

1.04 Theory and Observations: Normal Mode and Surface Wave Observations

G Laske, Scripps Institution of Oceanography, University of California San Diego, La Jolla, CA, USA

R Widmer-Schmidrig, Black Forest Observatory, Wolfach, Germany

© 2015 Elsevier B.V. All rights reserved.

1.04.1	Introduction	117
1.04.1.1	Free Oscillations	117
1.04.1.2	Surface Waves	118
1.04.1.3	What We See in Seismograms: The Basics	119
1.04.2	Free Oscillations	120
1.04.2.1	Modes of a Spherically Symmetric Earth	120
1.04.2.2	Modes of a Heterogeneous Earth	122
1.04.2.2.1	Mode splitting	122
1.04.2.2.2	Mode coupling	126
1.04.2.3	Measuring Mode Observables	128
1.04.2.3.1	Multiplet stripping and degenerate mode frequencies	130
1.04.2.3.2	Singlet stripping and receiver stripping	132
1.04.2.3.3	Retrieving the splitting matrix with the matrix autoregressive technique	133
1.04.2.3.4	Retrieving the splitting matrix with iterative spectral fitting	133
1.04.2.3.5	Observed mode coupling	135
1.04.2.4	Example of a Mode Application: Inner-Core Rotation	136
1.04.2.5	Example of a Mode Application: Earth's Hum	139
1.04.3	Surface Waves	141
1.04.3.1	Standing Waves and Traveling Waves	141
1.04.3.2	The Measurement of Fundamental Mode Dispersion	144
1.04.3.2.1	Group velocity	148
1.04.3.2.2	The study of ambient noise	149
1.04.3.2.3	Phase velocity	149
1.04.3.2.4	Time-variable filtering	151
1.04.3.3	Other Surface Wave Observables	152
1.04.3.4	Higher Modes	154
1.04.3.4.1	Higher-mode dispersion and waveform modeling	154
1.04.3.4.2	Love waves and overtones	157
1.04.3.5	Surface Waves and Structure at Depth	157
1.04.3.6	The Validity of the Great-Circle Approximation and Data Accuracy	160
1.04.4	Concluding Remarks	160
	Acknowledgments	161
	References	161

1.04.1 Introduction

1.04.1.1 Free Oscillations

The destructive $M_W=9.0$, 11 March 2011 Tohoku, Japan, earthquake most certainly raised recent awareness of extremely large earthquakes. And also remembering the $M_W=9.1$ 26 December 2004 Sumatra–Andaman earthquake and the $M_W=8.8$ 27 February 2010 Maule, Chile, earthquake, one can easily forget that a seismologist has to wait many years for a great, preferably deep earthquake to occur in order to observe Earth's free oscillations. After all, the last earthquake in this league of 'mega earthquakes' occurred 40 years before the Sumatra–Andaman event: the 'Good Friday' 27 March 1964 Alaska earthquake. It is therefore not surprising that, compared to other seismic studies, free oscillation studies started relatively late last century, after the great $M_W=9.5$ 22 May 1960

Valdivia, Chile, earthquake. It was not until 1975 – after the analysis of digitized records of the deep, magnitude 8.0 31 July 1970 Colombia earthquake – that enough mode measurements were available to construct the first one-dimensional (1-D), normal-mode derived Earth that could withstand decades of testing as a reference Earth model (REM) (1066A by Gilbert and Dziewonski, 1975). Not much later, great progress was achieved to facilitate the collection of high-quality mode data by installing the global digital seismic network IDA (International Deployment of Accelerometers), a network of LaCoste–Romberg gravimeters that were specifically designed to observe Earth's free oscillations (Agnew et al., 1976, 1986). In the meantime, permanent stations of several other global seismic networks have been upgraded with very broadband seismic sensors – typically Wielandt–Streckeisen STS-1 vault seismometers or Geotech–Teledyne KS-54000 borehole

seismometers – and digital recording units. This includes early networks that were designed to monitor global seismicity and the comprehensive test ban treaty (CTBT), such as the high-gain long-period (HGLP) network (first digitally recording network; Savino et al., 1972), the seismic research observatory (SRO; Peterson et al., 1980), the World-Wide Standardized Seismograph Network (WWSSN; Oliver and Murphy, 1971), and the China Digital Seismograph Network (CDSN; Peterson and Tilgner, 1985). Many of these stations as well as the upgraded IDA network are now part of the US Global Seismic Network (GSN) operated by IRIS (Incorporated Research Institutions for Seismology), but other global networks exist such as the French GEOSCOPE (Romanowicz et al., 1984) and the German GEOFON (Hanka and Kind, 1994). All these and more operate under the umbrella of the international Federation of Digital Seismograph Networks (FDSN; Romanowicz and Dziewonski, 1986). Roughly 25 years into very broadband seismic networks, a normal mode seismologist now can enjoy a more than tenfold increase in high-quality vertical-component long-period seismic records for a given earthquake. But even in the late 1990s – a few years after the deep magnitude 8.2 09 June 1994 Bolivia earthquake provided spectacular spectra – great effort was invested in digitizing the legendary 1970 Colombia records. Before the 26 December 2004 Sumatra–Andaman earthquake, there have been a handful of other great earthquakes since ‘Bolivia.’ But even the great 23 June 2001 Arequipa, Peru, earthquake, the largest digitally recorded earthquake until then, did not excite the relatively few normal mode observers whose interest lies in unraveling the deep secrets of the inner core (IC). ‘Peru’ was simply not deep (or great) enough to make some of the modes ring that the observers are interested in. On the other hand, since normal modes involve the vibration of the whole planet, mode observations at a single station readily reveal a wealth of information about Earth structure that no other seismic techniques can provide. Modes are intrinsic low-pass filters of Earth structure. It is relatively easy to collect unbiased estimates of mode observables that constrain the spherical average of Earth as well as long-wavelength perturbations to it. It is therefore not surprising that in the current efforts to remove the more than three-decade-old ‘preliminary’ from PREM (preliminary reference Earth model, Dziewonski and Anderson, 1981) – the currently still most widely accepted REM of the spherical average – a suitable mode data set for an updated model exists (a ‘best-estimate’ data set can be obtained from the REM website), while we still struggle to obtain an unbiased body-wave data set.

Normal mode seismology has facilitated other great achievements that we can proudly look back to. For example, the analysis of modes provided the ultimate proof that the IC is solid (Dziewonski and Gilbert, 1971). Normal mode studies were at the forefront to assess Earth’s attenuation (Smith, 1972) and to retrieve earthquake moment tensors (Gilbert and Dziewonski, 1975), which has been continued in the faithful delivery of the Harvard centroid moment tensors (CMTs) (Dziewonski et al., 1981) now continued as the ‘global CMT project’ led by Göran Ekström at Lamont Doherty Earth Observatory (LDEO) (Ekström et al., 2012; www.globalcmt.org) that many colleagues depend on for their own studies. Normal mode studies also were at the forefront to assess Earth’s 3-D structure. For example, Jobert and Roullet (1978) found early evidence for large-scale lateral variations from free

oscillations and surface waves, and Masters et al. (1982) discovered harmonic degree 2 variations in the transition zone that are associated with subducting slabs. The first widely used 3-D models of Earth’s upper mantle, M84A and M84C (Woodhouse and Dziewonski, 1984), were obtained using mode theory. Still today, careful analysis of high-precision mode measurements provides crucial clues to answer some of the most fundamental geodynamical questions that remain elusive to other seismic techniques. For example, the analysis of Masters and Gubbins (2003) provided updated estimates of the density jump across the IC boundary, which is relevant to the discussion of the growth rate and the age of the IC. They also argue against a significant overall excess density in the lowermost mantle that was proposed by Kellogg et al. (1999) for locally varying hot abyssal layers for which seismic evidence was presented by Ishii and Tromp (1999). Earth’s density structure and the solidity of the IC are best constrained by mode data. Similarly, modes help determine Earth’s internal anelastic and anisotropic structure. There are many more aspects where mode data can help out to understand how our planet works. One example is the differential rotation of the IC. Evidence for this was first observed using body-wave data and was initially reported to be between 1° and 3° per year (Song and Richards, 1996; Su et al., 1996) but hotly debated (e.g., Souriau, 1998). As subsequent studies accumulated, this number decreased dramatically and is currently estimated at 1/10 of the initial rate. Mode observations in particular (Laske and Masters, 1999, 2003; Sharrock and Woodhouse, 1998) provided the conclusive constraints to correct the rotation estimates downward.

In the first part of this chapter, the reader gets acquainted with the jargon used in normal mode seismology, some of which requires to summarize the theoretical background that is described in Chapter 1.02. We then introduce some of the most commonly used measurement techniques that we have been involved in. Mode analysis involves more than simply reading the peak frequencies and amplitudes from a spectrum. In fact, in most cases, such an approach leads to biased estimates. One also has to bear in mind that the most basic analysis techniques treat modes as being isolated from their neighbors in which case only Earth structure of even-degree symmetry can be retrieved. Earth’s rotation and lateral variations cause modes to couple with each other. This complicates mode analysis but also facilitates the assessment of odd-degree structure. This is briefly described.

1.04.1.2 Surface Waves

Surface waves can be understood as a superposition of free oscillations. It is therefore not surprising that many long-period surface wave seismologists analyzed normal modes at some time in their career. With a few exceptions, including very deep earthquakes, fundamental mode surface waves are the largest signal in a seismogram. First-arriving surface wave packets are relatively short and do not require the consistently high signal levels, over several days, as normal modes do. Nor do they require the wait for very large earthquakes. The analysis of surface waves essentially involves the analysis of fundamental modes and the first few overtones, at high frequencies. Surface waves are therefore a natural choice to explore Earth’s

crust, upper mantle, and transition zone. Much like in a body-wave study, the analyst collects travel times, but the complication is that these depend on frequency. Rather than a sharp onset, a wave packet is observed that is often likened to a Gaussian packet. The two travel time-equivalent observables of dispersed surface waves are phase velocity, the speed at which a certain point in the waveform travels, and group velocity, the speed at which wave energy or a point on the envelope of the waveform travels. Though both observables constrain structure at depth, they have different dependencies, and ideally one would want to measure both. Group velocity tends to change more significantly with structure at depth, but its measurement errors are also larger than those of phase velocity. On the other hand, source effects on group velocity are relatively small and are usually ignored. Details on earthquake source processes therefore do not have to be known to measure group velocity.

The analysis of surface waves has a major advantage over that of body waves. In the upper mantle, imaging capabilities using body waves are dictated by the distribution of earthquakes and seismic stations. Surface waves travel along the surface between sources and receivers, crossing remote areas and thereby picking up invaluable information about along-path upper-mantle structure that remains elusive to body waves. Like a body-wave arrival, group velocity can be measured on a single wave train recorded at a single station without having to resort to calculating synthetic seismograms that are necessary to measure phase travel times. For this reason, group velocity analysis has seen a wide range of applications in regional seismology, especially in the CTBT community, even before the advent of sophisticated signal processing.

In the second part of this chapter, we first summarize the relationship between normal modes and surface waves. Some of the surface wave observables are described and how they are measured. We touch on the observation of higher modes and discuss the relationship between dispersion and structure at depth, but the reader interested in Earth structure is referred to other contributions in this volume.

1.04.1.3 What We See in Seismograms: The Basics

For moderately large earthquakes, seismograms exhibit a number of wave trains, some of which circled the globe completely before arriving at a station. **Figure 1** shows the nomenclature for these wave trains. We distinguish between minor and major arc wave trains that arrive at a station from the source directly or took the long path in the opposite direction. **Figure 2** shows an example of a vertical seismic record collected at a station of the GEOSCOPE network. Rayleigh wave trains are usually labeled R, while overtones are often labeled X (e.g., [Roult et al., 1986](#)). Love wave trains carry the label G and are observed on the transverse component only, unless Earth's rotation and/or heterogeneity causes strong lateral refraction or, to use the mode analogy, toroidal-spheroidal mode coupling. For large earthquakes with magnitudes typically larger than $M_S = 6.5$, surface waves may be observed as they circle the globe multiple times. At group velocities of about 3.7 km s^{-1} , long-period Rayleigh waves take about 3 h to complete one orbit.

Very large earthquakes can be observed at many global seismic stations with fidelity high enough to discern many

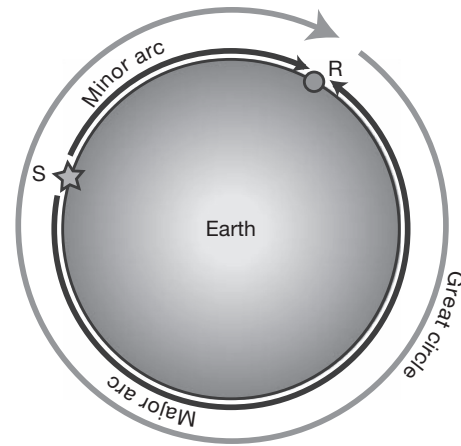


Figure 1 Surface wave paths from source S to receiver R. Paths associated with the shorter distance from the source are minor arc paths (R_1); paths associated with the larger distance are major arc paths (R_2). The number following R is the wave orbit number. The wave orbit number advances by two when successive wave trains include a complete great circle (e.g., R_3 and R_5 for minor arc paths).

wave trains in a record section. **Figure 3** shows the tsunami-generating 2001 Arequipa, Peru, earthquake. We can follow R_1 across the globe from the source toward its antipode where the wave train merges with R_2 . Near the source, R_2 and R_3 overlap. A similar collapse of waveforms can be observed for later wave trains. Gray lines mark some of the body-wave phases that combine to form the overtones X wave trains as shown in **Figure 2**. For earthquakes as large as the Arequipa event, multiple body-wave reflections off the surface, or globe-circling overtones, are also discernible. Very nicely displayed for the Arequipa event, we can follow these overtones at significant signal levels between the fundamental modes, and later, overtone packets also merge near the source and its antipode. If we consider these overtone packets as modes, some of them have very low attenuation rates and can persist well after the fundamental modes have decayed into the noise. To observe these modes with high fidelity, the collected records typically have to be at least 5 days long.

Figure 4 shows the spectrum of a large earthquake observed at the Black Forest Observatory (BFO) in Germany. Since Earth is a finite body, transient waves propagating away from a localized source eventually interfere. For paths whose orbital length is an integer multiple of the wavelength, the two signals interfere constructively while destructive interference occurs otherwise. The spectrum of the several-day-long coda therefore yields discrete lines that correspond to Earth's normal modes, while destructive interference is responsible for the gaps separating the peaks.

We distinguish between observably split and not observably split modes. A spectral line of the former type has more than one peak in a typical spectrum (**Figure 5**). This 'splitting' of a mode is caused by the fact that individual singlets, the different 'vibrational states' of a certain mode (multiplet), are no longer degenerate in a nonspherical Earth. Observably split modes are typically of low angular order, that is, the

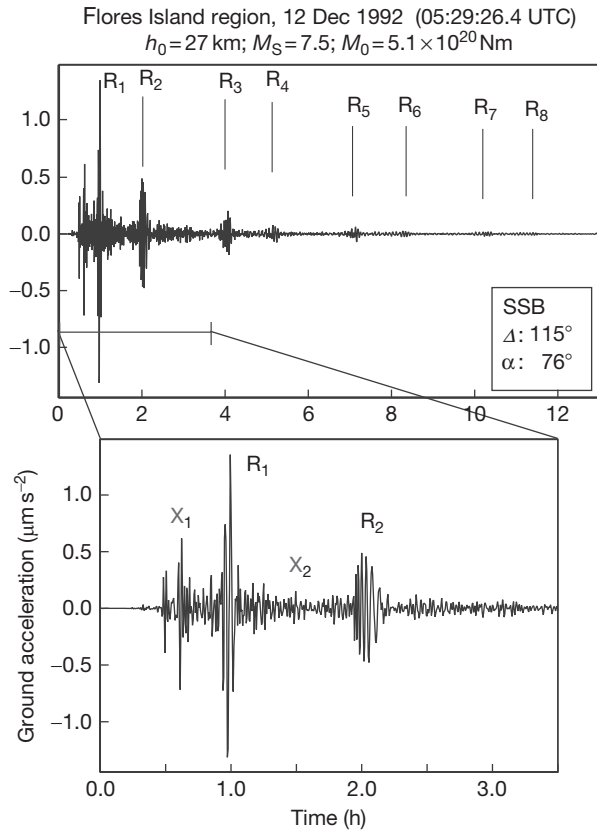


Figure 2 The 1992 Flores Island earthquake, recorded at GEOSCOPE station SSB (Saint Sauveur Badole, France). Marked are eight fundamental mode Rayleigh wave trains (R_n) and the first two overtone groups (X_n). Δ and α are the epicentral distance and the back azimuth to the event. Since the earthquake was more than 90° away, R_1 and R_2 are closer together than R_2 and R_3 . At group velocities of about 3.7 km s^{-1} , it takes 3 h for Rayleigh waves to circle the globe. Hence, R_3 arrives at a station 3 h after R_1 . The seismogram was low-pass-filtered with a convolution filter to suppress signal above 20 mHz.

geographic pattern of surface displacement is simple and the mode has few singlets. In the case of not observably split modes (Figure 4), there are so many singlets of a mode or the singlets are so close together that a standard spectral analysis is not able to resolve them. Another limiting factor to resolve a mode's splitting is its attenuation rate. The rather complex superposition of all the singlets causes an 'apparent frequency shift' of an otherwise ordinary-looking spectral peak where the shift depends on lateral variations in Earth structure (Jordan, 1978).

Having long wavelengths compared to transient seismic waves, such as body waves and surface waves, free oscillations inherently average over large volumes, which leads to comparatively poor resolution of Earth's heterogeneous structure. On the other hand, free oscillation studies are much less likely biased by the uneven global distribution of earthquake sources and seismic receivers. Mode observables are relatively weakly sensitive to structure with odd-degree symmetry because waves traveling on a sphere lose their sensitivity to this structure as time goes on. With every completed great circle, an observable accumulates information about the average structure over the entire great-circle path. This information is symmetric with

respect to Earth's center and thus reflects only even-degree structure. We will revisit this problem in the surface wave section.

1.04.2 Free Oscillations

1.04.2.1 Modes of a Spherically Symmetric Earth

The elastic-gravitational response of Earth to localized, transient excitations consists of impulsive disturbances followed by dispersed wave trains and long-lasting standing waves, as seen in Figures 2–4. As long as an earthquake rupture is ongoing, Earth responds with forced vibrations. Once the rupture has ceased, Earth undergoes free oscillations around its new equilibrium state. The rupture duration of the largest earthquakes is on the order of a few minutes and thus very much shorter than the typical decay time of modes, which is a few tens of hours. A study of the source based on low-frequency seismic records reduces to the estimation of the initial amplitude and phase of the modes, while studies of Earth's internal mechanical structure concentrate on the frequency, ω , and attenuation, α , of the mode, where $\alpha = \omega/2Q$ and Q the quality factor.

The deviations of Earth structure from a spherically symmetric reference state are quite small. It is therefore convenient to discuss free oscillations of a spherically averaged Earth and treat any deviation away from this state with perturbation theory. On a spherically symmetric Earth, three integer quantum numbers, n , ℓ , and m , fully specify the set of normal modes. The azimuthal order, $|m|$, counts the number of nodal surfaces in the longitudinal direction $\hat{\phi}$. The number of nodal surfaces in the colatitudinal direction, $\hat{\theta}$, is $|\ell - m|$, where ℓ is the angular order. For fixed ℓ and m , the overtone number n indexes the modes with increasing frequency.

Solutions of the linearized, homogeneous equations of motion for a self-gravitating elastic Earth can be written as (Aki and Richards, 1980, 2002; Backus, 1967; Dahlen and Tromp, 1998; Chapter 1.02)

$${}_n u_\ell^m(\mathbf{r}, t) = \text{Re} \left[\left(\hat{\mathbf{r}}_n U_\ell(r) Y_\ell^m(\theta, \phi) + {}_n V_\ell(r) \nabla_1 Y_\ell^m(\theta, \phi) - {}_n W_\ell(r) \hat{\mathbf{r}} \times \nabla_1 Y_\ell^m(\theta, \phi) \right) e^{i_n \omega_\ell^m t} \right] \quad [1]$$

where ${}_n u_\ell^m$ is the displacement eigenfunction of the mode singlet identified by the (n, ℓ, m) -triplet and ${}_n \omega_\ell^m$ is its eigenfrequency. Y_ℓ^m are surface spherical harmonic functions and ∇_1 is the surface gradient operator. While n and ℓ can be any non-negative number ($n \geq 0, \ell \geq 0$), the azimuthal order is limited to the interval $-\ell \leq m \leq \ell$. The spherical harmonics describe the angular shape of the eigenfunction. An example for some low-order spherical harmonics is shown in Figure 6.

The three scalar radial eigenfunctions, ${}_n U_\ell(r)$, ${}_n V_\ell(r)$, and ${}_n W_\ell(r)$, describe the way the modes sample Earth with depth. As n increases, they become more oscillatory with depth, leading to an increased number of nodal spheres. For toroidal modes, n is the number of nodes in W , while for radial modes, n is the number of nodes in U . For spheroidal modes, both U and V can have nodes, but the number of nodes is not as easily related to n . The radial eigenfunctions do not depend on the azimuthal order m and are thus identical for all singlets within a multiplet. Eigenfunctions for some mode examples are shown in Figures 7 and 8. The relevant quantity for the

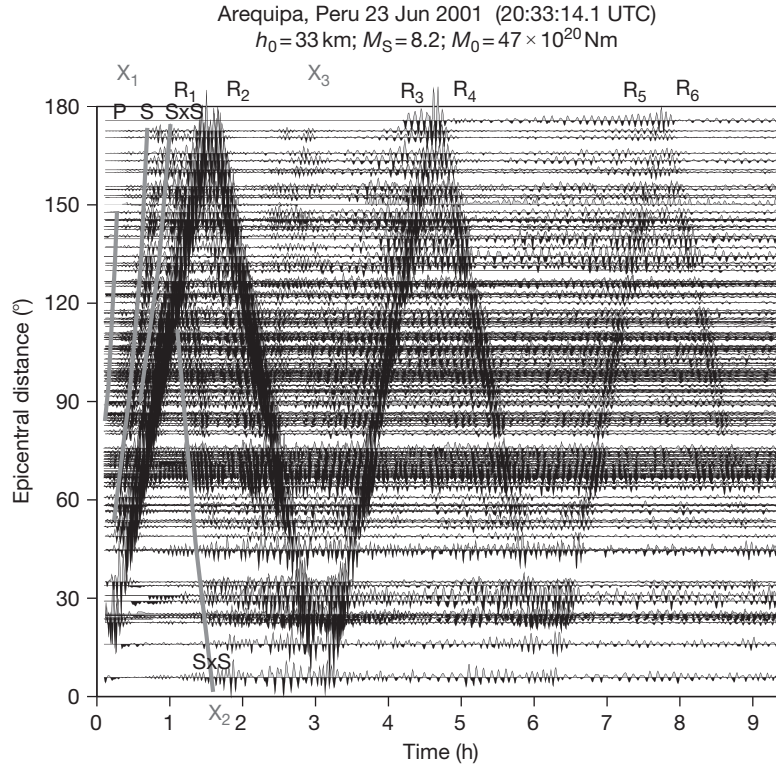


Figure 3 Record section of the 2001 Arequipa, Peru, earthquake, the largest digitally recorded earthquake before the 2004 Sumatra–Andaman earthquake. Marked are six fundamental mode Rayleigh wave trains (R_n) and early compressional (P) and shear (S) body-wave arrivals. Also marked are S multiples that bounced off the surface (SxS). Such phases are contributors to the major arc overtone phases X_n . At 90° epicentral distance, surface wave trains traveling in opposite directions arrive at a station at equidistant time intervals, while wave trains overlap at the antipode and near the source.

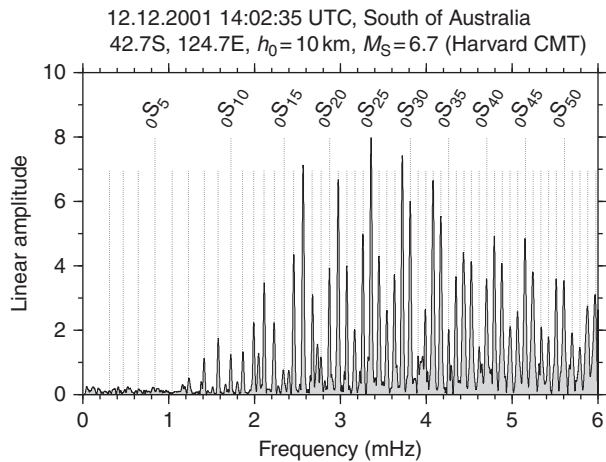


Figure 4 Spectrum of a magnitude $M_S=6.7$ earthquake south of Australia that was recorded at station BFO (Black Forest Observatory, Germany). The succession of globe-circling Rayleigh wave packets in roughly 3 h intervals manifests itself in the spectrum through the regular spacing between adjacent fundamental spheroidal modes ${}_0S_\ell$ of about $(3 \text{ h})^{-1} \approx 0.1$ mHz. The underlying time series is 18 h long.

sensitivity of a mode to structure with depth is actually not the eigenfunction but the energy density. This is because the modes are stationary solutions to the Lagrangian energy functional (Gilbert, 1980). A mode can store elastic energy in shear

and in compression, and it can store gravitational potential energy. Significant amounts of the latter can be stored only by spheroidal modes below 1 mHz. For most other modes, their sensitivity to structure can be discussed based solely on their shear and compressional energy densities.

For the spherically symmetric reference state, the structure of the spectrum of a mode (fixed n and ℓ) exhibits a high degree of degeneracy in that all of its $2\ell+1$ singlets have the same frequency and the same radial eigenfunction. This degeneracy in m is a consequence of the fact that the singlet eigenfrequencies cannot depend on the choice of the coordinate system. The ensemble of $2\ell+1$ singlets comprises the mode multiplet. Further classification into spheroidal and toroidal modes is possible in the spherically symmetric case. The displacement field of toroidal modes, ${}_nT_\ell^m$, is purely horizontal and divergence-free with ${}_nU_\ell(r) = {}_nV_\ell(r) = 0$. Thus, it involves only shearing and does not lead to any deformation of the radial interfaces. Spheroidal modes, ${}_nS_\ell^m$, for which ${}_nW_\ell(r) = 0$, involve volumetric changes as they are composed of both horizontal and vertical displacements. They deform interfaces and also perturb the gravity field. A third subclass of modes are the radial modes, ${}_nS_0$, for which $\ell=0$ and the displacement is purely radial, so that ${}_nV_\ell(r) = {}_nW_\ell(r) = 0$.

The formulation of computational methods for the practical calculation of normal-mode seismograms reaches back to the early 1970s. Takeuchi and Saito (1972) first formulated a Runge–Kutta matrix integration scheme to solve the ordinary

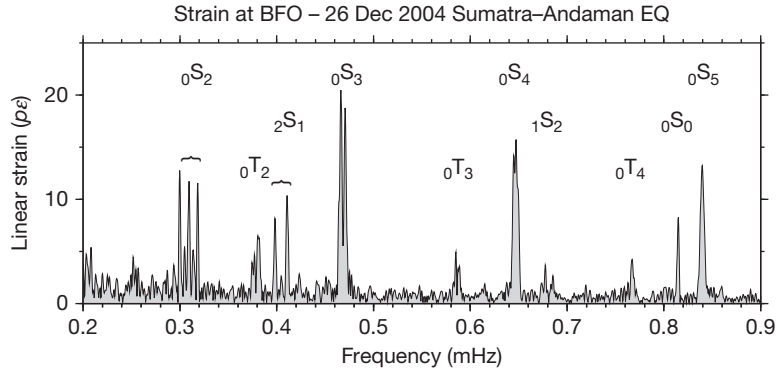


Figure 5 Linear Fourier amplitude spectrum of strain from the 2004 Sumatra–Andaman earthquake recorded by the invar wire strainmeter at station BFO with azimuth N2°E. The time-domain amplitude of ${}_0S_0$ at 0.814 mHz is $8 \times 10^{-12} \epsilon$. This is a rare spectrum showing evidence of Zeeman-type splitting due to Earth’s rotation of not only to the lowest-order spheroidal modes ${}_0S_2$, ${}_2S_1$, ${}_0S_3$, and ${}_0S_4$ but also to the two lowest-order toroidal modes ${}_0T_2$ and ${}_0T_3$. The strainmeter array at BFO is described in [Widmer et al. \(1992a\)](#). A barometric correction similar to that of [Zürn and Widmer \(1995\)](#) has been applied to this spectrum. With an empirically determined strain pressure compliance of 0.8 ne hPa^{-1} , a lowering of the noise floor by a factor 4 was achieved. The first 240 h after the event was used for the spectrum.

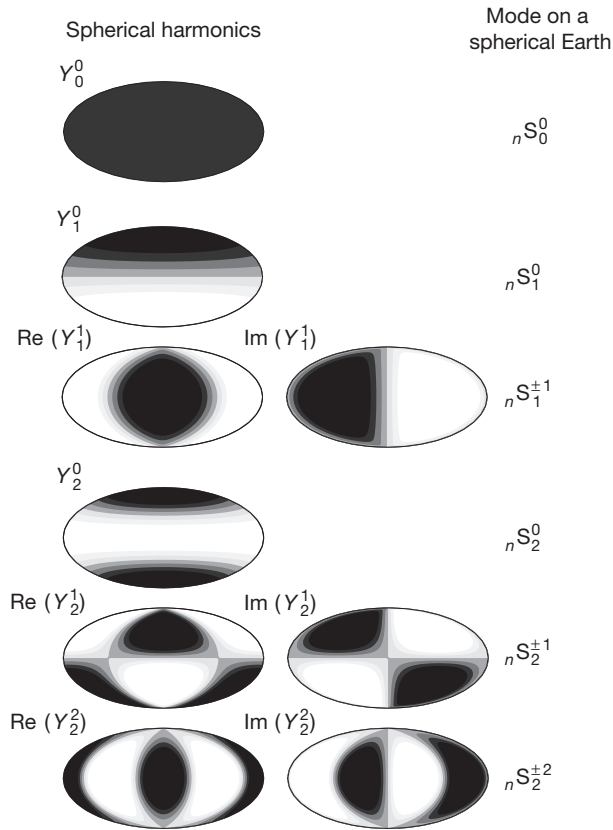


Figure 6 Surface spherical harmonics $Y_l^m = X_l^m(\theta)e^{im\phi}$ that compose the basis set for radial modes (e.g., ${}_0S_0$, ${}_1S_0$) and $\ell=0, 1$, and 2 spheroidal modes (e.g., ${}_1S_1$, ${}_2S_1$, ${}_0S_2$, and ${}_3S_2$), plotted in Hammer–Aitoff projection. The singlets of modes have these shapes on the \hat{r} component of recordings on a spherical, nonrotating Earth. Modified from Masters TG, Laske G, and Gilbert F (2000c) Large-scale Earth structure from analyses of free oscillation splitting and coupling. In: Boschi E, Ekström G, and Morelli A (eds.) *Problems in Geophysics for the New Millennium*, pp. 255–288. Bologna: Editrice Compositori.

differential equations governing free oscillations. This method is still used today. Freeman Gilbert implemented a propagator matrix approach in his computer program EOS, and various descendants of this code have also been circulating informally since that time. We mention two versions here: OBANI by John Woodhouse and MINOS by Guy Masters. Woodhouse advanced the code by allowing to compute the eigenfunctions through the method of minors. He also introduced a mode counter for spheroidal modes, while Masters added one for toroidal and radial, Stoneley, and IC modes. A description of OBANI can be found in [Woodhouse \(1988\)](#). MINOS can be downloaded from the REM website.

1.04.2.2 Modes of a Heterogeneous Earth

1.04.2.2.1 Mode splitting

As an Earth model becomes successively more realistic and complex, the spherical symmetry is broken and a mode spectrum becomes more complex. The principal deviations from the spherically symmetric reference state are Earth’s daily rotation, its hydrostatic ellipticity in response to the rotation, and its general aspherical structure. The latter includes the topography of interfaces and lateral variations in isotropic and anisotropic volumetric parameters. The distribution of singlets within a multiplet on a rotating Earth in hydrostatic equilibrium is given by [Dahlen \(1968\)](#). If the (n, ℓ) -tuple denotes the k th spheroidal or toroidal multiplet, then the eigenfrequency of the m th singlet of an isolated multiplet is

$$\omega_k^m = \bar{\omega}_k (1 + a + mb + m^2c) \text{ with } -\ell \leq m \leq \ell \quad [2]$$

where $\bar{\omega}_k$ is the multiplet degenerate frequency, a and c the ellipticity splitting coefficients (to first order), and b the rotational splitting coefficient ([Dahlen, 1968](#)). The ellipticity of figure removes the degeneracy of a mode only partially, with ${}_n\omega_k^m = {}_n\omega_k^{-m}$. This splitting is asymmetric with respect to the degenerate frequency. On the other hand, the rotational splitting is symmetric, or of Zeeman type, and removes the

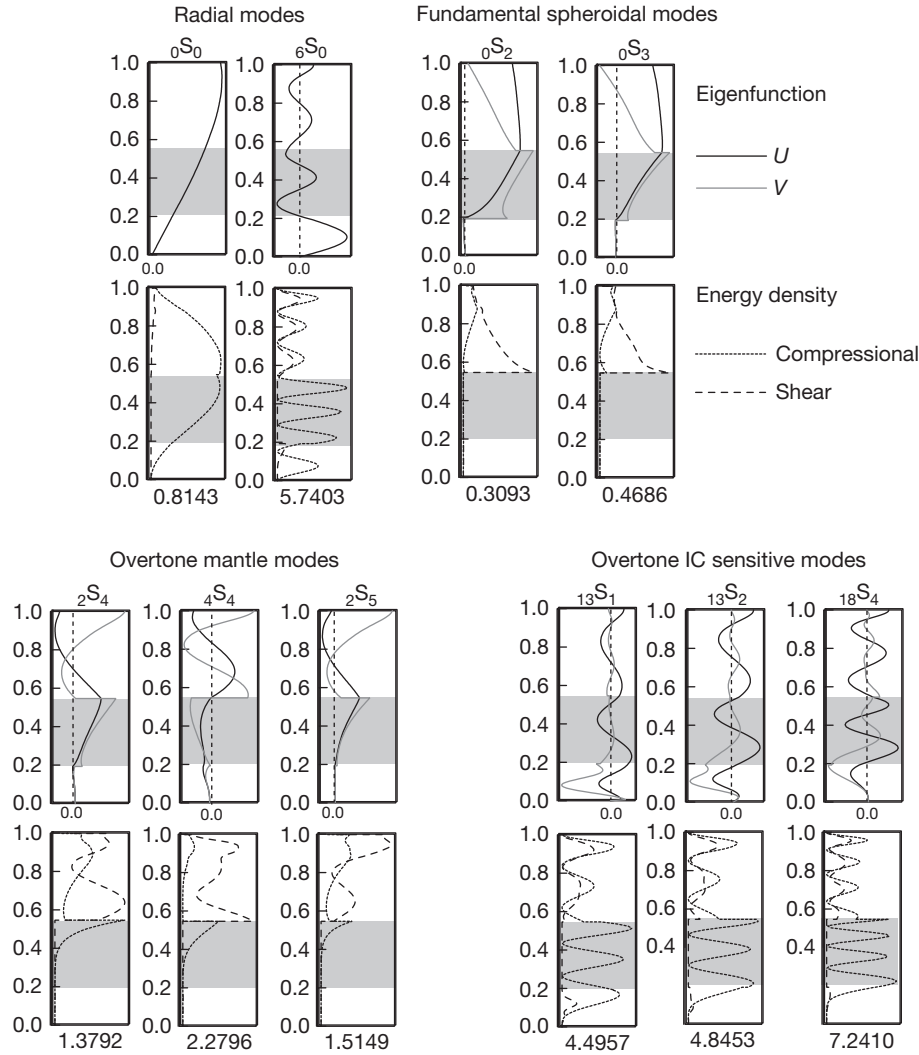


Figure 7 Radial eigenfunctions U and V and compressional and shear energy densities for some modes described in this chapter, displayed as function of normalized radius (0 is at the center; 1 is at the surface). Gray areas mark the outer core. Numbers at the bottom of the panels are PREM mode frequencies in mHz (Dziewonski and Anderson, 1981). Radial modes are very sensitive to core structure, while spheroidal fundamental modes are not very sensitive to κ and μ in the core. On the other hand, overtone mantle modes that are primarily sensitive to mantle structure are also influenced by κ in the core. IC-sensitive modes that can be observed at Earth's surface are typically quite sensitive to mantle structure.

degeneracy completely. Splitting due to rotation dominates at low frequencies ($b \gg c$) so that the spacing between adjacent singlets is nearly constant (see Figures 5 and 9). Other examples of modes whose splitting is dominated by rotation are modes ${}_0S_5$ and ${}_1S_4$ (Figure 10). At higher frequencies, ellipticity and heterogeneous structure become the dominant cause and frequencies become partially degenerate when $b \ll c$. Examples of such modes are ${}_{13}S_2$ and ${}_{18}S_4$. IC-sensitive modes ${}_{3}S_2$, ${}_{13}S_2$, and ${}_{18}S_4$ are anomalously split, as first observed by Masters and Gilbert (1981). In these cases, the splitting width, the range of singlet frequencies, is significantly larger than that predicted by rotation and ellipticity. In fact, the extreme splitting of ${}_{10}S_2$ led Gilbert and Dziewonski (1975) to misidentify the $m=0$ line of ${}_{10}S_2$ as mode ${}_{11}S_2$. Based on their observations, Masters and Gilbert (1981) argued for high Q in the IC but did not interpret the anomalous splitting. Ritzwoller et al. (1986) speculated that the anomalous splitting is due to

axisymmetric structure in the outer core (see also Romanowicz and Bréger, 2000). Woodhouse et al. (1986) were the first to attribute this splitting to the anisotropic IC, which now appears to be widely accepted (see, e.g., Tromp, 1993).

Gilbert (1971) investigated how small structural perturbations to a spherically symmetric Earth affect the spectrum of a multiplet. He formulated the 'diagonal sum rule,' which states that, to first order, the arithmetic mean of the $2\ell+1$ singlet frequencies is the multiplet degenerate frequency $\bar{\omega}_k$:

$$\bar{\omega}_k = \frac{1}{2\ell+1} \sum_{m=-\ell}^{\ell} \omega_k^m \quad [3]$$

Any first-order perturbation in structure leaves the degenerate frequencies of the spherical Earth unchanged. On the other hand, the second-order effects of the Coriolis force may cause a frequency shift. Dahlen (1968) showed that the singlet

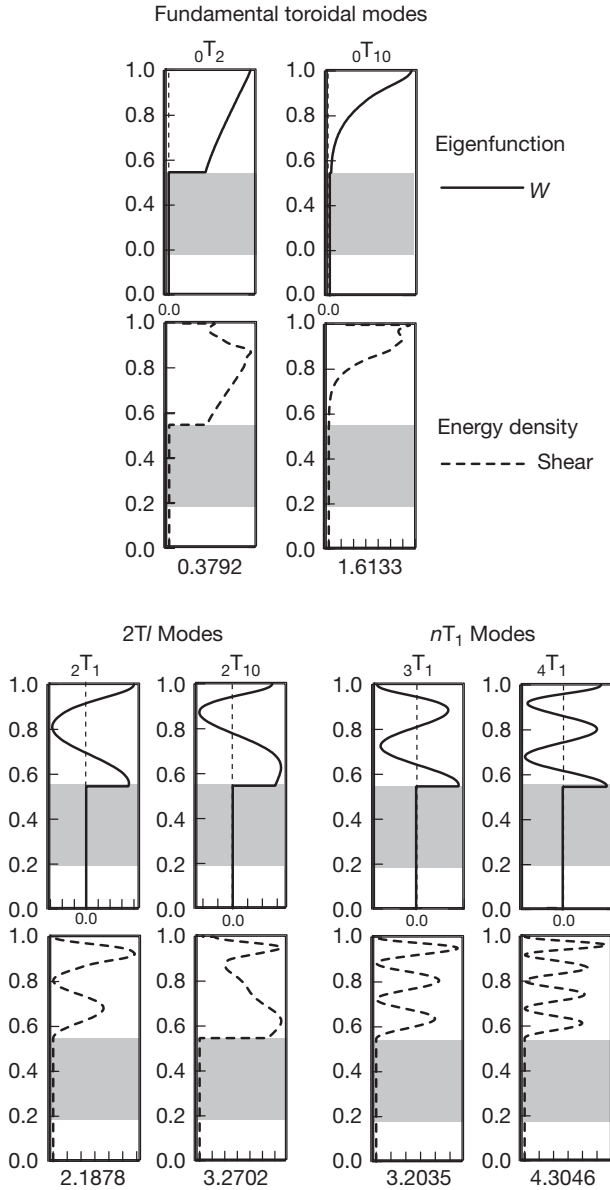


Figure 8 Radial eigenfunction W and shear energy densities for some toroidal modes. Toroidal modes are sensitive only to the shear modulus, μ . For details, see [Figure 7](#).

distribution within a multiplet still follows the parabolic distribution of eqn [2], but second-order terms contribute to factors a and c , and the diagonal sum rule is no longer valid. [Dahlen \(1968\)](#) and [Dahlen and Sailor \(1979\)](#) provided the splitting parameters for modes below 2 mHz for a variety of Earth models. Since the splitting parameters caused by rotation and Earth's hydrostatic ellipticity are well understood, their effects are usually corrected for before mode parameters are interpreted in terms of Earth structure.

Once the eigenfrequencies and eigenfunctions of a 1-D Earth model have been computed, the synthesis of seismograms based on free oscillations is rather straightforward as it involves only the summation over all multiplets in a desired frequency band. The representation of the time series of an

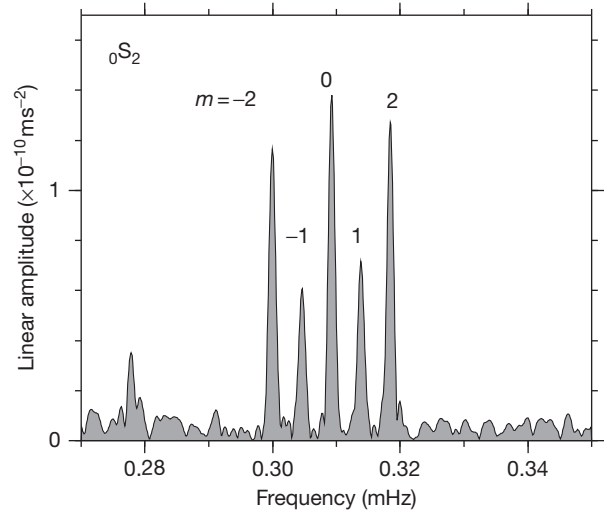


Figure 9 Zeeman splitting of the 'football mode' ${}_0S_2$. This is a Fourier spectrum of a 500 h long record of the 2004 Sumatra–Andaman earthquake by the superconducting gravimeter at Strasbourg, France ([Rosat et al., 2005](#)). A scaled version of the locally recorded barometric pressure was subtracted from the gravity record to achieve a noise reduction by a factor 2. The time-domain acceleration amplitude of the singlets is close to 10^{-10} ms^{-2} . Zeeman-type splitting of a mode is caused by Earth's rotation.

isolated split multiplet with degenerate frequency $\bar{\omega}_k$ at station j is given by

$$u_j(t) = \sum_{m=1}^{2\ell+1} R_{jm} a_m(t) e^{i\bar{\omega}_k t} \quad \text{or} \quad \mathbf{u}(t) = \mathbf{R} \cdot \mathbf{a}(t) e^{i\bar{\omega}_k t} \quad [4]$$

where the real part is understood (e.g., [Landau and Lifshitz, 1958](#), section 40; [Woodhouse, 1983](#); [Woodhouse and Girmius, 1982](#)). The j th row of \mathbf{R} is a $2\ell+1$ vector of spherical harmonics, which describes the motion of the spherical-Earth singlets at the j th receiver and is readily calculated. $\mathbf{a}(t)$ is a slowly varying function of time given by

$$\mathbf{a}(t) = \exp(i\mathbf{H}t) \cdot \mathbf{a}(0) \quad [5]$$

where $\mathbf{a}(0)$ is a $2\ell+1$ vector of spherical-Earth singlet excitation coefficients, which can be computed if the source mechanism of the event is known. \mathbf{H} is the complex 'splitting matrix' of the multiplet and incorporates all the information about elastic and anelastic 3-D structure to which the mode is sensitive, that is,

$$H_{mm'} = \bar{\omega}_k \left[(a + mb + m^2c) \delta_{mm'} + \sum_s \gamma_s^{mm'} c_s^t + i \sum_s \gamma_s^{mm'} d_s^t \right] \quad [6]$$

where $-\ell \leq m \leq \ell$, $-\ell \leq m' \leq \ell$, and $t = m - m'$. The first term describes the splitting due to Earth's rotation and ellipticity (eqn [2]), and the second and third terms describe the effects from elastic and anelastic structures through the 'structure coefficients,' c_s^t and d_s^t (e.g., [Ritzwoller et al., 1986](#); [Smith and Masters, 1989b](#)). Equation [6] changes to equation (14.84) of [Dahlen and Tromp \(1998\)](#) if real instead of complex basis eigenfunctions and spherical harmonics are considered in eqn [1]. \mathbf{H} and consequently $\exp(i\mathbf{H}t)$ are $(2\ell+1) \times (2\ell+1)$ -dimensional square matrices. The $\gamma_s^{mm'}$ are integrals over three

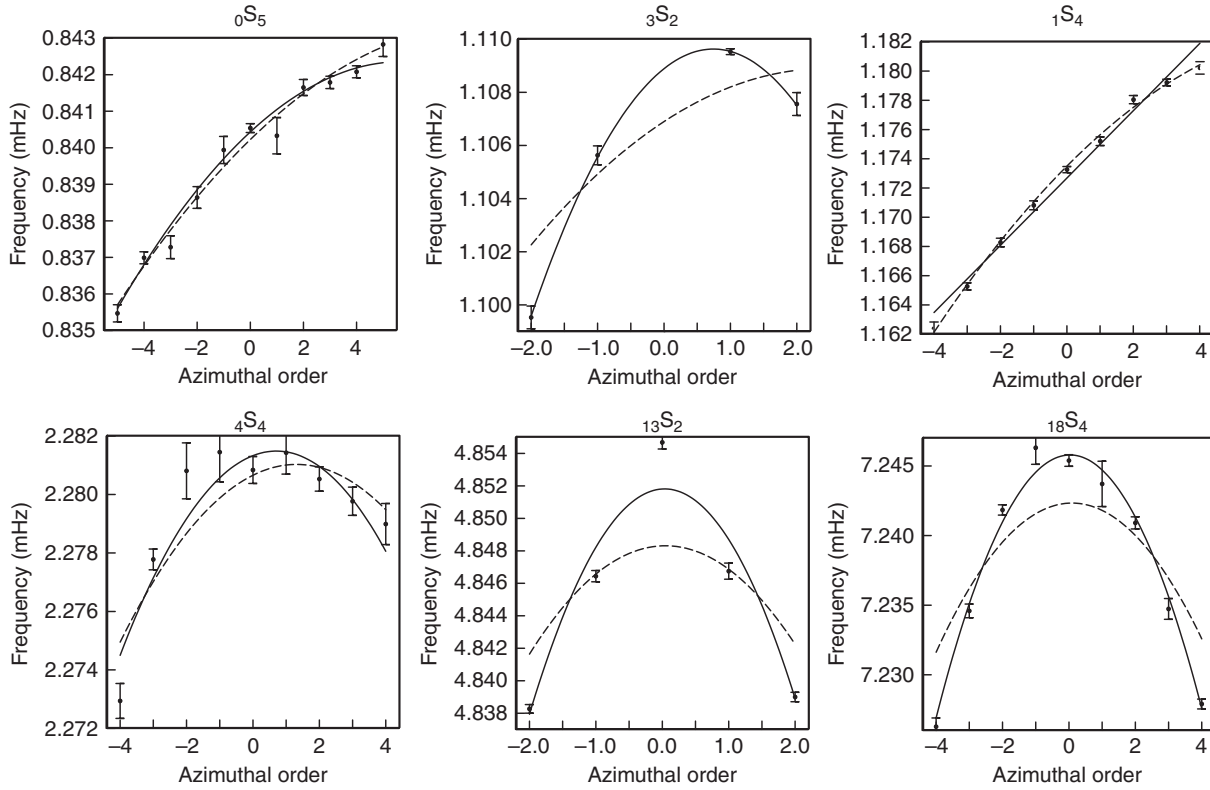


Figure 10 Observed singlet frequencies as a function of azimuthal order, m , for six modes. The dashed lines mark the splitting predicted for Earth's rotation and hydrostatic ellipticity. Solid lines mark the best-fitting parabolas. The splitting of low-frequency modes ${}_0S_5$ and ${}_1S_4$ is dominated by rotation, while that of IC-sensitive modes ${}_{13}S_2$ and ${}_{18}S_4$ is dominated by ellipticity. The splitting of mantle mode ${}_4S_4$ and low-frequency IC-sensitive mode ${}_3S_2$ is mixed. The $m=0$ singlet of ${}_3S_2$ has not yet been observed reliably. IC-sensitive modes are anomalously split, that is, the observed splitting is significantly larger than that predicted for rotation and ellipticity alone.

spherical harmonics (e.g., Dahlen and Tromp, 1998). These integrals are often zero, and the 'selection rules' summarize the nonzero conditions:

1. $m - m' = t$
2. $\ell + s + \ell'$ must be even; i.e., s must be even [7]
3. $0 \leq s \leq 2\ell$ (triangle rule)

Rule (1) implies that axisymmetric structure ($t=0$) gives nonzero contributions to the splitting matrix only if $m=m'$, so that \mathbf{H} is diagonal. Rule (2) implies that an isolated mode is sensitive only to structure of even degree. The rule can be extended to two coupled modes in which case $\ell + s + \ell'$ must be even (for same-type coupling; see Section 1.04.2.2.2 for details). In order to retrieve structure of odd harmonic degree, $\ell + \ell'$ must therefore be odd. Rule (3) implies that a mode cannot be sensitive to structure of arbitrarily high degree. The rule can also be extended to the case of two coupled modes where $|\ell - \ell'| \leq s \leq \ell + \ell'$. The structure coefficients for elastic structure, c_s^t , are given by

$$c_s^t = \int_0^a \mathbf{M}_s(r) \cdot \delta \mathbf{m}_s^t(r) r^2 dr \quad [8]$$

and a similar expression exists for the anelastic structure coefficients, d_s^t . The coefficients $\delta \mathbf{m}_s^t$ are the expansion coefficients of the 3-D aspherical Earth structure: $\delta \mathbf{m}(r, \theta, \phi) = \sum \delta \mathbf{m}_s^t(r) Y_s^t(\theta, \phi)$ and \mathbf{M}_s are integral kernels, which can be computed

(Henson, 1989; Li et al., 1991a; Woodhouse, 1980; Woodhouse and Dahlen, 1978). Equation [8] and its counterpart for the d_s^t s can be regarded as a pair of linear inverse problems for \mathbf{c} and \mathbf{d} . Strictly speaking, eqn [4] is not quite correct since both \mathbf{R} and $\mathbf{a}(0)$ should include small renormalization terms (see equations 14.87 and 14.88 in Dahlen and Tromp, 1998). The renormalization requires the knowledge of the splitting matrix, which we ultimately want to determine in a mode analysis. While the renormalization terms are expected to be small for isolated modes, we may have to iterate the retrieval of the splitting matrix for coupled modes.

It is convenient to visualize the geographic distribution of structure as sensed by a mode by forming the elastic and anelastic 'splitting functions' (Woodhouse and Giardini, 1985):

$$\begin{aligned} f_E(\theta, \phi) &= \sum_{s,t} c_s^t Y_s^t(\theta, \phi) \\ f_A(\theta, \phi) &= \sum_{s,t} d_s^t Y_s^t(\theta, \phi) \end{aligned} \quad [9]$$

The $Y_s^t = X_s^t(\theta) e^{it\phi}$ is a spherical harmonic of harmonic degree s and azimuthal order number t . An example is shown in Figure 11. The elastic splitting function shows local peak shift variations caused by the local structure beneath a geographic location, as 'seen' by an isolated mode. Recall that isolated modes are not sensitive to odd-degree structure. In a similar way, the anelastic splitting function shows attenuation.

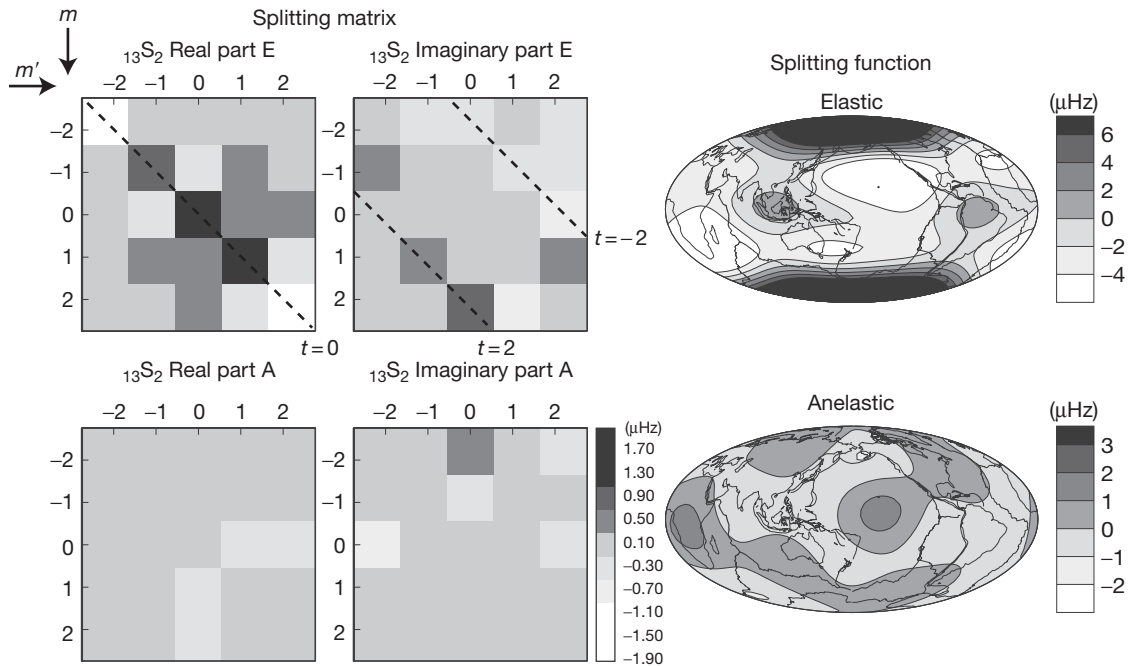


Figure 11 Left: Observed complete splitting matrix for mode ${}_{13}S_2$, decomposed into its elastic (E) and anelastic (A) parts, both of which are Hermitian. The data from 13 earthquakes were used to determine this matrix. The signal down the diagonal of the matrices is caused by zonal (axisymmetric) structure ($t=0$), as constrained by the selection rules for a mode. Also indicated are the contributions from $t=\pm 2$ -structure (which is sectorial for $s=2$). Right: Splitting functions obtained from the splitting matrix on the left. The signal from anelastic structure is typically much smaller than that from elastic structure.

Bearing this restriction in mind, a splitting function can be understood as the mode equivalent of a surface wave phase velocity map.

To summarize, an isolated mode of harmonic degree ℓ is sensitive to even-degree structure only, up to harmonic degree $s=2\ell$. If the structure within Earth is axisymmetric, then the splitting matrix is diagonal, the individual singlets can be identified by the index m , and the only singlet visible at a station at Earth's poles is the $m=0$ singlet.

1.04.2.2.2 Mode coupling

While the treatment of isolated modes is appealing because of its simplicity, it is insufficient to describe free oscillations of the real Earth. The coupling between modes has two fundamental effects: (1) varying coupling effects on individual singlets causes a shift of the mode's degenerate frequency and Q , and (2) coupling to certain other modes gives a mode sensitivity to odd-degree structure. We distinguish between along-branch (same mode type and n but different ℓ) and cross-branch coupling (any other mode combination). The coupling between two modes is particularly strong if their frequencies are close and the radial and geographic shape of their displacement field is similar. Numerically, the complex frequencies must be close, but in fact, the real part (frequency) is more dominant than the imaginary part (attenuation). As in the case of isolated modes, selection rules dictate through which mechanism and in which way two modes couple:

- Coriolis force causes spheroidal–toroidal mode coupling for mode pairs of the form ${}_nS_{\ell}-{}_nT_{\ell\pm 1}$, that is, between

multiplets that differ by a single angular degree ($|\ell-\ell'|=1$), for example, ${}_0S_4-{}_0T_3$, ${}_0S_8-{}_0T_9$, and ${}_1S_4-{}_0T_3$.

- Earth's ellipticity also causes spheroidal–toroidal mode coupling for $|\ell-\ell'|=1$.
- Earth's ellipticity causes same-type (spheroidal or toroidal) mode coupling for $|\ell-\ell'|=0$ and for $|\ell-\ell'|=2$, for example, ${}_0S_4-{}_1S_4$ and ${}_0S_3-{}_0S_5$.
- Rotation causes spheroidal–spheroidal mode coupling for $|\ell-\ell'|=0$, for example, ${}_0S_4-{}_1S_4$.
- Lateral heterogeneity of degree s causes spheroidal–toroidal mode coupling under the condition that $|\ell-\ell'|+1\leq s\leq \ell'+\ell-1$ and $\ell'+\ell+s$ is odd, for example, ${}_0S_4-{}_0T_3$ are coupled through structure of degrees 2, 4, and 6; as a consequence, if $|\ell-\ell'|$ is even, then modes can couple through odd-harmonic degree structure, for example, ${}_0S_5-{}_0T_3$ are coupled through structure of degrees 3, 5, and 7.
- Lateral heterogeneity of degree s causes same-type mode coupling under the conditions that (1) $m+t-m'=0$; (2) $\ell'+\ell+s$ is even; (3) $|\ell-\ell'|\leq s\leq \ell'+\ell$, for example, ${}_0S_2-{}_0S_3$ are coupled through structure of degrees 1, 3, and 5.

Coriolis coupling between fundamental spheroidal and toroidal modes was first observed and modeled by [Masters et al. \(1983\)](#). Coupling spheroidal–toroidal mode pairs form hybrid modes that share some of the characteristics of both modes. Toroidal modes can then be observed on vertical-component seismic spectra in the form of additional peaks, which Masters et al. nicely showed. For angular orders $7\leq\ell\leq 26$, ${}_0T_{\ell+1}$ modes are closer neighbors to ${}_0S_{\ell}$ modes than ${}_0T_{\ell-1}$ modes are. The strongest coupling occurs between pairs ${}_0S_{11}-{}_0T_{12}$ whose PREM degenerate frequencies are about

4.5 μHz apart (1 μHz for 1066A) and ${}_0S_{19}-{}_0T_{20}$ whose PREM frequencies are within 0.5 μHz of each other (2.5 μHz apart in 1066A). **Figure 12** shows that predicted frequency shifts for Coriolis-coupled modes can be up to 5 μHz , which is significant with respect to measurement errors (see **Figure 24**; regard a ‘strip’ as a spectral line of a mode for now). **Figure 12** also indicates that coupling modes ‘repel’ each other. For example, while the frequency of ${}_0S_{10}$ gets pulled downward, the frequency of ${}_0T_{11}$ gets pushed upward. The coupling between two multiplets actually has a different effect on each singlet of the modes, as is shown in **Figure 13**. As discussed in the

preceding text, for uncoupled modes, rotation and Earth’s hydrostatic ellipticity remove the frequency degeneracy. The coupling of the mode pairs causes the sets of mode singlets to rearrange. Strongly coupled modes form a hybrid pair in which the sets of singlet frequencies repel each other but the attenuation is ‘shared.’ As shown by [Masters et al. \(1983\)](#), Earth’s aspherical structure causes further rearrangement of the singlets.

Coupling between two modes also manifests itself in the splitting matrix. Instead of two matrices with ranks $2\ell + 1$ and $2\ell' + 1$ that describe the effects of rotation, ellipticity, and

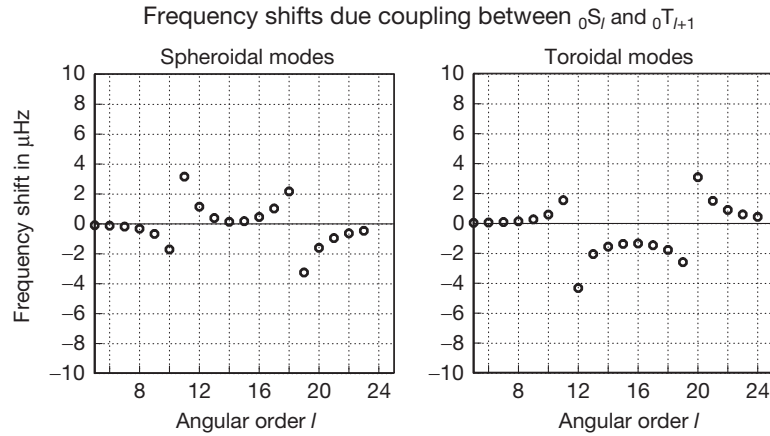


Figure 12 Predicted frequency shifts for mode pairs ${}_0S_\ell - {}_0T_{\ell+1}$ caused by Coriolis coupling. Predictions are for Earth model 1066A ([Gilbert and Dziewonski, 1975](#)). The strongest coupling occurs between pairs ${}_0S_{11} - {}_0T_{12}$ and ${}_0S_{19} - {}_0T_{20}$.

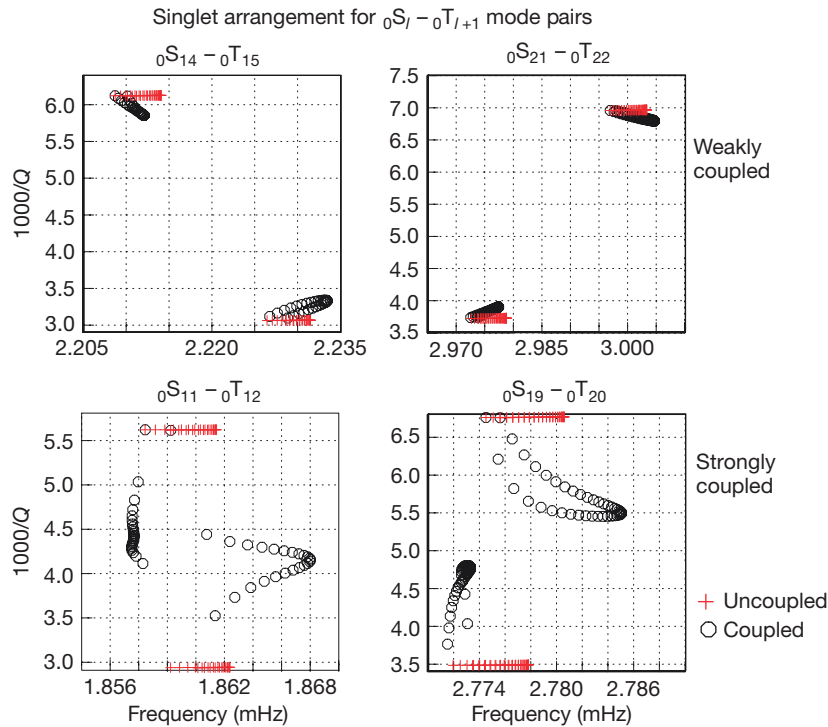


Figure 13 Predicted rearrangement of singlet frequencies and quality factor Q for weakly coupled-mode pairs ${}_0S_{14} - {}_0T_{15}$ and ${}_0S_{11} - {}_0T_{12}$ and for strongly coupled pairs ${}_0S_{21} - {}_0T_{22}$ and ${}_0S_{19} - {}_0T_{20}$. The coupling calculations included effects from both rotation and ellipticity, but for the modes discussed here, Coriolis coupling is the dominant cause. Strongly coupled modes form a hybrid pair in which the sets of singlet frequencies repel each other but the attenuation is ‘shared.’

structure for two modes, we now deal with a larger matrix with rank $2(\ell + \ell' + 1)$ that has four subblocks: the two original matrices that are now the two self-coupling blocks in the upper-left and lower-right corners, and two cross coupling blocks of dimensions $(2\ell + 1) \times (2\ell' + 1)$ and $(2\ell' + 1) \times (2\ell + 1)$. As an example of spheroidal–toroidal mode coupling, Figure 14 shows how Earth’s rotation and ellipticity affect the four coupling blocks in the splitting matrix for modes ${}_0S_4$ and ${}_0T_3$.

Earth structure can complicate the splitting matrix substantially, which we show in a schematic example for a $\ell = 2$ mode coupling with a $\ell' = 3$ mode of the same type (i.e., either spheroidal or toroidal). Figure 15 compares the structure of the splitting matrix in the case of the self-coupling of an isolated $\ell = 2$ mode and the upper-right cross coupling block with a $\ell' = 3$ mode. According to the selection rules, structure of certain symmetries affects certain elements in the splitting matrix. As already discussed, the effects from axisymmetric structure are found down the diagonal, while non-axisymmetric, even-degree structure affects off-diagonal elements (Figure 11). Depending on ℓ and ℓ' of the coupling modes, some elements in the cross coupling blocks are now affected by structure of odd-harmonic degree. An example of an observed splitting matrix is discussed in Section 1.04.2.3.5.

We should mention that the coupling calculations presented here were done with a code based on the work of Jeff

Park (Park and Gilbert, 1986). His method uses a Galerkin procedure that allows the assessment of mode coupling in a dissipating Earth. To reduce the computational burden, the method applies a trick. The exact representation of interaction on a rotating Earth requires a matrix equation that is quadratic in eigenfrequency ω . Coriolis interaction terms are grouped in a matrix linear in ω . This linear dependence is removed by replacing ω with a fixed fiducial frequency (reference frequency) $\hat{\omega}_0$. Park’s numerical experiments showed that this approximation is adequate for modes above 1 mHz as long as the relative frequency spread, $\Delta\omega/\hat{\omega}_0$, is not large. Modes in a certain frequency band all couple through various mechanisms. When modeling the interaction in a group of modes, all these have to be taken into account simultaneously. The examples of coupling mode pairs shown here are only to illustrate how mode coupling works and where Park and Gilbert’s method is appropriate. A treatment of coupling modes in a wider frequency band requires more general procedures. Some are discussed in Section 1.04.2.3.5, but the interested reader is also referred to Chapter 1.02.

1.04.2.3 Measuring Mode Observables

The most basic approach to extract mode observables from a seismogram is to calculate the spectrum of a tapered seismogram. The finiteness of the underlying time series prohibits a

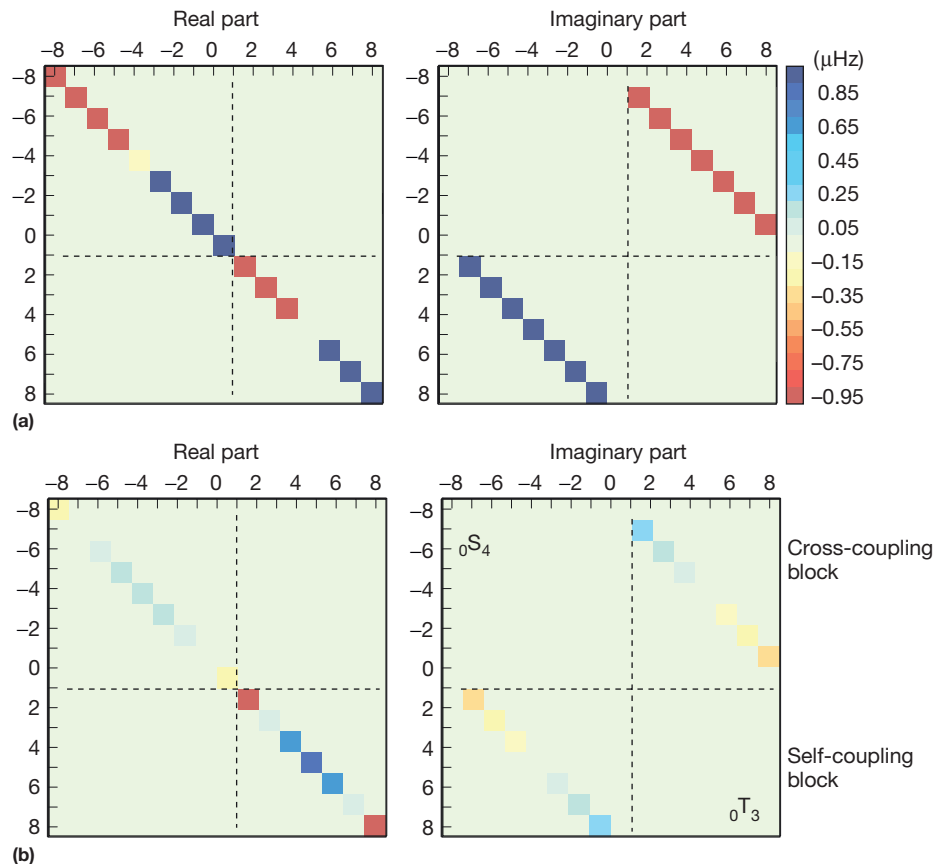


Figure 14 Synthetic splitting matrices to illustrate the coupling effect of Earth’s (a) rotation and (b) ellipticity on the mode pair ${}_0S_4 - {}_0T_3$. Self-coupling fills the diagonals of the self-coupling blocks, while multiplet–multiplet coupling fills the cross coupling blocks. For this pair, the effect of rotation is ten times larger than that of ellipticity.

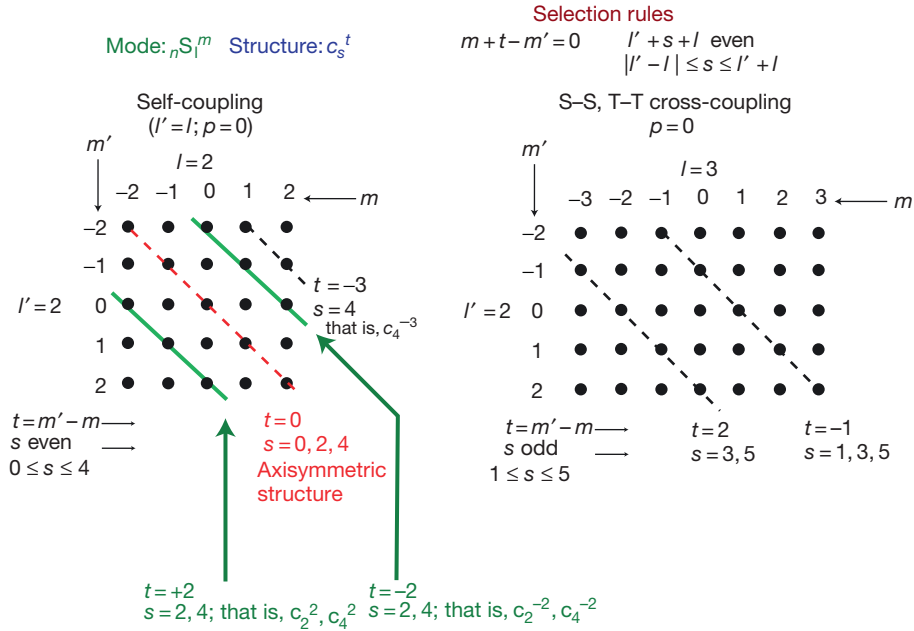


Figure 15 Elements in the splitting matrix that are affected by coupling. Left panel: An isolated $\ell=2$ mode experiences self-coupling through the Earth's rotation and ellipticity. Together with axisymmetric structure, this manifests itself in the diagonal. Other even-degree structure (s even) affects off-diagonal elements. When two modes couple, the splitting matrix has four blocks: two self-coupling blocks (one for each mode) and two cross coupling blocks. The right panel shows how elements in a cross coupling block with an $\ell'=3$ mode are affected for same-type coupling ($p=0$). Some of the elements are now affected by odd-degree structure (s odd).

parameter estimation with arbitrary precision (e.g., see [Jenkins, 1961](#) for an early assessment of the [Blackman and Tukey, 1958](#) approach). Modal decay rates, the vicinity of other modes, and the presence of noise necessitate the application of spectral optimization procedures, which involve the choice of a proper set of time windows. [Harris \(1978\)](#) presented a comprehensive overview on the use of windows in discrete Fourier analysis. Based on this, [Dahlen \(1982\)](#) first provided formal expressions for the variances and covariances of free oscillation parameters when using arbitrary data windows. He also showed that the optimum- or minimum-variance record length for measuring frequencies and decay rates (to determine Earth structure) using a Hanning taper is 1.1 Q cycles but only 0.5 Q -cycles for measuring amplitudes and phases (to determine the earthquake source). [Park et al. \(1987b\)](#) and [Lindberg and Park \(1987\)](#) adapted and applied [Thomson's \(1982\)](#) multitaper technique to optimize the bias from ambient noise and spectral leakage of decaying sinusoids in the free oscillation spectrum. Though we have not used this technique ourselves, they found that their approach provides a much improved detector for modes in a time series contaminated by white noise. Properly tapering free oscillation spectra is particularly important for measuring attenuation rates, which is discussed in [Masters and Gilbert \(1983\)](#). Complicating direct spectral estimation is the fact that, even today, it is not as trivial as it may appear to find continuous undisturbed seismic records that stretch over more than a week or so. A proper analysis of Earth's breathing mode ${}_0S_0$ requires records of more than two and half months! A somewhat disturbing fact is also that some continuous records that were available at the IRIS data management center (DMC) or other DMCs less than 10 years ago now have data gaps due to data storage failures. It is therefore essential to

understand how data gaps cause additional distortions in a complex spectrum. The best way to address this is by comparing a real data spectrum with a synthetic one that uses the same windowing and data gap structure, provided the source mechanism is known.

An obvious approach to assess Earth's 1-D and 3-D structure is to measure the apparent frequency of a certain mode for many stations and many earthquakes. Each of these 'peak shift data' can be plotted at the two poles of its source-receiver great circle. We make use of [Backus' \(1964\)](#) discovery that such data represent the great-circle integrals over surface spherical harmonics:

$$P_s(0)Y_s^t(\Theta, \Phi) = \frac{1}{2\pi} \oint_C Y_s^t(\theta, \phi) d\Lambda \quad [10]$$

where (Θ, Φ) is the positive pole of the source-receiver great-circle C and $P_s(0)$ is a Legendre polynomial. This representation can be used for peak shift data as long as the structural wavelength along the great circle is much longer than the modal wavelength ([Jordan, 1978](#)). Thus, we can extract the effects of Earth structure on a particular mode in an inversion for the structure coefficients of a splitting function (see eqn [9]). Examples of using this technique are the work of [Masters et al. \(1982\)](#), who found evidence for subducting slabs in the transition zone and [Romanowicz et al. \(1987\)](#) discussion of the degree 2 pattern of structure in the upper mantle. In principle, the c_0^0 term in the splitting function gives the degenerate mode frequency. In practice, an unbiased estimation of c_0^0 requires a large data set of peak shift measurements. More efficient tools to measure degenerate mode frequencies are based on mode stripping, which is laid out in the next section. Peak shift measurements to extract the effects of 3-D structure

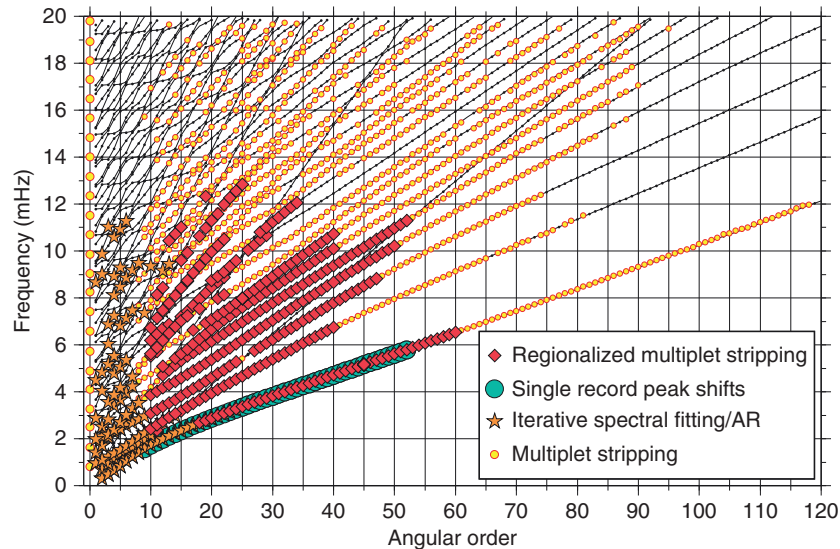


Figure 16 Spheroidal mode dispersion diagram (ω - ℓ plot) for spherical Earth model PREM. Different symbols indicate by which method a particular mode has been observed. Black dots are predicted modes that still await observation. The mode frequencies are published on the REM website except for the multiplet stripping results. Single record peak shifts refer primarily to the work of [Smith and Masters \(1989b\)](#). The first comprehensive ω - ℓ diagram showing observed modes was presented by [Dziewonski and Gilbert \(1972\)](#).

are only possible in spectra with high signal levels and at relatively high frequencies, where asymptotic theory is valid, which is typically the case only for fundamental modes. For other modes, this technique has been superseded by the regionalized stripping technique. The use of the different methods is summarized in [Figure 16](#) that includes only methods that we have used ourselves. Other methods include the time-lapse spectra approach used by [Dratler et al. \(1971\)](#) to measure attenuation rates of high- Q overtone modes. This method was also used by [Roult \(1974\)](#) and [Jobert and Roult \(1976\)](#) and others to determine attenuation rates for fundamental spheroidal and toroidal modes and the first few overtones. In this method, a sliding window of several hours (e.g., 6 h) is moved over a time series. An attenuation rate is then fitted to the collected amplitude values of a certain mode in a least-squares procedure. Our own (limited) experiments have shown that this technique gives accurate estimates as long as the spectral peaks are large and the frequency picked for the estimation is close to the observed peak shift frequency. Otherwise, oscillating amplitudes hamper the least-squares fitting procedure. For a discussion on mode attenuation rates, the interested reader is referred to [Chapter 1.21](#). Roult and colleagues made use of the time-variable filtering technique to extract individual mode branches from a seismogram prior to analysis. This technique is laid out in the surface wave section. [Romanowicz and Roult \(1986\)](#) showed in a later intriguing study that information on lateral heterogeneity can be obtained from records of a single station by modeling the fluctuations of frequency shifts along a mode branch, for different earthquakes, as explained theoretically by [Romanowicz \(1987\)](#).

1.04.2.3.1 Multiplet stripping and degenerate mode frequencies

In the multiplet stripping procedure, we ‘strip’ an overtone from a ‘stack’ of spectra. This process requires a large set of

recordings from different stations and events. The average location of a multiplet coincides with the multiplet degenerate frequency as long as the set of seismograms samples the globe evenly (condition 1) and as long as the distribution of singlets within a multiplet is relatively even (condition 2). Spectral stacking using a phase equalization procedure to extract free oscillation parameters was first used by [Mendiguren \(1973\)](#). Mode or multiplet ‘stripping’ was first introduced in the seminal paper of [Gilbert and Dziewonski \(1975\)](#) who used hand-digitized WWSSN recordings of the 1970 Colombian event and the 15 August 1963 Peru–Bolivia event. The set of mode frequencies they obtained constituted the bulk information in the construction of spherical Earth models 1066A, PEM-O/PEM-C/PEM-A ([Dziewonski et al., 1975](#)), and, finally, PREM ([Dziewonski and Anderson, 1981](#)) that is used as a REM still today.

In the multiplet stripping approach, we measure mode degenerate frequencies by linearly estimating multiplet resonance functions. In a second nonlinear step, a complex synthetic resonance function is fitted to the estimated resonance function to obtain the mode frequency and attenuation rate. With given starting models for the 1-D Earth and the earthquake source, the acceleration spectrum at the j th station, $u_j(\omega)$, can be computed as a weighted sum of multiplet resonance functions $c_k(\omega)$ (see eqn [4]):

$$u_j(\omega) = A_{jk} c_k(\omega) \quad [11]$$

Within narrow frequency bands, the multiplet excitation, A , can be considered constant and frequency-independent. Multiplet stripping consists in estimating the ‘multiplet strips’ $\hat{c}_k(\omega) = A_{jk}^{-1} u_j(\omega)$ in a least-squares sense, given observed spectra $u_j(\omega)$ and given the predicted multiplet excitations A_{jk} .

By applying multiplet stripping to large sets of seismograms, we can isolate individual multiplets even at frequencies where the spectrum of modes is dense compared to the line width. [Figures 17](#) and [18](#) show the result of multiplet

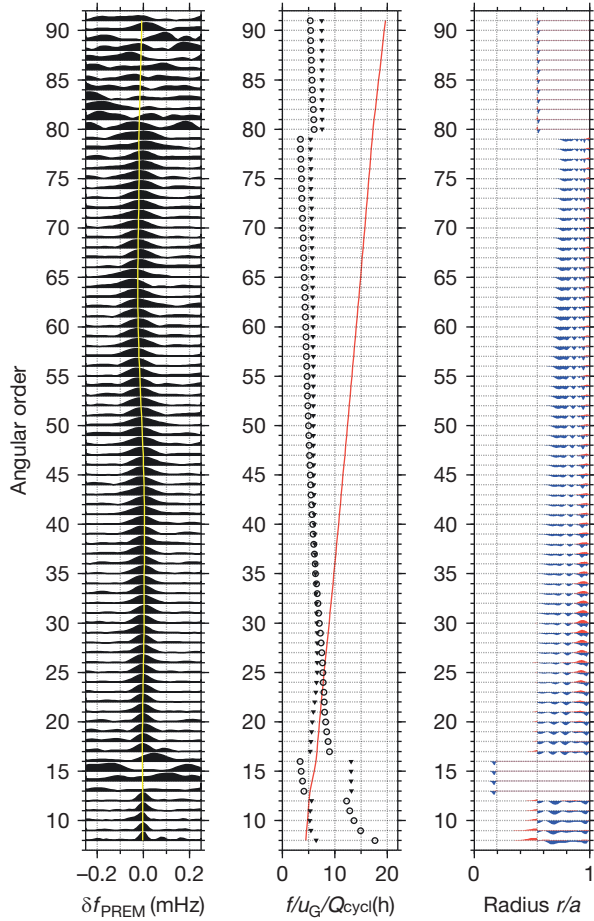


Figure 17 Multiplet strips for mode branch ${}_7S_\ell$, obtained from a data set of 12000 records of 260 events between 1991 and 1998. The left panel shows the strips for the individual modes centered on the predicted PREM frequencies. The middle panel shows the predicted degenerate frequencies (red line, mHz), group velocity (triangles, km s⁻¹), and Q cycles (circles, h). The right panel shows compressional (red) and shear (blue) energy densities. Multiplet stripping works well up to 17 mHz or angular order $\ell=79$ where the ${}_7S_\ell$ modes become Stoneley modes. Systematic deviations from PREM are evident in the left panel. The yellow line in that panel shows the predicted frequencies of MEMO0 (Valette and Lesage, 1992). This model seems to go a long way toward explaining the new observations even though it was constructed from a data set of modes below 5.4 mHz.

stripping for the two spheroidal mode branches ${}_7S_\ell$ and ${}_{23}S_\ell$. The frequency band covered by the strips is 0.5 mHz and contains as many as 200 toroidal and 300 spheroidal modes. Nevertheless, the good sampling of the globe provided by 12000 seismograms of 260 different events allows us to separate one mode from the others based solely on the shape of its eigenfunction and its excitation. The along-branch consistency such as exhibited by the mode group ${}_{23}S_{39} - {}_{23}S_{44}$ is a strong indication of the success of the method.

With the same large data set, we have tried to extract the radial modes ${}_nS_0$, which consist of only one singlet and hence cannot get split by aspherical structure. They are of particular interest because of their high sensitivity to density structure and to structure of the IC. Figure 19 shows the multiplet strips

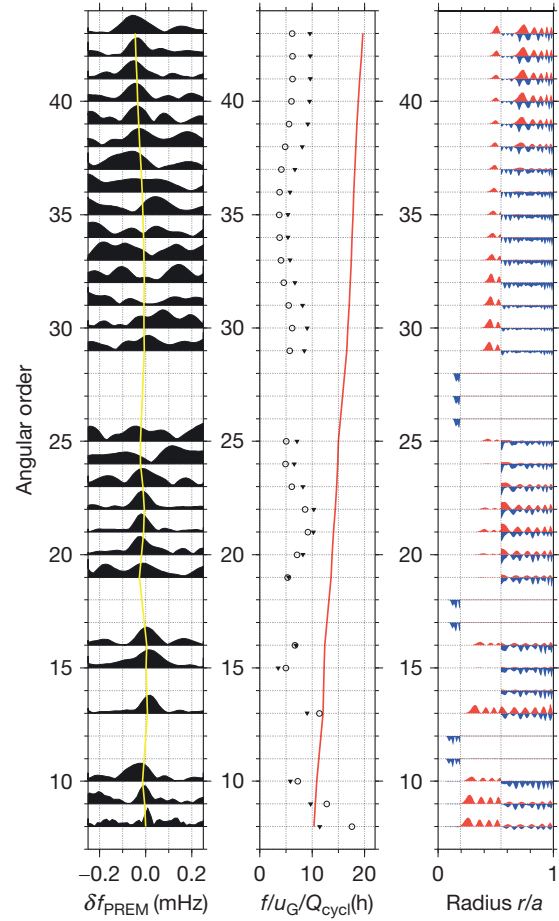


Figure 18 Multiplet strips for mode branch ${}_{23}S_\ell$, obtained from a data set of 12000 records of 260 events between 1991 and 1998. For well-excited multiplets with intermediate to high-quality factors, Q , and sensitivity to lower mantle and core structure, multiplet stripping works well up to 20 mHz. Systematic deviations from PREM are evident in the left panel, particularly between ${}_{23}S_{39}$ and ${}_{23}S_{43}$. For details, see Figure 17.

that we obtain for modes ${}_{10}S_0$ at 9 mHz through ${}_{23}S_0$ at 19.8 mHz. While for the two branches shown in Figures 17 and 18, the prediction of MEMO0 (Mean Earth MOdel) (Valette and Lesage, 1992) is in good agreement with the stripping results, neither PREM nor MEMO0 provides a satisfactory fit to our radial mode observations. The data set used for the construction of MEMO0 consisted of 617 mode degenerate frequencies in the period band 185–3230 s and included 198 toroidal, 10 radial, and 409 spheroidal modes from Masters and Widmer (1995). Whether the inability to fit radial mode observations requires new structure in the IC or whether it is due to coupling with nearby high- Q modes is still an open question.

As stated in the preceding text, one of the conditions for unbiased results is an even data coverage. In the long-wavelength limit of Jordan (1978), the sampling of the globe can be quantified by the density of great-circle poles. A scheme to optimize the selection of high signal-to-noise spectra that provide best possible sampling could minimize a possible bias. Unfortunately, large-size earthquakes and high-quality stations

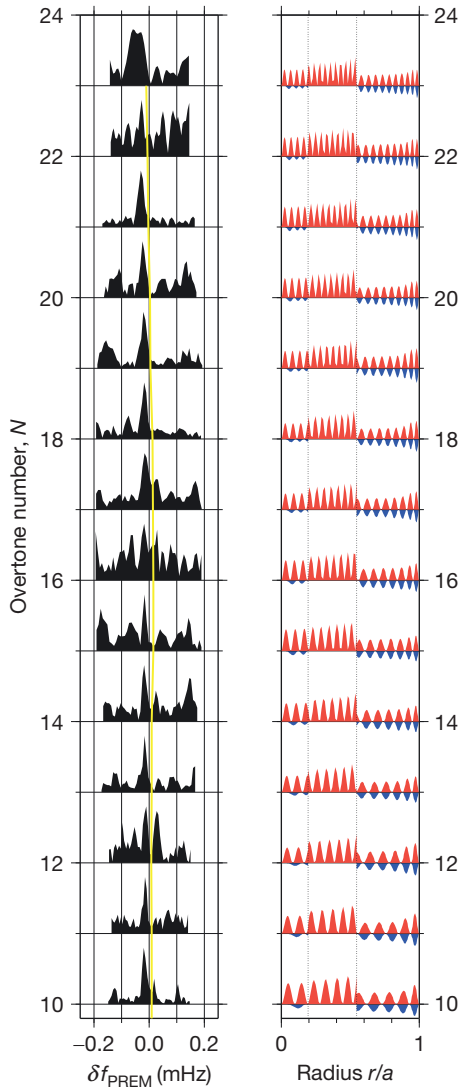


Figure 19 Multiplet stripping results for radial modes between 10 and 20 mHz. Strips with multiple peaks are likely due to coupling to nearby high- Q spheroidal overtones (Laske et al., 2001). The yellow line shows the predictions of MEM00. Neither PREM nor MEM00 gives a satisfactory fit to these modes. While a model with an additional first-order discontinuity in the inner core can explain the new radial mode frequencies, such a model leads to degradation of the fit of other IC-sensitive modes (B. Valette, personal communication, 2002). For details, see Figure 17.

are very unevenly distributed. These issues have been addressed with regionalized multiplet stripping by Widmer-Schnidrig (2002), where regular multiplet stripping is carried out for subsets of seismograms that sample only a particular great circle. While there is no substitute for missing data, regionalized multiplet stripping has at least allowed us to minimize the bias from long-wavelength structure. To date, about 30 years of high-quality digital seismic data enable us to successfully isolate individual modes to frequencies as high as 20 mHz. However, only the regionalized multiplet stripping results presented by Widmer-Schnidrig (2002), which stop at 12 mHz, are largely free of bias from 3-D structure because the data were

selected and weighted to specifically minimize this bias. The multiplet strips presented here maximize the signal-to-noise ratio at the expense of some geographic bias (i.e., some source-receiver great circles may dominate the coverage).

Condition 2 at the beginning of this section addresses pathological cases when one or more singlets are located far away from their neighbors. Isolated singlets with low spectral amplitudes are likely missed and omitted from the stripping. Examples are anomalously split IC-sensitive modes such as ${}_{13}S_2$ for which the $m=0$ singlet lies anomalously far away from the mode's degenerate frequency (see Figure 10). Multiplet stripping for such a mode can produce strips with two peaks: a large peak near the four singlets $m = \pm 1, 2$ and a small peak near the $m=0$ singlet. Estimating the multiplet frequency by fitting only a single resonance function to the large peak produces a biased degenerate frequency estimate. A still elusive mode is ${}_3S_2$ for which no reliable observations of the $m=0$ line exist, not even after the Sumatra–Andaman event. The reason for this is not fully understood, but possible causes include weak excitation, peculiar anelastic structure, and coupling to other modes. Fortunately, the splitting of many low- ℓ modes can be resolved fully so that their degenerate frequency can be estimated using other techniques. For high- ℓ overtones, which are analyzed exclusively with the multiplet stripping technique, this kind of extreme singlet distribution does not appear to be a problem.

1.04.2.3.2 Singlet stripping and receiver stripping

Historically, singlet stripping was the first method to dissect a multiplet into its singlets (Buland et al., 1979). While it is a robust technique, it has been superseded by the AR receiver stripping technique (Masters et al., 2000b). This is because the latter makes less assumptions about the shape of Earth's heterogeneity and also needs no accurate earthquake source model. Singlet stripping assumes that the dominant structure leading to splitting is axisymmetric. In this case, the splitting matrix \mathbf{H} (eqn [6]) remains diagonal. For the vertical component, one singlet frequency is then associated with a single Y_ℓ^m , as on the spherically symmetric Earth. The spectrum of a multiplet with angular order ℓ at the j th station, $u_j(\omega)$, can then be written as a weighted sum of singlet resonance functions $c_m(\omega)$:

$$u_j(\omega) = A_{jm}c_m(\omega) \quad \text{with } -\ell \leq m \leq \ell \quad [12]$$

where the singlet excitations, A_{jm} , have been computed based on eqn [4]. Equation [12] is an overdetermined system that can be solved for the 'singlet strips,' $\hat{c}_m(\omega) = A_{jm}^{-1}u_j(\omega)$. This procedure typically includes the records of many earthquakes.

In the receiver stripping approach, we treat each earthquake individually. Using eqns [4] and [5], we 'collapse' the set of spectra into a set of $2\ell + 1$ 'receiver strips,' for each earthquake and each mode:

$$\mathbf{b}(t) = \mathbf{R}^{-1} \cdot \mathbf{u}(t) = \exp[i(\mathbf{H} + \mathbf{I}\bar{\omega})t] \cdot \mathbf{a}(0) \quad [13]$$

We actually work in the frequency domain using spectra of Hanning-tapered records in a small frequency band about a multiplet of interest. Examples are found in Figure 20. The spectral lines in these diagrams are proportional to the spectra of individual singlets, if axisymmetric structure dominates the

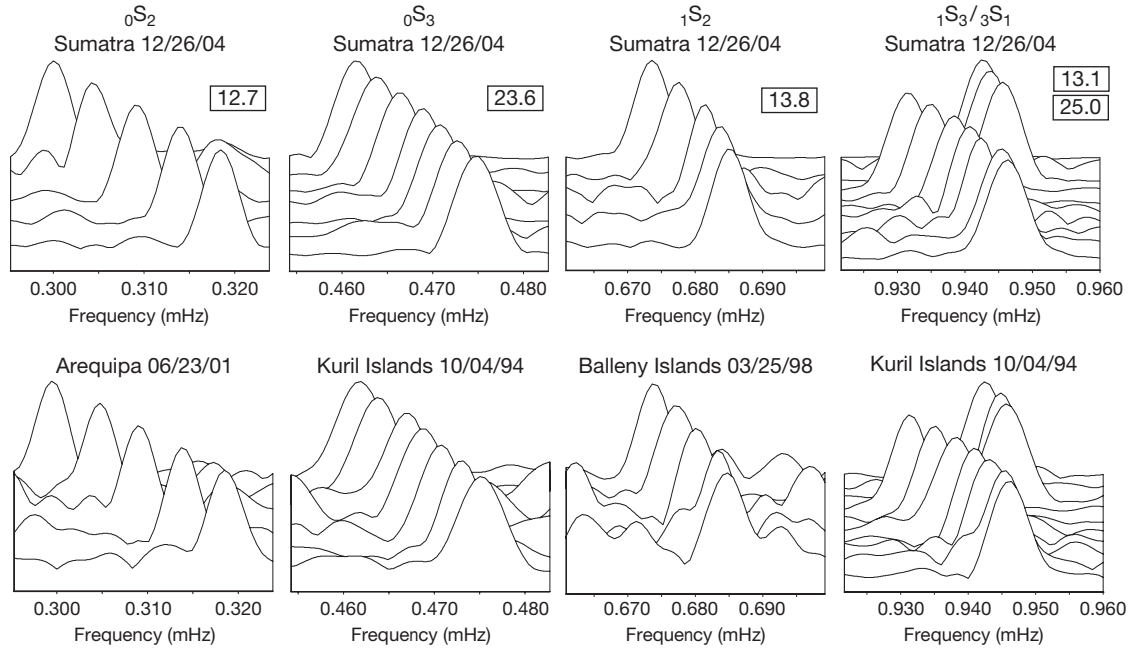


Figure 20 Normalized receiver strips for very low-frequency modes. For these modes, the splitting is dominated by axisymmetric structure, and the $2\ell + 1$ strips closely resemble the spectral lines of each singlet. The upper row shows the strips for the 2004 Sumatra–Andaman earthquake, while the lower row shows the best set of strips that we have had so far. The boxed numbers indicate how much larger the amplitudes of the Andaman strips are with respect to the best other earthquake.

splitting matrix. Modes $1S_3$ and $3S_1$ are so close together in frequency that their receiver strips overlap. A joint analysis prevents bias introduced when ignoring one of the modes.

1.04.2.3.3 Retrieving the splitting matrix with the matrix autoregressive technique

Figure 21 shows typical examples of spectra for IC-sensitive mode $13S_2$, and the steps involved going from seismograms (or spectra) to retrieve Earth’s internal structure. We use the autoregressive nature of the receiver strips to make our analysis technique for the splitting matrix independent of earthquake location and source mechanism. The receiver strips satisfy a recurrence in time. Using eqn [13], we obtain $\mathbf{b}(t)$ after the time increment δt :

$$\begin{aligned}\mathbf{b}(t + \delta t) &= \mathbf{R}^{-1} \cdot \mathbf{u}(t + \delta t) \\ &= \exp[i(\mathbf{H} + \mathbf{I}\bar{\omega})(t + \delta t)] \cdot \mathbf{a}(0) \\ &= \mathbf{P}(\delta t) \mathbf{b}(t)\end{aligned}$$

so

$$\mathbf{b}(t + \delta t) = \mathbf{P}(\delta t) \mathbf{b}(t), \quad \mathbf{P}(\delta t) = \exp[i\delta t(\mathbf{H} + \mathbf{I}\bar{\omega})] \quad [14]$$

which describes the autoregressive nature of $\mathbf{b}(t)$. Equation [14] has no term that depends on the seismic source. An inverse problem is set up for the propagator matrix \mathbf{P} , using the strips of many events simultaneously. The splitting matrix \mathbf{H} is determined from \mathbf{P} using the eigenvalue decomposition of \mathbf{P} (Masters et al., 2000b). The complex matrix \mathbf{H} we retrieve in this process is non-Hermitian (no symmetry) and includes elastic and anelastic structure. We use the unique representation

$$\mathbf{H} = \mathbf{E} + i\mathbf{A} \quad [15]$$

to decompose \mathbf{H} into its elastic, $\mathbf{E} = 1/2(\mathbf{H} + \mathbf{H}^H)$, and anelastic, $i\mathbf{A} = 1/2[\mathbf{H} - \mathbf{H}^H]$, components where superscript \mathbf{H} indicates Hermitian transpose. Both \mathbf{E} and \mathbf{A} are Hermitian and are the matrices for eqn [6] (where the effects of rotation and ellipticity are included in \mathbf{E}). Examples of splitting matrices retrieved with this technique are shown in Figures 11 and 25 in Section 1.04.2.3.5. A discussion on retrieving Earth’s density from splitting functions that were obtained using this method can be found in Masters et al. (2000c). An application to investigate the IC differential rotation is described Section 1.04.2.4.

1.04.2.3.4 Retrieving the splitting matrix with iterative spectral fitting

The first technique to retrieve all elements of the splitting matrix of an isolated multiplet was iterative spectral fitting (ISF) introduced by Ritzwoller et al. (1986), Ritzwoller et al. (1988), and Giardini et al. (1987). It has been refined and applied in a number of studies, including Li et al. (1991a), Li et al. (1991b), Widmer et al. (1992b), He and Tromp (1996), and Resovsky and Ritzwoller (1998). ISF considers the Fourier transform of eqns [4]–[6]. In this coupled set of equations, the $\ell - 1$ real and $\ell(\ell + 1)$ complex structure coefficients c_s^ℓ are nonlinearly related to the observed spectra $u_j(\omega)$. The problem of finding the structure coefficients from a set of observed spectra is then formulated as a nonlinear parameter estimation problem. Figure 22 shows an example of how ISF allows detailed modeling of a split mode spectrum. The prediction from a model including only Earth’s rotation and hydrostatic

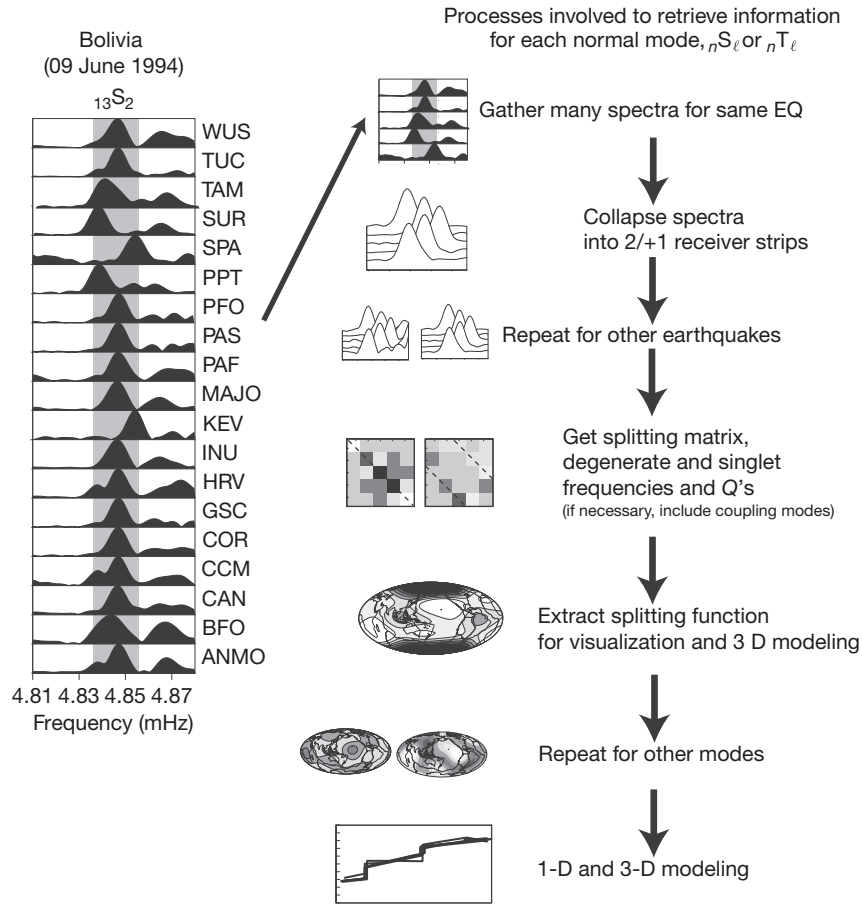


Figure 21 Left: Selected spectra for mode ${}_{13}S_2$, for the 1994 Bolivia earthquake. Right: Simplified flowchart of our approach to extract mode information from seismograms of large earthquakes.

ellipticity provides a poor fit to the observed spectrum. If ISF is implemented with a local search algorithm, this prediction can serve as starting solution. Spectral fitting is then iterated and converges to a new solution that fits the observation much better. The splitting of the mode shown here, ${}_1S_8$, reflects lower mantle V_S heterogeneity. A crucial aspect of ISF is the need of a source model so that the vector of singlet excitations $\mathbf{a}(0)$ in eqn [5] can be computed. Matters are further complicated, if local rather than the computationally more expensive global algorithms are used to search for the set of best-fitting structure coefficients. Nevertheless, for well-excited multiplets for which records from many events can be used simultaneously, it was possible with the data coverage of the 1980s to obtain robust estimates of degree $s=2$ and perhaps also $s=4$ structure coefficients.

ISF was also applied to high-Q, low-order modes up to 9 mHz (Widmer et al., 1992b). These modes sample the outer and inner core and many of the modes are anomalously split. The large majority of other modes attenuate so rapidly that the spectra are dominated by the relatively sparse class of high-Q modes, if the first 6–8 h of data after an earthquake are discarded. The set of structure coefficients of these high-Q

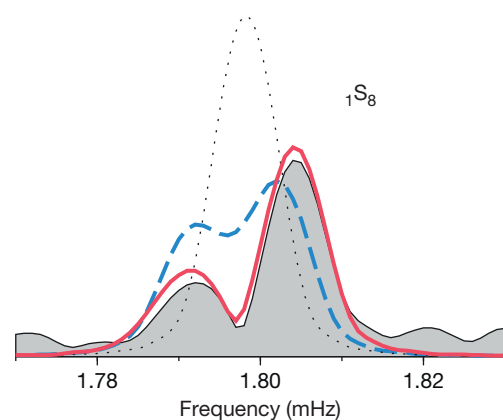


Figure 22 Modeling of the spectrum of multiplet ${}_1S_8$ with the ISF procedure, for a recording of the 9 June 1994 Bolivia earthquake at station MAJO (Matsushiro, Japan). Black line: Observed linear amplitude spectrum; dotted line: prediction for PREM; dashed blue line: splitting caused by Earth's rotation and hydrostatic ellipticity; red line: final solution for the spectrum after ISF. Spectra courtesy of Joe Resovsky, personal comm. 1998. Vertical ground displacement due to this mode at MAJO measured 10 μm .

modes analyzed by Widmer et al. (1992b) with both ISF and singlet stripping were used primarily by Tromp (1993) to corroborate the hypothesis of Giardini et al. (1987) that axisymmetric IC anisotropy can explain the anomalous splitting of IC-sensitive modes. The most comprehensive set of structure coefficients based on ISF was compiled by Resovsky and Ritzwoller (1998). Restricting their analysis to modes below 3 mHz, they obtained 3100 structure coefficients for 90 multiplets. These authors also generalized the ISF procedure to coupled modes and obtained, for the first time, constraints on odd-degree structure using normal modes (Resovsky and Ritzwoller, 1995). An updated mode data set obtained from using ISF is that of Deuss et al. (2013).

1.04.2.3.5 Observed mode coupling

As mentioned in the preceding text, we observe toroidal mode energy on vertical components because Coriolis coupling causes the formation of hybrid mode pairs in which energy is exchanged between modes. While this has been well observed for modes above 2 mHz, Zürn et al. (2000) recently also observed this for the gravest modes below 1 mHz (Figure 23). In gravimeter spectra of the great 1998 Balleny Islands earthquake, they identified spectral lines at the toroidal mode frequencies of ${}_0T_3$ through ${}_0T_6$. A correction of the LaCoste–Romberg gravimeter ET-19 record at station BFO for local atmospheric pressure variations (Zürn and Widmer, 1995) helped raise mode ${}_0T_3$ above the noise floor, while the spectrum of the superconducting gravimeter GWR-C026 at station J9 near Strasbourg also may have shown this peak. After the Sumatra event, Hu et al. (2006) observed the gravest toroidal mode ${}_0T_2$ and overtones ${}_1T_2$ and ${}_1T_3$ in gravimeter spectra. Using the method of Park and Gilbert (1986), Zürn et al. (2000) compared the effects of rotation, hydrostatic ellipticity, and aspherical Earth structure on coupled-mode synthetic spectra. They identified Coriolis coupling as the most effective mechanism responsible for toroidal mode energy to appear in the vertical-component spectra.

In the preceding text, we have described how the coupling of modes can lead to a frequency shift of the entire multiplet. An example is the Coriolis coupling between spheroidal and toroidal fundamental modes. The observation of Coriolis coupling is well documented for fundamental modes between 2 and 4 mHz (Masters et al., 1983; Smith and Masters, 1989a), and we recall that it is particularly strong for the two pairs ${}_0S_{11}$ – ${}_0T_{12}$ and ${}_0S_{19}$ – ${}_0T_{20}$. Figure 24 shows this mode coupling in an analysis where we applied the multiplet stripping technique. In general, the effect of multiplet–multiplet coupling on the degenerate frequency cannot be corrected for using this technique, except for the case shown here (e.g., Smith and Masters, 1989a). For multiplet–multiplet coupling caused by aspherical structure, it has to be assumed that the induced shift of the degenerate frequency can be treated as a source of random noise. This may be justified as the frequency separation to the nearest coupling partners is different for every multiplet so the cross branch coupling is different for every multiplet. For along-branch coupling, systematic effects may be significant, since the frequency separation of modes belonging to the same branch is nearly the same.

Coupling through Earth structure manifests itself in the cross coupling blocks of the splitting matrix. We have recently

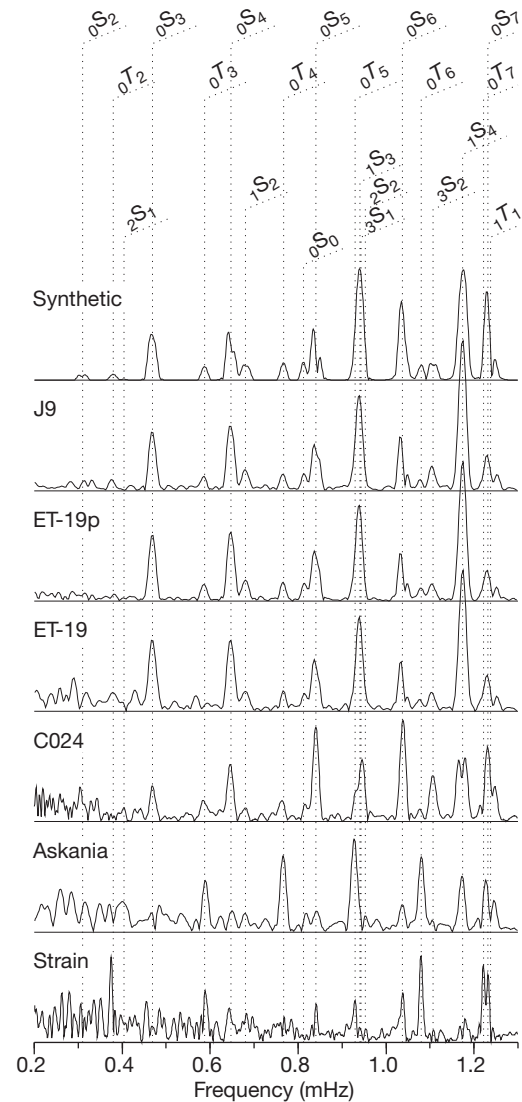


Figure 23 Coriolis coupling below 1 mHz, observed for the 25 March 1998 Balleny Islands earthquake. Spectral peaks appear in vertical-component spectra at the frequencies of toroidal modes ${}_0T_3$ through ${}_0T_6$. Shown are spectra of the LaCoste–Romberg spring gravimeter ET-19p at station BFO, the superconducting gravimeters GWR-C026 at station J9 near Strasbourg, 60 km from BFO, and GWR-C024 at Table Mountain Observatory near Boulder, CO (the United States). To reduce noise, the gravimeter records were corrected for variations in local atmospheric pressure (Zürn and Widmer, 1995). For comparison, the uncorrected spectrum at BFO is also shown (ET-19). The synthetic spectrum was obtained from a coupled-mode synthetic for BFO, using Park and Gilbert's (1986) method to account for effects from rotation, hydrostatic ellipticity, and aspherical structure. 'Askania' and 'strain' refer to data from the Askania borehole tiltmeter and the invar wire strainmeter array at BFO and show that the low-order fundamental toroidal modes were efficiently excited by the event. Reproduced from Zürn W, Laske G, Widmer-Schmidrig R, and Gilbert F (2000) Observation of Coriolis coupled modes below 1 mHz. *Geophysical Journal International* 143: 113–118.

started to apply the matrix AR technique to coupled modes, and an example for weakly coupled modes ${}_1S_5$ and ${}_2S_4$ is shown in Figure 25. Since the selection rules state that $\ell + \ell' + s$

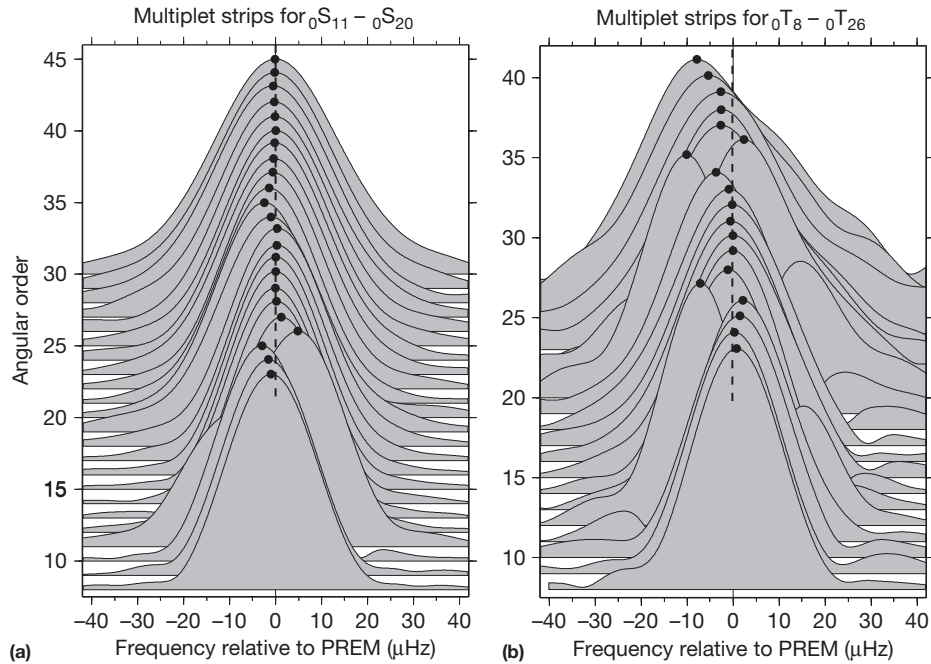


Figure 24 Observed effects of Coriolis coupling above 1 mHz. (a) Multiplet strips of fundamental spheroidal modes ${}_0S_8$ through ${}_0S_{30}$, aligned relative to PREM (Dziewonski and Anderson, 1981). (b) Multiplet strips of fundamental toroidal modes ${}_0T_8$ through ${}_0T_{26}$. Coupling effects are different for each singlet, resulting in a shift of the entire multiplet. Modes ${}_0S_{11}$ and ${}_0S_{20}$ are within a few microhertz of neighboring ${}_0T_{\ell+1}$ modes so coupling effects are particularly large. Coriolis coupling effects are significant for ${}_0S_9$ through ${}_0S_{22}$, relative to the observational uncertainties of $< 0.3 \mu\text{Hz}$. Modified from Widmer R (1991) *The Large-Scale Structure of the Deep Earth as Constrained by Free Oscillation Observations*. PhD Thesis, University of California San Diego, La Jolla, CA.

must be even, these two modes couple through structure of odd-harmonic degree. Coupling through Earth structure makes the splitting matrix quite complex, and the cross coupling blocks we determine with our technique may yet be too noisy to extract odd-degree structure. This should be improved in the future by including more earthquakes in the analysis. Resovsky and Ritzwoller (1995) successfully determined odd-degree structure implied in the cross coupling blocks by using the ISF method. In the example shown here, only a mode pair was considered, whereas Resovsky and Ritzwoller (1995) considered relatively small groups of modes below 3 mHz. Deuss and Woodhouse (2001) showed that wideband coupling can significantly alter the shape of spectral lines, though it is not immediately clear if this effect is significant with respect to measurement errors of mode observables.

Since the coupling strength scales with the inverse of the frequency separation of coupling modes, splitting matrices above 3 mHz become so large that their decomposition turns into a numerically formidable task. Several different strategies have been suggested to reduce the computational burden. Lognonné and Romanowicz (1990) and Lognonné (1991) introduced the efficient spectral method using third-order perturbation theory to compute coupled modes and seismograms for an anelastic rotating Earth. Using this method, Millot-Langet et al. (2003) calculated coupled-mode synthetics on an anelastic 3-D Earth. Deuss and Woodhouse (2004) introduced a method that is similar to subspace projection methods but can be iterated several times to completely represent the exact solution. They found that only one iteration

usually brings the solution sufficiently close to the exact solution.

Alternatives to the approach based on mode summation include the direct solution method (Geller and Takeuchi, 1995) for which an application to 3-D heterogeneity can be found in Takeuchi et al. (2000). The spectral element method of Komatitsch and Vilotte (1998) also has been shown to provide an efficient tool to study wave propagation, diffraction, and body-wave conversion in a 3-D Earth. Applications of this method can be found in Komatitsch and Tromp (2002), Komatitsch et al. (2002), Capdeville et al. (2003), and Chaljub and Valette (2004). Gilbert (2001) suggested that a Vandermonde matrix analysis allows the independent determination of earthquake mechanisms and Earth structure. The method also allows the analysis of 'latent' modes that are not observed but coupled to observed modes (e.g., modes with extremely little energy density near the surface). For a detailed discussion of numerical methods, the reader is referred to Chapter 1.07.

1.04.2.4 Example of a Mode Application: Inner-Core Rotation

Differential rotation of the IC with respect to the rigid mantle has been inferred by several body-wave studies, with most agreeing that a superrotation may exist with a rate between 0.2° and 3° per year (e.g., Creager, 2000; Song and Richards, 1996). The wide range of inferred rotation rates is caused by the sensitivity of such studies to local complexities in structure, which have been demonstrated to exist. Free oscillations, on

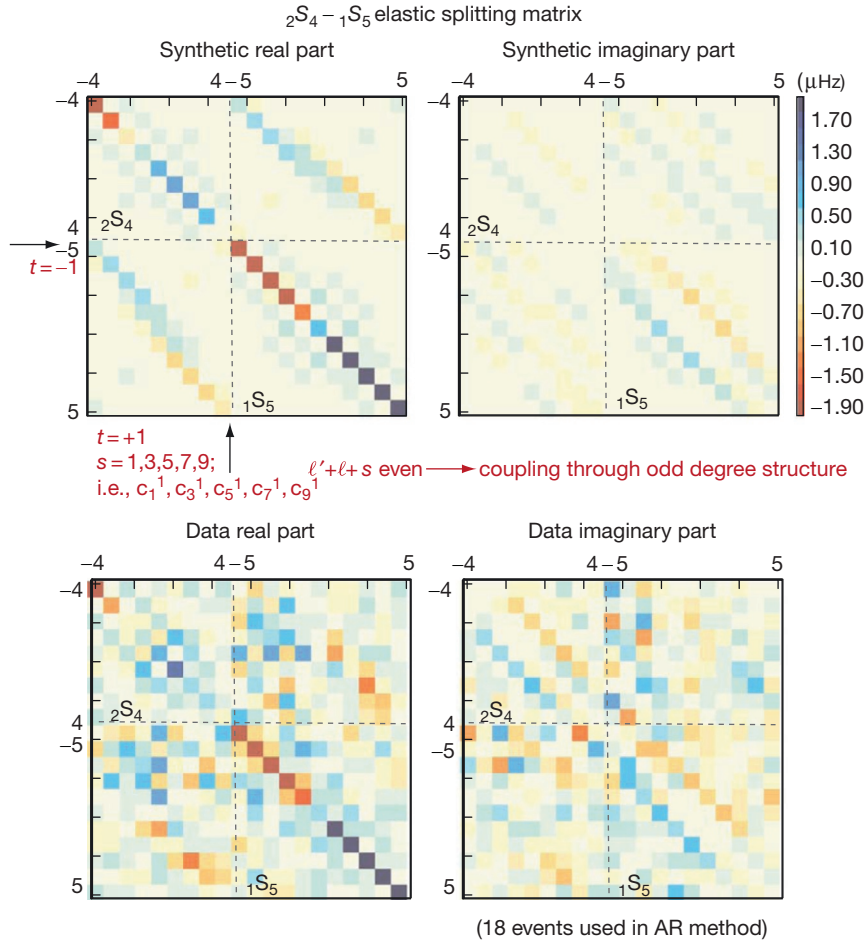


Figure 25 Predicted and measured elastic splitting matrix \mathbf{E} of the coupled-mode pair ${}_1S_5 - {}_2S_4$. The signal in the diagonal self-coupling blocks is generally somewhat larger in the observations than in the predictions (e.g., imaginary part for mode ${}_2S_4$). Some predicted features show up in the measured off-diagonal cross coupling blocks (e.g., blue in upper-left corner and red toward the lower right in the real part), but noise probably inhibits a reliable extraction of odd-degree structure from these blocks at this time. The 3-D model used for the synthetic splitting matrix is S16B30 (Masters et al., 1996). Reproduced from Masters TG, Laske G, and Gilbert F (2000d) Large-scale Earth structure from analyses of free oscillation splitting and coupling. In: Boschi E, Ekström G, and Morelli A (eds.) *Problems in Geophysics for the New Millennium*, pp. 255–288. Bologna: Editrice Compositori.

the other hand, are natural low-pass filters of 3-D structure, so that long-wavelength phenomena, such as IC rotation, are prime study targets. Free oscillations ‘see’ Earth as a whole, so the observation of how a free oscillation splitting pattern changes with time, and any inference on IC rotation is not biased by the effects of localized structures. It is also not necessary to know the physical cause of the patterns (anisotropy or heterogeneity). All that needs to be observed is if and how they change with time. Free-oscillation splitting functions are therefore better candidates for estimating differential IC rotation accurately. The most obvious approach to do this analysis is to compare splitting functions obtained with earlier earthquakes to those obtained with recent events. A problem with this approach is that the sparsity of early data does not allow us to construct early splitting functions with the required accuracy. Sharrock and Woodhouse (1998) therefore studied the time dependence of the fit of splitting functions to spectra of earthquakes over time for some IC-sensitive modes. Their estimates of a westward rotation of the IC with respect to the

mantle appear to be inconsistent with the results from body-wave studies. We prefer to use our autoregressive technique for this analysis.

In a hypothesis test, we sought the optimal IC rotation rate that matches our splitting functions for the recent earthquakes with receiver strips over time. Our initial finding was that the IC rotation is essentially zero over the last 20 years ($0.01 \pm 0.21^\circ \text{year}^{-1}$; Laske and Masters, 1999). A complication in this analysis – that also plays a role in many body-wave studies – is that IC-sensitive modes are also very sensitive to mantle structure. Prior to applying the assumed IC rotation rate in the test, we therefore have to correct for the contributions from the heterogeneous mantle. In a detailed and updated analysis, Laske and Masters, (2003) applied mantle corrections using a variety of published mantle models (Figure 26). Our preferred model is SB10L18 (Masters et al., 2000a), a 10-degree equal area block model that was derived simultaneously for shear velocity and bulk sound speed, $V_C = \sqrt{\kappa/\rho}$, and our mode data were included in the

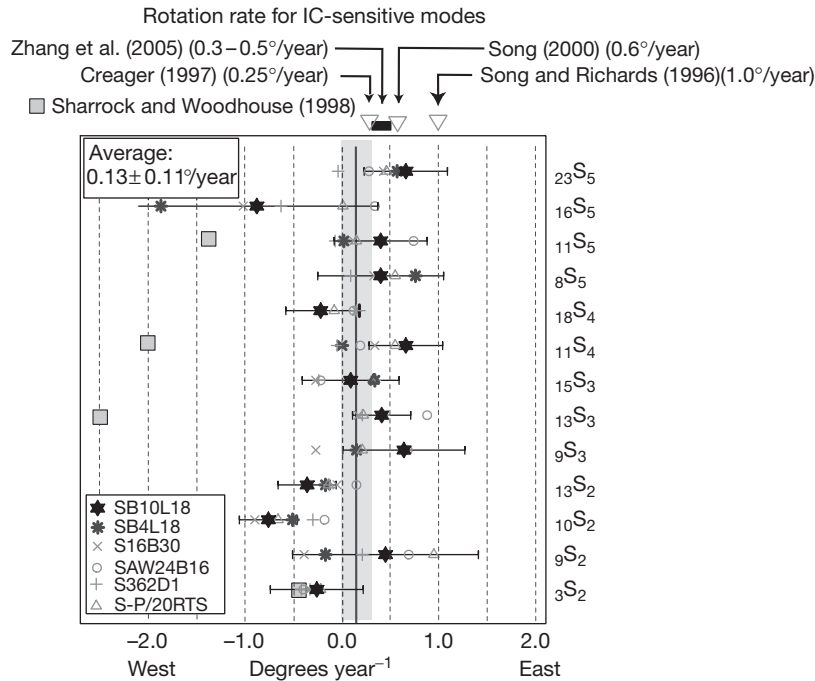


Figure 26 IC rotation rates obtained for 13 IC-sensitive modes, using our preferred $V_S/V_O/V_P$ mantle model SB10L18 (Masters et al., 2000a). Also shown are the results obtained using other mantle models: shear velocity models SB4L18 (Masters et al., 2000a), S16B30 (Masters et al., 1996), SAW24B16 (Mégnin and Romanowicz, 2000), and S362D1 (Gu and Dziewonski, 1999) and V_S/V_P models S-P/20RTS (Ritsema and van Heijst, 2000). Other symbols and lines mark results from other publications: Song and Richards (1996), Creager (1997), Sharrock and Woodhouse (1998), Song (2000), and Zhang et al. (2005).

inversions. The majority of models in the literature are shear velocity models that were derived using only shear-sensitive modes (e.g., SAW24B16 by Mégnin and Romanowicz, 2000) or using established scaling relationship for V_P and ρ (or ignoring sensitivity to the latter entirely) to include spheroidal modes (e.g., S20RTS by Ritsema and van Heijst, 2000). Our comparison also includes our older model S16B30 (Masters et al., 1996) that was the result of a direct matrix inversion for a model described by spherical harmonics. As can be seen from Figure 26, inferred rotation rates vary with different mantle models, but most results lie within our error bars for SB10L18. Laske and Master's best estimate is a barely significant super-rotation of $0.13 \pm 0.11 \text{ year}^{-1}$, which is still consistent with the idea that the IC is gravitationally locked to the mantle. A more recent estimate of $0.00 \pm 0.06 \text{ year}^{-1}$ that is based on data up to and including the 2011 Tohoku, Japan, earthquake was presented at the 2011 General Assembly of the EGU (Masters, 2011). These results are broadly consistent with many body-wave results (e.g., Creager, 1997, 2000) though the discrepancy to a recent body-wave estimate of $0.3\text{--}0.5 \text{ year}^{-1}$ by Zhang et al. (2005) is marginal but still significant.

There are limitations to this type of analysis, and not all IC-sensitive modes can be utilized. For example, although $\ell=1$ modes (e.g., ${}_8S_1$ and ${}_{13}S_1$) are quite sensitive to IC structure, they can constrain IC rotation only poorly because the mantle-corrected splitting functions are dominated by a large zonal (axisymmetric) component. Also, so far, we have ignored mode coupling in our analysis. Some IC-sensitive modes significantly overlap in frequency with other modes of high angular order ℓ , thereby hampering an analysis using the receiver

strip method. For example, with a degenerate frequency in PREM (Dziewonski and Anderson, 1981) of 1.242 mHz, mode ${}_2S_3$ is very sensitive to IC shear velocity but overlaps with ${}_0T_7$, ${}_0S_7$, and ${}_1T_1$, which couple through Earth's 3-D structure. For a given mode pair ${}_0S_\ell/{}_0T_\ell$, we need at least $2 \times (\ell' + \ell + 1)$ high-quality records to construct receiver strips. These many records are often not available for earlier earthquakes. Many $\ell=2$ modes that are very sensitive to IC structure are strongly coupled to radial modes. We can analyze such mode pairs with our AR technique, but the IC rotation hypothesis test becomes more cumbersome and was not done in our 2003 study. We notice that mode ${}_{13}S_2$, which couples with ${}_5S_0$, and mode ${}_{10}S_2$, which couples with ${}_4S_0$, systematically suggest a westward IC rotation, regardless of the mantle model chosen for the corrections. The analysis of ${}_3S_2$, whose coupling properties with neighboring modes is quite complex (see also Zürn et al., 2000), also gives westward rotation rates. Mode ${}_9S_2$ is difficult to observe and errors are quite large. When not taking these modes into account, we obtain an eastward IC rotation rate of $0.34 \pm 0.13^\circ/\text{year}^{-1}$. This marginally agrees with the estimate of Zhang et al. (2005).

A caveat when analyzing modes using the isolated-mode assumption is that only even-degree structure can be determined. It is known from body-wave studies that the heterogeneity at the top of the IC has a strong $s=1$ signal that is roughly divided into a Western and an Eastern Hemisphere (Creager, 2000; Tanaka and Hamaguchi, 1997). The fact that isolated modes are insensitive to such structure does not invalidate our IC rotation results, provided the IC rotates as a rigid body. Structure of odd-harmonic degree can potentially be determined

by analyzing coupled modes, but the coupling effects for the modes considered here are rather weak. Core structure and IC differential rotation are discussed in [Chapter 1.23](#).

1.04.2.5 Example of a Mode Application: Earth's Hum

It took as long as 38 years after the first observation of Earth's free oscillations of the 1960 Great Chilean earthquake before convincing evidence was found that Earth's normal modes never cease to vibrate but instead remain excited at a low but nearly constant level ([Ekström, 2001](#); [Suda et al., 1998](#); [Tanimoto et al., 1998](#)). This normal mode background signal is now often termed Earth's 'hum.' Early on, [Benioff et al. \(1959\)](#) looked for modal signals in noise spectra of LaCoste-Romberg gravimeters, but the sensitivity of these instruments (which at the time were operated with a mechanical feedback) was too low by three orders of magnitude for a positive hum detection. It was not until [Nawa et al. \(1998\)](#) first inspected data from the superconducting gravimeter at Syowa (Antarctica) and subsequently from seismic stations of the global network ([Suda et al., 1998](#)) that evidence for the incessant excitation of seismic free oscillations was presented.

Fundamental spheroidal modes ${}_0S_\ell$ are observed to be permanently excited in the frequency band 2–7 mHz, with an root mean square acceleration amplitude of ~ 1 ngal ($=10^{-11}$ ms $^{-2}$) over a 100 μ Hz bandwidth ([Figure 27](#)). Additional characteristic hum features are a slight semiannual modulation of the amplitude and a resonant enhancement near 3.7 mHz ([Ekström, 2001](#); [Nishida et al., 2000](#)). At frequencies below 2 mHz, vertical seismic noise is primarily of local barometric origin, and some of this noise can be removed by regression with the locally recorded pressure fluctuations ([Zürn and Widmer, 1995](#)). However, this crude correction does not allow to remove all of the barometric noise, making a hum detection below 2 mHz nearly impossible. At frequencies near 7 mHz, the splitting of the fundamental spheroidal modes due to heterogeneous upper-mantle structure is as wide as the frequency separation between adjacent fundamental modes. Modes then overlap and cause an overall rise of the noise base level into which peaks disappear. [Nishida et al. \(2002\)](#) showed that the vertical-component seismic noise consists of globe-circling Rayleigh waves all the way up to 20 mHz, and it seems likely that the same mechanism is responsible for the generation of Rayleigh wave background noise as for the hum at lower frequency. The detection of the hum is an instrumental challenge because of its exceptionally small amplitude. The self-noise of all instruments that have so far been able to detect the hum is at or very near the amplitude of the hum itself. These include superconducting gravimeters, LaCoste-Romberg spring gravimeters, and Streckeisen STS-1 and STS-2 seismometers. [Widmer-Schnidrig \(2002\)](#) computed coherences for pairs of colocated sensors and in the hum band obtained values not exceeding 0.5. The low signal-to-noise ratio in individual traces necessitates much averaging in time or the use of array techniques to enhance the hum signal.

The physical processes responsible for the excitation of the hum remain somewhat of a puzzle. Considering that wave motion in the oceans is responsible for the marine microseisms at periods shorter than ~ 25 s and that below 2 mHz atmospheric phenomena dominate the seismic noise, one can speculate that

the signals in between are also generated by atmospheric and/or hydrospheric processes. The semiannual modulation supports this hypothesis, while the resonant enhancement near 3.7 mHz ([Nishida et al., 2000](#)) is evidence for at least partial involvement of the atmosphere (e.g., [Widmer and Zürn, 1992](#)). The lack of overtones in the hum favors near-surface excitation and also speaks for the atmosphere and/or hydrosphere excitation hypothesis. From the observation that individual mode excitations do not correlate between pairs of stations, [Nishida and Kobayashi \(1999\)](#) had drawn the conclusion that the source of the hum cannot be localized but must be of global origin: they hypothesize that pressure exerted on the solid Earth by global atmospheric turbulence is responsible for the hum excitation. This conclusion, however, is not compelling because of the low signal-to-noise ratio mentioned in the preceding text.

Trying to elucidate the hum excitation mechanism, [Rhie and Romanowicz \(2004\)](#) used the BDSN (Berkeley Digital Seismic Network) in California and the F-net in Japan to estimate the back azimuth of the Rayleigh wave background signal. They located hum sources in the North Pacific during Northern Hemisphere winter and in the southern oceans during summer. A subsequent analysis of 5 years of data from the GRSN (German Regional Seismic Network) in Germany found back azimuths consistent with these source regions ([Kurlle and Widmer-Schnidrig, 2006](#)). [Figure 28](#) shows that the back azimuths of Rayleigh waves at GRSN also have a very pronounced seasonality. Prevalent winter back azimuths around 30° point toward the North Pacific, while summer back azimuths of 210° and 120° point to the southern Pacific and southern Indian Ocean, both in accordance with [Rhie and Romanowicz \(2004\)](#). More recently, [Rhie and Romanowicz \(2006\)](#) studied two winter storms off the west coast of N America during four seismically quiet, consecutive days. As the storms encountered the coast, the amplitude of both the marine microseisms and the low-frequency Rayleigh waves increased, and both wave types could be traced back to the same coastal segment where the storms hit the shore.

While the generation of microseisms by ocean surface gravity waves is well understood (e.g., [Kedar et al., 2008](#); [Languet-Higgins, 1950](#)), it is not entirely clear how the band-limited surface gravity waves are linked to the occurrence of infragravity waves and subsequently the generation of low-frequency Rayleigh waves. One particular difficulty in this chain of linked phenomena is the mismatch of wave numbers between open-ocean infragravity waves on the one hand and Rayleigh and Love waves on the other: at a given frequency in the hum band, the wavelength of Rayleigh and Love waves is 25 times larger than that for infragravity waves in the deep ocean.

Infragravity-wave generation is most efficient on the continental shelf and involves nonlinear wave-wave interactions (e.g., [Galagher, 1971](#); [Tanimoto, 2005](#); [Webb, 1998](#)). [Rhie and Romanowicz \(2006\)](#) observed hum excitations not only along the west coast of North America, where the infragravity waves were originally generated, but also along the North Pacific Rim after the waves apparently traveled there and dissipated. The timing was found to be consistent with the propagation speed of ~ 200 ms $^{-1}$ for infragravity waves in the open ocean. If infragravity waves are capable of exciting the hum to observable levels after crossing entire ocean basins, this may explain why previous attempts at locating the source

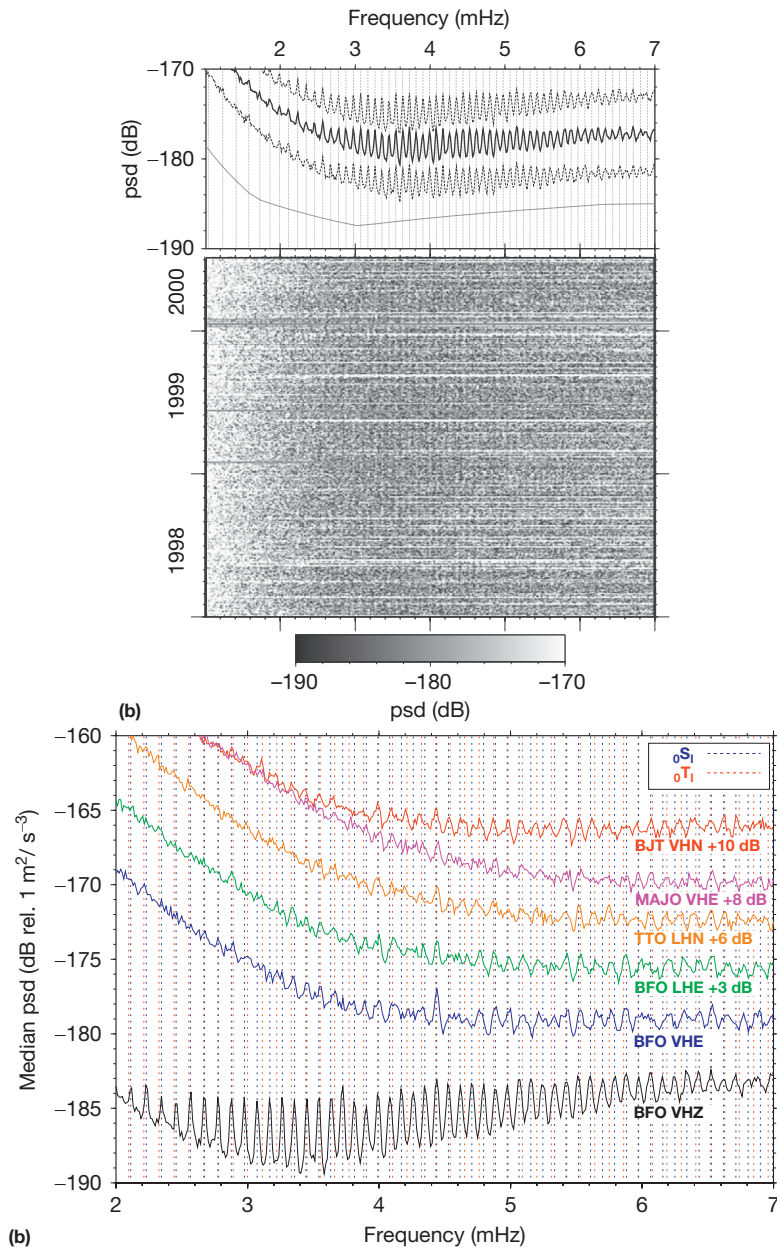


Figure 27 (a) Time–frequency plot covering 2.5 years of data from the STS-2 seismometer of the German Regional Seismic Network (GRSN) at BFO. The range of the gray scale is chosen to emphasize structure in the noise during seismically quiet times. The upper panel shows median psd levels (black) together with the first and third quartiles (dashed). The new low noise model of Peterson (1993) (gray) is shown for reference. The vertical dashed lines indicate the predicted frequencies of the fundamental spheroidal modes ${}_0S_1$ and coincide with light-gray vertical bands in the lower panel. (b) Comparison of vertical and horizontal hum. The bottom trace (BFO VHZ) with the regular comblike structure shows the spheroidal hum recorded on the vertical-component STS-1Z seismometer at BFO. The traces above show spectra of the horizontal hum recorded at four different stations of the GSN, F-net, and GRSN seismic networks: BFO, TTO, MAJO, and BJT. The richer spectrum of the horizontal hum is due to the interference of fundamental spheroidal and toroidal modes. The different horizontal hum spectra are offset for clarity. (Kurrle and Widmer-Schmidrig, 2008).

regions of the hum produced only very diffuse maps (e.g., Nishida and Fukao, 2007). More recent studies based on data from the large, transportable USArray (292 stations with an aperture of 2000×1200 km) confirmed the shelves as the dominant source region in times of large oceanic storms (Bromirski and Gerstoft, 2009). However, whether the

processes invoked to explain the observations from large winter storms are representative for the persistent background hum excitation remains an open question.

Owing to higher noise levels in horizontal component seismic recordings, it took another 10 years after the discovery of the spheroidal hum to discover its counterpart in horizontal

recordings. A horizontally polarized hum consisting of spheroidal modes was to be expected because the particle motion of spheroidal modes (and Rayleigh waves) follows an ellipse in a vertical plane. However, the discovery of the horizontal hum included also a big surprise: it consisted also of toroidal modes, and the latter were present with equal or even larger amplitudes than the spheroidal modes (Figure 27(b)). Kurrle and Widmer-Schmidrig (2008) estimated the ratio of toroidal-to-spheroidal signal power at 4 mHz to be close to unity, while at 12.5 mHz, Nishida et al. (2008) estimated the power of Love waves to be three times larger than for Rayleigh waves.

Initially, the large fraction of toroidal energy posed a serious challenge to the models of hum excitation. At the time, these models consisted of predominantly vertical forces from pressure fluctuations of infragravity waves on the shelf or in the deep ocean that in turn lead to an excitation of spheroidal modes (e.g., Tanimoto, 2005; Webb, 2007). However, vertical pressure forces acting on a horizontal sea floor excite exclusively spheroidal modes and lead to no excitation of toroidal modes. Fukao et al. (2010) proposed a model for spheroidal and toroidal hum excitation, which could resolve this conundrum. In its simplest form, this model can be described as follows: consider a patch of sea floor with a periodic bathymetry consisting of linear sinusoidal hills (e.g., abyssal hills), and let a monochromatic infragravity wave with the same wavelength as the bathymetry propagate over this patch in a direction perpendicular to the bathymetric hills. The pressure field acting on the sloping sea floor can now be decomposed into vertical and horizontal pressure forces: while the resulting vertical forces oscillate rapidly with position, the horizontal pressure forces are not oscillating spatially but point in the same direction for the entire patch. This model achieves two things: (1) it overcomes the mismatch in wave numbers between infragravity waves and seismic surface waves, and (2) it provides a mechanism with a predominantly horizontal

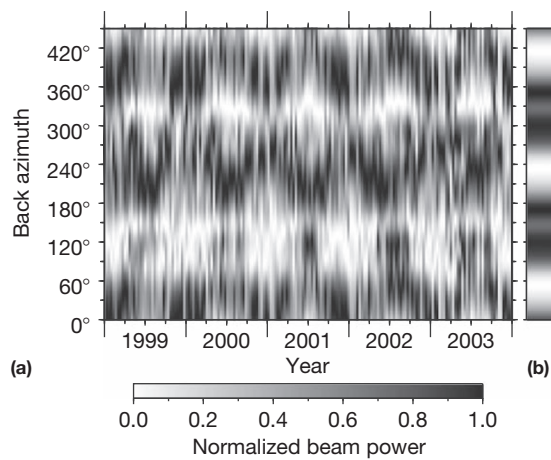


Figure 28 (a) Beam power distribution of Rayleigh wave background between 5 and 8 mHz estimated from vertical-component recordings of a nine-station array in Central Europe. (b) Back azimuths of an incident plane wavefield cannot be recovered perfectly from a sparse nine-station array. This is evident from the array response shown here. (Kurrle and Widmer-Schmidrig, 2006).

force, which naturally leads to the excitation of Love and Rayleigh waves with comparable amplitudes.

While identifying the processes that lead to the excitation of the hum needs further study, Nishida et al. (2009) succeeded in using the hum signal to infer 3-D upper-mantle shear wave velocity structure. Their work is closely related to the emergent field of ambient noise tomography, which is discussed in the surface wave section and in Chapter 1.12. For a more detailed discussion of the hum, the interested reader is referred to the excellent review article by Nishida (2013).

1.04.3 Surface Waves

1.04.3.1 Standing Waves and Traveling Waves

Surface waves provide a rich data set to explore Earth's crust and upper mantle as well as seismic sources on a multitude of scales (see Romanowicz, 2002 for a comprehensive review). Many papers document that there is no real boundary between free-oscillation and surface wave measurements. For example, early free-oscillation papers that discuss great-circle surface wave dispersion actually discuss free-oscillation peak shifts (e.g., Roullet and Romanowicz, 1984). Studying long-period surface waves, Souriau and Souriau (1983) found a plate subduction-related degree 2 anomaly in the transition zone that was similar to that of Masters et al. (1982) using their mode approach. In fact, surface wave theory on the spherical Earth can be understood as a high-frequency approximation of mode theory. As mentioned in the mode section, the motion of standing waves on a sphere is expressed in spherical harmonics. At epicentral distance Δ , standing waves along a source–receiver great circle are described by zonal harmonics where the Legendre polynomials $P_\ell(\cos \Delta)$ are the relevant terms (Figure 29). In the high-frequency or high- ℓ asymptotic expansion, this term is approximated by cosines which are the relevant terms of traveling waves (e.g., Aki and Richards, 1980, 2002; Jordan, 1978; Romanowicz and Roullet, 1986) to zeroth order in $1/\ell$ (see Romanowicz, 1987, for higher-order expansion):

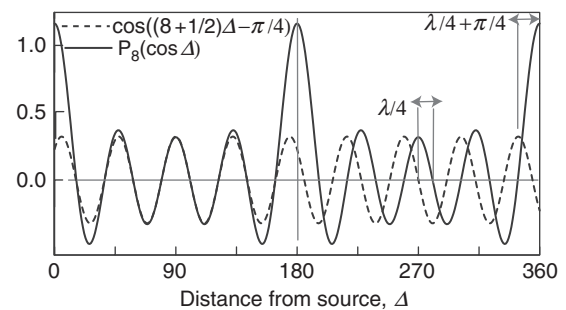


Figure 29 A comparison of the degree 8 Legendre polynomial with its asymptotic representative. The scaling factor of eqn [16] was omitted, but a constant factor was applied for optimal illustration. The graph also illustrates the validity of Jeans' formula. The asymptotic representation is applicable strictly only near $\Delta = 90^\circ$. After passing a pole, the asymptotic leads by $\pi/2$ or approximately a quarter wavelength where $\lambda = 2\pi/(\ell + 1/2)$. Entering and exiting a pole each add $\pi/4$.

$$P_\ell(\cos\Delta) \simeq \left(\frac{2}{\pi\ell \sin\Delta}\right)^{\frac{1}{2}} \cos\left[\left(\ell + \frac{1}{2}\right)\Delta - \frac{\pi}{4}\right] \quad [16]$$

Away from the poles, Jeans' formula (Jeans, 1923) gives the approximate wave number, k , of such a cosine:

$$k = \frac{\ell + \frac{1}{2}}{a} \quad [17]$$

where a is Earth's radius.

Dahlen and Tromp (1998) described the conversion from the standing wave to the traveling wave representation through the Watson transformation

$$\sum_{\ell=0}^{\infty} f\left(\ell + \frac{1}{2}\right) = \frac{1}{2} \int_C f(k) e^{-ik\pi} \cos(k\pi)^{-1} dk \quad [18]$$

where f is any function that is analytic near the real k -axis and C is a closed contour along the positive real k -axis (see also box 9.7 in Aki and Richards, 2002 and box 9.3 in Aki and Richards, 1980). This demonstrates how a sum over discrete modes

(standing waves) is expressed as an integral over continuous wave number (traveling waves).

Approaching the problem from the other end, to observe a free-oscillation spectrum, the time series has to include at least a pair of wave trains traveling in opposite directions as well as a third wave train that circled Earth, that is, the time window has to be at least roughly 5 h long (Figure 30; see also Figure 3). The synthetic seismograms that Figure 30 is based on were calculated for an epicentral distance of nearly 90° . In this case, the fundamental mode spectra are modulated such that often, every other mode has a significantly reduced amplitude though this modulation also depends on the source. For the examples shown here, we assume a double-couple point source. A seismogram including only one wave train carries no information on the finite body Earth; hence, we do not observe normal modes. As soon as a major arc wave train and a minor arc wave train are recorded, an amplitude modulation pattern emerges that depends on the epicentral distance and the source mechanism. If two wave trains are recorded that are separated by a complete great circle, modes can be observed though

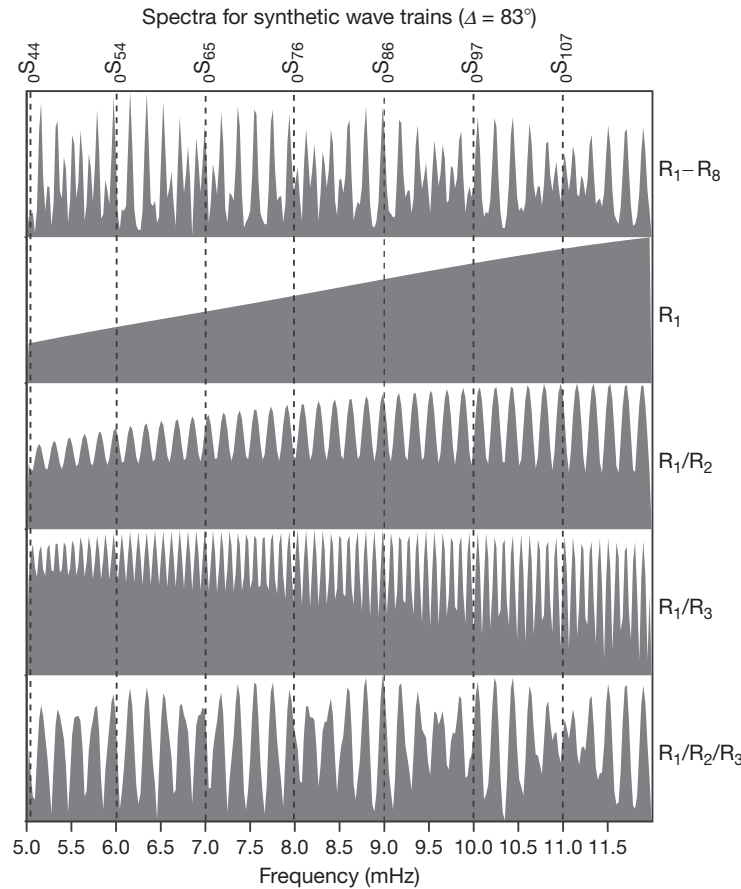


Figure 30 Spectra of synthetic acceleration seismograms at an epicentral distance of 83° , with a variety of wave trains as indicated on the right. All time series are 12 h long. Only the top spectrum contains all wave trains that arrive at a station within 12 h. Wave trains in the other records were zeroed out. A Hanning taper was applied before calculating the spectra. The full amplitude modulation is apparent only after three wave trains are recorded at a station. The combination R_1/R_3 is an unrealistic case but demonstrates that wave trains separated by a full great circle carry mode information (see also the caption in Figure 4). The seismograms were calculation with a mode summation code based on MINOS (see Section 1.04.2.1).

without this amplitude modulation. This peculiar behavior becomes clear when we discuss the representation of a surface wave seismogram on the spherical Earth.

Away from the poles, surface waves traveling on the spherical Earth can be expressed by

$$s(t) = \frac{1}{2\pi} \int_{-\infty}^{\infty} A_s(\omega) e^{-\alpha(\omega)t} \times e^{i(\omega t - k(\omega)x + (N-1)\pi/2 + \Phi_s(\omega))} d\omega \quad [19]$$

where A_s is the source amplitude, $\exp(-\alpha(\omega)t)$ describes the attenuation along the path, Φ_s is the source phase, and $i(\omega t - kx)$ describes the evolution of the phase along the travel path. Brune et al. (1961) first described and experimentally verified that surface waves traveling on a sphere experience a $\pi/2$ phase shift each time the wave passes a pole. This is accounted for by the term $(N-1)\pi/2$, where N is the wave orbit number. The polar phase shift can be explained by the fact that eqn [16] is a good approximation only for distances $< 180^\circ$ where the $P_\ell(\cos \Delta)$ are in phase with the cosines (Figure 29). For distances $180^\circ < \Delta < 360^\circ$, this representation lags by a quarter of a wavelength, or $\pi/2$. Note that we ignore the scaling factor of eqn [16] in Figure 29. Including this factor provides a better match in amplitudes for a wider distance range away from 90° , but the factor is singular near the poles. From a traveling wave perspective, the poles are locations of caustics where an approaching surface wave from one direction is not defined (e.g., Romanowicz and Roullet, 1986; Schwab and Kausel, 1976b; Wielandt, 1980). Using eqn [19], we can also understand how two wave trains that are separated by a complete great circle interfere to form standing waves. The contributions of the two wave trains to the seismogram are largest (constructive interference), when the phase difference between the two, $\delta\Psi(\omega) = -2\pi k\Delta(\omega) + \pi$, is an integer multiple of 2π , that is, $\ell 2\pi$. This results in Jeans' formula.

The surface wave analog to measuring mode frequency shifts is the measurement of phase velocity, $c(\omega) = \omega/k$, which is achieved by measuring the phase, $\Psi = -kx$. Two principal hurdles impede a straightforward analysis. The first hurdle has to do with the time series in general. Surface wave packets are nonstationary and the phase changes rapidly with frequency. It is therefore not practical to extract accurate phase estimates using a simple periodogram technique. The second hurdle comes from the fact that we use the approximation in eqn [16], which is a high- ℓ asymptotic. Wielandt (1980) pointed out that, at a given frequency, Jeans' formula gives only an average wave number on a sphere, which changes with travel distance, so the phase velocity also changes. The measured phase velocity, which he termed 'dynamic phase velocity' (Wielandt, 1993), is the asymptotic one only at distance $\Delta = 90^\circ$ but slower at shorter distances and faster at longer ones. The 'dynamic phase velocity' is attached to the wavefield (which includes the nonuniform amplitude on a spherical Earth; see Figure 29) and is not to be confused with the 'structural phase velocity' that we seek, which, in the case of a 1-D Earth, is the asymptotic phase velocity. Wielandt (1980) suggested to apply correction factors for waves that do not cross a pole. He estimated that ignoring such factors can amount to errors of 1%, which is of the same order of magnitude as phase perturbations caused by structure. This consideration is relevant only at extremely long periods beyond 300 s ($\ell \approx 25$) where these factors become significant, given modern

measurement errors. Schwab and Kausel (1976b) provided graphs of correction factors for Love waves for certain travel distances and earthquake source mechanisms. We prefer to measure phase perturbations with respect to a reference model by determining the transfer function between an observed and a mode synthetic seismogram. This implicitly reduces the variation of phase with frequency (hurdle 1). It accounts for the polar phase shift and source phase automatically and fully accounts for the approximation of eqn [16] (hurdle 2). A phase perturbation $\delta\Psi(\omega)/\Psi(\omega)$, caused by lateral heterogeneity, is then

$$\frac{\delta\Psi(\omega)}{\Psi(\omega)} = -\frac{1}{\Delta} \int_0^\Delta \frac{\delta c(\omega)}{c_0(\omega)} dx \quad [20]$$

where $\Psi(\omega)$ is the frequency-dependent phase accumulated along the perturbed travel path, Δ is the travel distance, and $c_0(\omega)$ is the frequency-dependent reference phase velocity. Equation [20] is correct to first order in lateral heterogeneity. Romanowicz (1987) and Pollitz (1994) calculated higher-order contributions that arise from gradients perpendicular to the great-circle path. Pollitz concluded that the second-order effect is insignificant in the determination of long-wavelength structure up to harmonic degree 12 (anomalies of scale 1500 km and larger). Ignoring higher-order contributions may cause a bias in phase velocity maps for structure significantly beyond harmonic degree 16 (anomalies smaller than 1200 km) though the impact of this on models obtained with large global data sets requires further investigation.

On a sphere, it is convenient to expand lateral heterogeneity in terms of surface spherical harmonics $Y_l^m(\theta, \phi)$ as a function of geographic coordinates θ and ϕ , so that $\delta c/c_0$ is

$$\frac{\delta c(\omega)}{c_0(\omega)} = \sum_{l=0}^{L_M} \sum_{m=-l}^l c_l^m(\omega) Y_l^m(\theta, \phi) \quad [21]$$

where the c_l^m are complex coefficients and L_M is the maximum harmonic degree to which lateral phase velocity variation (a 'phase velocity map') is expanded. Note that l and m here describe structure, while the ℓ and m in the modes section describe a normal mode.

Considering the parameterization of eqn [21], it is interesting to plot the integral kernels in eqn [20] to examine how phase perturbations depend on lateral heterogeneity. In Figure 31, we notice that sensitivity falls off with harmonic degree in structure though it is initially relatively high, for short travel distances. The sensitivity to even-degree structure decreases relative to odd-harmonic degrees, up to a travel distance of 180° , at the antipode of the source. Then sensitivity evens out up to 240° travel distance, which corresponds to R_2 , the major arc wave train for an epicentral distance of 120° . After that, the relative sensitivity to odd harmonics falls below the sensitivity to even harmonic degrees, until it is zero at 360° , when a wave train completed a great circle. Recall that we had mentioned in the mode section that waves lose sensitivity to odd-degree structure as time goes on and that eqn [10] (Backus, 1964) shows that a complete great-circle integral over Y_l^m 's has no sensitivity to odd-degree structure.

Phase velocity maps derived exclusively from great-circle data are equivalent to the mode splitting functions in

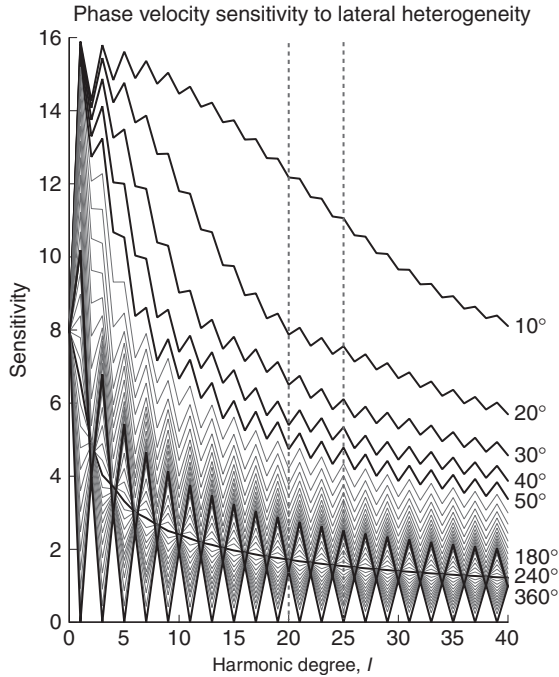


Figure 31 Phase sensitivity to lateral heterogeneity (integral kernel of eqn [20]), as function of harmonic degree in structure. Curves are shown for travel distances between 10° and 360° . Paths with distance $< 180^\circ$ are for minor arc paths (R_1); larger distances are for major arc paths (R_2).

eqn [9], except that phase velocity maps are measured at fixed frequency, ω , and splitting functions at fixed wave number, k (or ℓ). From the cyclic relation for partial differentiation (e.g., Riley et al., 2002),

$$\left(\frac{\partial\omega}{\partial m}\right)_k \cdot \left(\frac{\partial m}{\partial k}\right)_\omega \cdot \left(\frac{\partial k}{\partial\omega}\right)_m = -1$$

where m is a model parameter, we can derive a conversion factor between splitting functions and phase velocity maps,

$$\left(\frac{\delta\omega}{\omega}\right)_k = \frac{u}{c} \cdot \left(\frac{\delta c}{c}\right)_\omega \quad [22]$$

where $c = \omega/k$ and $u = \partial\omega/\partial k$ are the phase velocity and group velocity (see next paragraph). An example of this relationship is shown in Figure 32 where both maps were obtained by inverting our standing and traveling wave observations. The patterns in the maps, caused by lateral heterogeneity within Earth, are quite similar visually, and the correlation between the maps is above the 99% confidence level (Laske and Masters, 1996). Small variations that are numerically barely significant may result from differences in the data sets and inversion schemes used. We can therefore convince ourselves that analyzing standing and traveling waves results in the same models of even-degree Earth structure.

The phase velocity is the speed at which a certain point in the wave train travels, while a certain point of the envelope (or the energy) travels with the group velocity (see Figure 36(b) for concept). Both together define the dispersion of surface waves, and a last comparison with modes is done here. In the

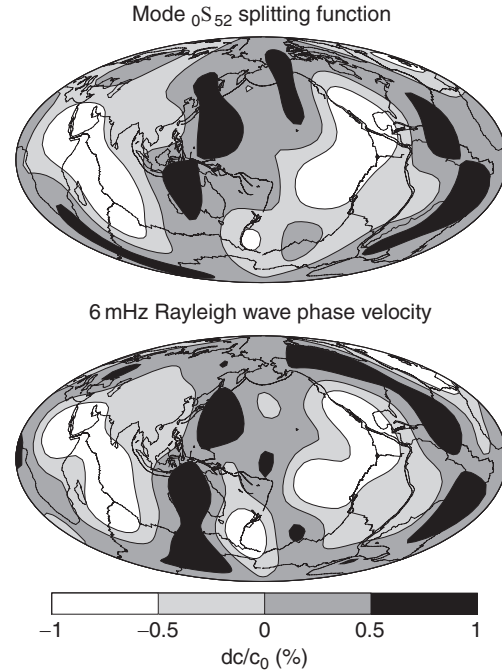


Figure 32 Comparison of effects of 3-D structure on standing waves (splitting function) and traveling waves (phase velocity map). The splitting function was converted to phase velocity perturbation using the conversion factor given by eqn [22]. Only even harmonic degrees are shown for the Rayleigh wave map to make it compatible with the splitting function of an isolated mode that is not sensitive to odd harmonics. Both maps are truncated at harmonic degree 8 (Laske and Masters, 1996).

mode section, we introduced the ω - ℓ dispersion diagram (Figure 16) that shows mode frequencies as a function of mode identifiers n and ℓ . Using Jeans' formula (eqn [17]), which is valid for $\ell \gg n$, this diagram implicitly summarizes the dispersion of surface waves (Figure 33). For most Rayleigh wave frequencies, we observe normal dispersion with $c > u$, or $dc/dk < 0$. An exception is the range below 2 mHz, where we observe anomalous dispersion, $u > c$, or $dc/dk > 0$. In the range of low-frequency modes below $\ell = 25$, c/u increases until c is roughly 42% larger than u , and then it decreases. At frequencies above about 6 mHz, c/u approaches 1 and variations in local peak shift can be related directly to phase velocity variations. Group and phase velocities for Love waves are typically larger than those for Rayleigh waves at the same frequency, except above roughly 50 mHz when the Love wave group velocity drops off significantly for oceanic structure (see next section). Also, c/u starts to approach 1 at much lower frequencies than for Rayleigh waves.

1.04.3.2 The Measurement of Fundamental Mode Dispersion

For surface waves, dispersion is usually presented in frequency-velocity (or period-velocity) diagrams (Figures 34 and 35). Before we elaborate on measurement techniques, we briefly summarize some early observations of surface wave

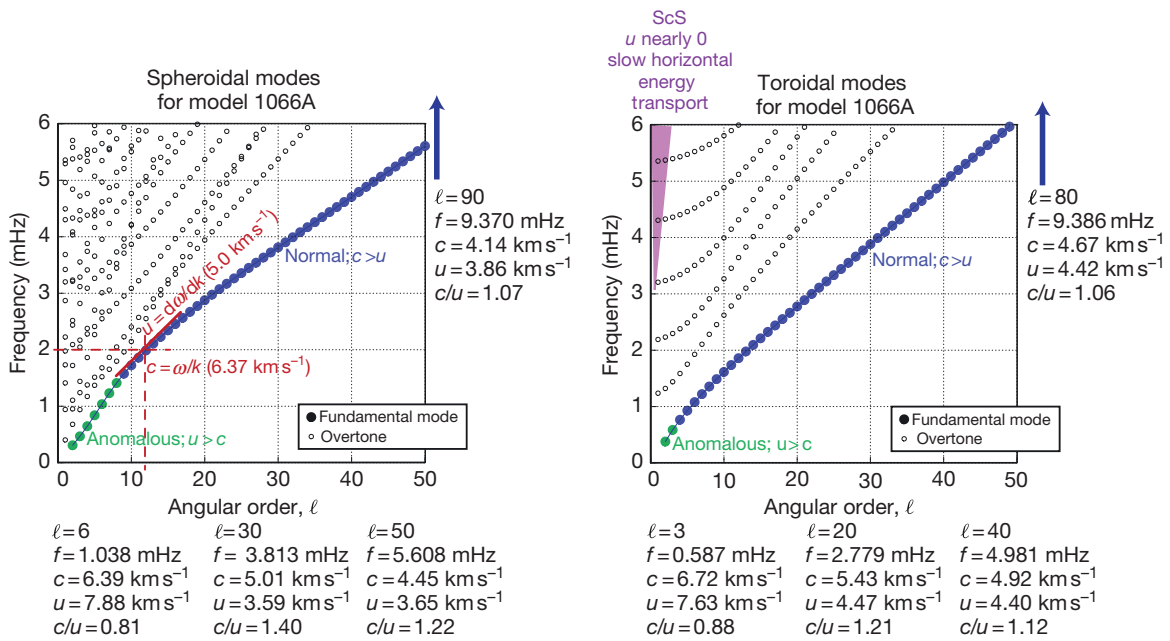


Figure 33 Dispersion diagram (ω - ℓ plot) for spheroidal and toroidal modes for model 1066A of Gilbert and Dziewonski (1975). Red lettering describes the concept of phase (c) and group (u) velocity for mode ${}_0S_{12}$. Blue symbols mark fundamental modes with normal dispersion ($u < c$), while green symbols mark modes with anomalous dispersion ($u > c$). The purple area marks the location of ScS equivalent modes whose group velocity is nearly zero. The scalar c/u is used to convert splitting functions to phase velocity maps (see Figure 32; eqn [22]).

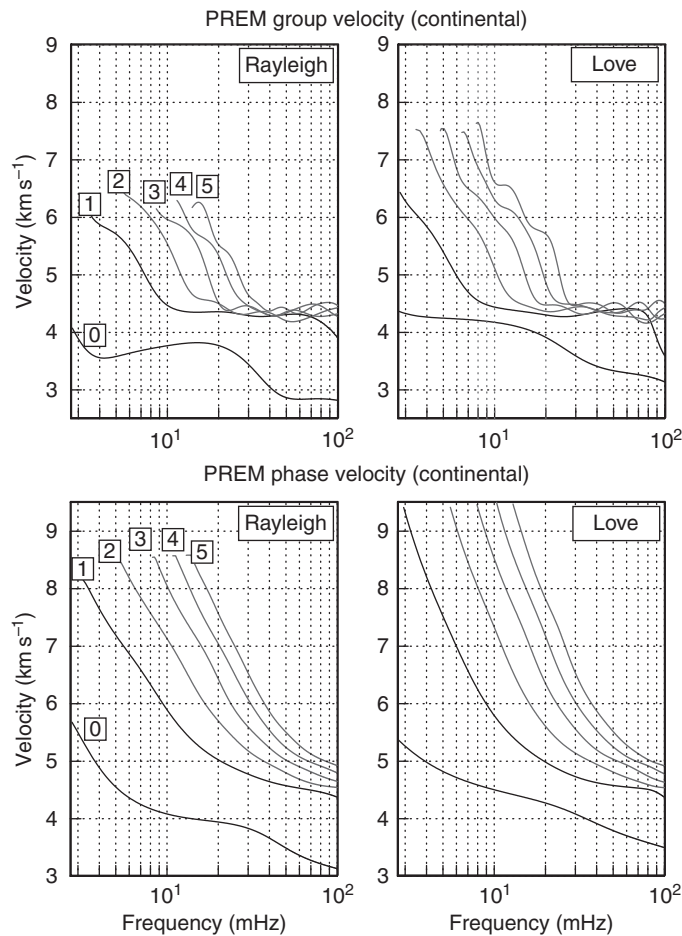


Figure 34 Group and phase velocity curves for isotropic PREM (Dziewonski and Anderson, 1981) with a 39 km thick continental crust. Shown are the fundamental modes (label 0) and the first five overtones (labels 1–5). Phase velocities span a greater range than group velocities. Overtones have nearly the same group velocities above 30 mHz (periods shorter than 33 s). For clarity of the diagrams, dispersion for IC modes and ScS equivalent modes at long periods are not shown.

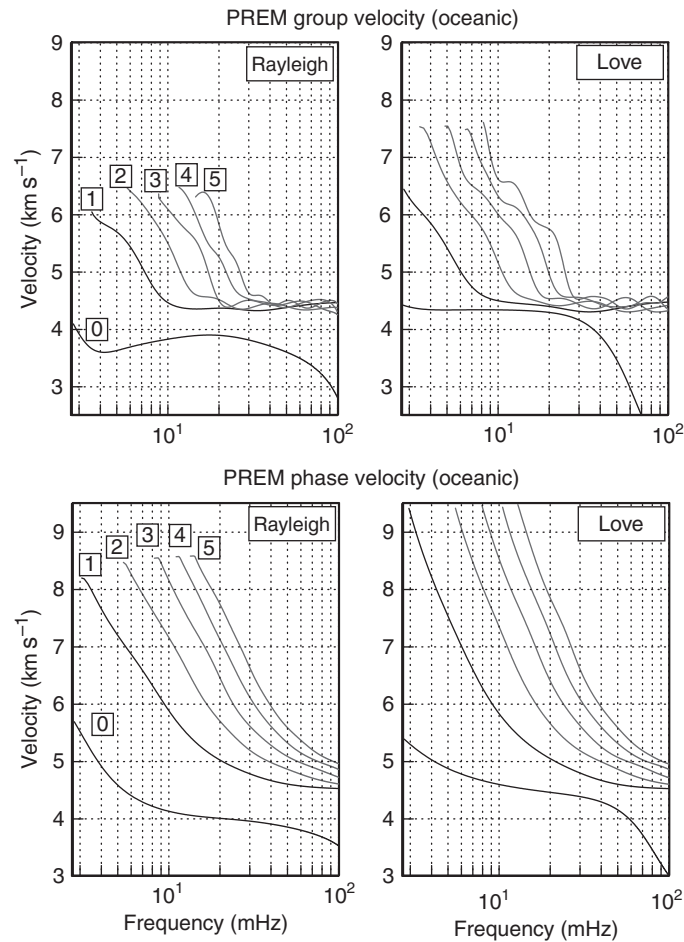


Figure 35 Group and phase velocity curves for isotropic PREM with a 7 km thick crystalline oceanic crust, overlain by 5 km of sediments (no water layer). Shown are the fundamental modes (label 0) and the first five overtones (labels 1–5). Phase velocities span a greater range than group velocities. Overtones have nearly the same group velocities above 30 mHz (periods shorter than 33 s). Love wave fundamental modes have similar group velocities as overtones between 10 and 20 mHz. For clarity of the diagrams, dispersion for IC modes and ScS equivalent modes at long periods is not shown.

dispersion. Probably one of the most well-known and subsequently most-cited summaries of early observed dispersion curves for both group and phase velocities is that of [Oliver \(1962\)](#) who published curves for both Love and Rayleigh wave fundamental modes and the first two overtones, for oceanic and continental paths. [Oliver \(1962\)](#) summarized results in a wide frequency range (corresponding to periods between 1 h and 1 s). At the time, overtone phase velocities remained largely unobserved. The summary was mainly based on the observations by Maurice Ewing and his group at LDEO, then the Lamont Geological Observatory, but the observation of Rayleigh wave dispersion goes back to at least the 1930s (e.g., [Carder, 1934](#), for oceanic paths; [Röhrbach, 1932](#); [Gutenberg and Richter, 1936](#), for continental paths). [Ewing and Press \(1954, 1956\)](#) collected long-period Rayleigh wave group velocities between 10 and 500 s. They observed a significant difference in dispersion for continental and oceanic paths at periods shorter than roughly 75 s and attributed dispersion at longer periods to be influenced primarily by structure in the mantle. Subsequently, surface waves at periods 75 s and longer were

called mantle waves, which is still used today (e.g., [Ekström et al., 1997](#)). Ewing and Press remarked that the dispersion of oceanic paths is strongly influenced by the presence of a water layer (e.g., [Ewing and Press, 1952](#), and also [Berckhemer, 1956](#)). It was observed that, due to the steep dispersion at periods shorter than 20 s, oceanic Rayleigh wave packets are far more stretched out than continental Rayleigh waves. The latter required long travel paths to resolve details in the dispersion curve. Short-period dispersion of the first ‘shear mode’ (overtone) was first observed by [Oliver and Ewing \(1958\)](#), for paths traversing the deep ocean after a nuclear explosion in 1955, about 700 km off the coast of Southern California (Operation Wigwam). The wave trains appeared unusually complicated but also gave seismologists a chance to observe oceanic dispersion for the first time at periods shorter than 15 s. Oceanic short-period overtone signals are usually hard to observe in teleseismic records due to the dominance of swell-generated microseism noise. The Wigwam records also revealed, for the first time, the slow Airy phase (waves with stationary group velocities; [Pekeris, 1946](#)) at around 7 s for oceanic paths.

Love wave dispersion is usually more difficult to measure than that of Rayleigh waves because the process involves the analysis of the typically noisier horizontal seismometer components. Also, long-period Love waves have similar group velocities over a wide frequency band, especially in the oceans (see Figure 35). This often makes Love waves to appear pulse-like, which hampered early dispersion measurements before the computer era. Nevertheless, Love wave dispersion measurements go back to at least the 1940s (e.g., Wilson, 1940). Figures 34 and 35 give a summary of the expected dispersion curves for fundamental mode Rayleigh and Love waves and their first five overtones. The curves are shown for isotropic PREM and both continental crust and oceanic crust. At frequencies above 10 mHz, variations in crustal structure have a significant effect on dispersion. Throughout a wide range in frequency, Rayleigh wave fundamental mode group velocity curves are fairly isolated from overtones, which allows easy dispersion measurement. This is not the case for overtones that overlap at frequencies above 15 mHz. Sophisticated ‘tuning’ techniques, such as array stacking, are then necessary to assess individual overtone dispersion (see Section 1.04.3.4). Also note that the first overtone branch overlaps with the Love wave fundamental mode branch between 10 and 30 mHz, for oceanic paths. Ignoring possible interference effects may lead to biased Love wave dispersion data, which is revisited in a later section.

For Rayleigh waves, we observe two Airy phases for which group velocity does not change much with frequency (Figures 34 and 35). One is near 4 mHz, and the other one is near

20 mHz. Between 4 and 20 mHz, the group velocity dispersion is inverse. The condition $du/dk < 0$ implies that modes with higher ℓ , hence higher frequency, are faster than modes with lower ℓ (compare also with Figure 33). This can be seen in the low-pass-filtered seismogram in Figure 2. Below 4 mHz and above 20 mHz, we observe regular dispersion with $du/dk > 0$ (low- ℓ modes are faster). This can be seen in Figure 36 that shows Rayleigh wave seismograms between 20 and 50 mHz in an oceanic setting. The figure also emphasizes that modern ocean bottom seismic instrumentation allows us to observe long-period surface waves on the ocean floor to an unprecedented signal level. Depending on crustal structure, a third Airy phase may be observed for Rayleigh waves near 50 mHz. For Love waves, group velocities are very similar over a large range in frequency. In oceanic settings in particular, the dispersion is very weak between 4 and 20 mHz, so that Love wave trains usually appear quite pulse-like.

The first attempts to take a general regionalization of surface wave dispersion beyond a distinction between continents and oceans go back to Toksöz and Anderson (1966) who decomposed composite-path great-circle data into those of ‘pure-path’ oceanic, shield, and mountain-tectonic regions. They analyzed records of the great Good Friday 1964 Alaska earthquake (28 March 1964) at stations Isabella, California (later station ISA of the TERRASCOPE Network), Kipapa, Hawaii (later station KIP of the IDA, GSN, and GEOSCOPE networks), and Stuttgart, Germany (later station STU of the GEOFON network). Kanamori (1970) analyzed many more records of this event ($M = 8.5$ as reported by Kanamori) and another great

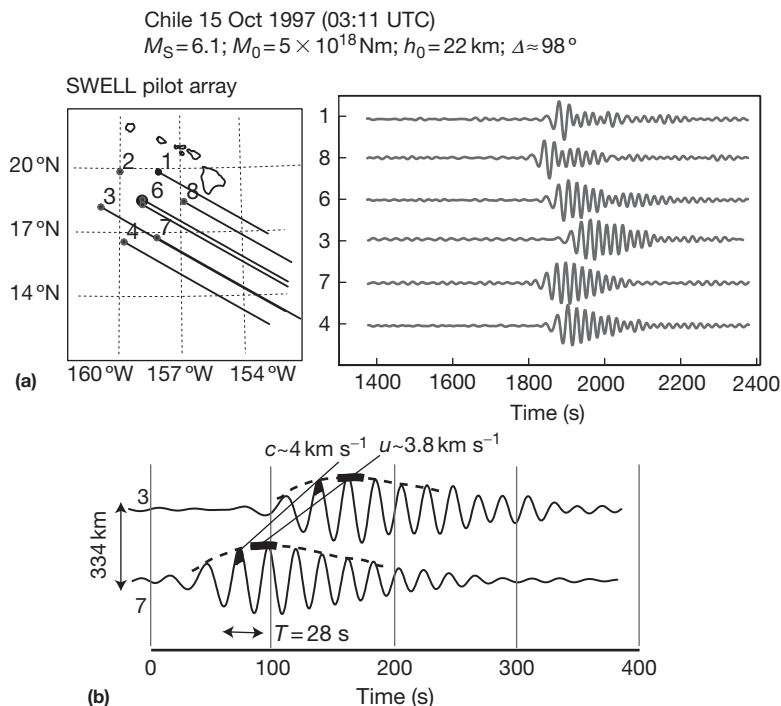


Figure 36 (a) Seismograms recorded on ocean bottom differential pressure sensors during the 97/98 SWELL Pilot Deployment southwest of Hawaii (Laske et al., 1998). The recorded frequencies range from 20 to 50 mHz. The waveforms exhibit regular dispersion, that is, low frequencies arrive earlier than higher frequencies. (b) Schematic concept of phase (c) and group (u) velocities along two-station leg 7-3.

earthquake in the Kuril Islands region (13 October 1963; $M=8.3$), and a supplement of earlier published data. Apart from phase and group velocity, he also measured great-circle attenuation but did not interpret the latter further. [Dziewonski \(1970\)](#) analyzed phase and group velocity for the 15 August 1963 Peru earthquake (the same earthquake that provided mode data for Earth model 1066A by [Gilbert and Dziewonski, 1975](#)) though phase velocities were derived from mode observations. This chapter also showed, for the first time, that world-circling measured phase and group velocities are mutually consistent. [Knopoff \(1972\)](#) first provided a more detailed discussion of surface wave dispersion in different tectonic regions.

Early measurements of surface wave dispersion were extended to frequencies much below 4 mHz. For example, the analysis of [Ewing and Press \(1956\)](#) extended to 2 mHz and that of [Toksöz and Anderson \(1966\)](#) extended even to 1.5 mHz. At such long periods, Coriolis coupling between Rayleigh and Love waves becomes considerable (see [Figure 13](#)) so that Love waves appear on the vertical seismometer component as so-called quasi-Love waves (e.g., [Levin and Park, 1998](#)). [Backus \(1962\)](#) discussed the effects of a rotating Earth on the propagation path of very long-period surface waves. While Love wave paths remain largely unaffected, Rayleigh wave great-circle paths precess about Earth's axis of rotation, effectively lengthening the travel path. Dispersion estimations that assume the direct great-circle path are then biased low. While early measurements were not precise enough for this effect to be significant, modern observations probably need to be corrected for this effect, which depends on Earth's 1-D structure much like the spheroidal-toroidal mode coupling does.

1.04.3.2.1 Group velocity

In the precomputer era, surface wave group velocity was measured using the peak-and-trough method (e.g., [Ewing and Press, 1954](#); [Ewing et al., 1957](#)). In a paper record, each peak, trough, and zero was numbered and plotted against recorded time. The slope of this curve gives the period as a function of travel time, from which the group velocity can be computed. This technique can be applied on well-dispersed signals but fails near Airy phases and for most Love waves because the waveforms are compressed. Even for the well-dispersed case, measurement errors are rarely better than 0.2 km s^{-1} , or about 6.5%. Since the late 1960s, when computers and the fast Fourier transform by [Cooley and Tukey \(1965\)](#) facilitated quick and comprehensive harmonic analyses, group velocity has been measured in the time-frequency domain. The most basic approach is the 'moving window analysis' ([Landisman et al., 1969](#)). A sliding window is applied to a time series, and the spectrum for each increment is tabulated in a time-frequency matrix, often called a Gabor matrix after Hungarian physicist Dennis Gabor ([Gabor, 1947](#)). Such a diagram is also called energy diagram (when amplitude squared is plotted) or, when the travel time is converted to velocity, a vespagram. [Figure 37](#) shows the Gabor matrix for the 1992 Flores Island region record at station SSB (see [Figure 2](#)). The group velocity is then determined by tracing the ridge with the highest amplitudes in the 2-D plot. This approach has seen wide use in a number of applications that deal with nonstationary signals and is still used today, for example, in the study of ocean swell-

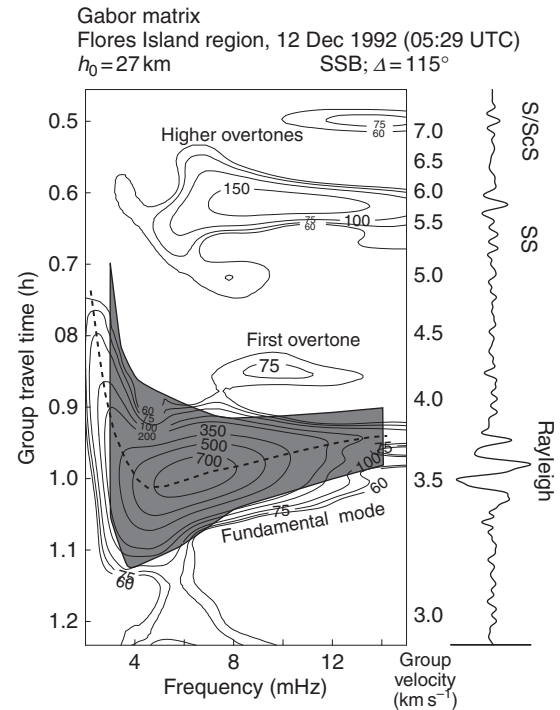


Figure 37 Visualization of a Gabor matrix for the seismogram in [Figure 2](#). Amplitudes in the matrix are normalized to optimize the display. The largest signal is the fundamental mode that exhibits dispersion (see [Figure 34](#)) where the dashed line marks the group velocity an analyst would choose. A combination of overtones arrives before the Rayleigh wave. The gray area marks the time-frequency range used in a time-variable filtering approach to isolate the fundamental mode.

generated signal in the microseism band (between 20 and 4 s) that is caused by approaching large storm systems (e.g., [Bromirski and Duennebier, 2002](#)).

When measuring dispersion, one has to be aware of the resolution limits in the Gabor matrix imposed by the Schwarz inequality ([Gabor, 1947](#)), where the smallest frequency separation, Δf , and the length of the sliding window, T , must satisfy $\Delta f \cdot T \geq 1$. For example, if the moving window is 1000 s long, the frequency resolution is not better than 1 mHz. To obtain the same relative resolution $\Delta f/f$ in the Gabor matrix, the sliding window can be made proportional to the period investigated, where the window length is usually four to eight times the period. Since this entails the separate calculation of a certain harmonic coefficient for each element in the Gabor matrix, this was sometimes prohibitively inefficient in the early days of computing. A quicker method is the multiple filtering technique (described in [Dziewonski et al., 1969](#)) that starts with the spectrum of a complete time series. A Gaussian filter is centered on a certain target frequency. The analytic signal, which provides the envelope function of the corresponding time series, is then determined for this frequency using the spectrum for positive frequencies only. Instead of just one element in the Gabor matrix, the envelope function now composes a whole column.

Measuring group velocity requires either interactive picking or a sophisticated routine that recognizes which ridge to pick. A widely used application in regional studies is the FTAN

(frequency–time analysis) package by Levshin et al. (1972) (see also Levshin et al., 1989). FTAN is similar to earlier multiple filtering methods except that FTAN uses an efficient folding algorithm to determine the complex time–frequency array from which the Gabor matrix is estimated. This allows the extraction of phase velocity as well. Signal enhancement in the Gabor matrix can also be achieved by the logarithmic stacking of several events in the group velocity–period domain (Shapiro et al., 1997). Modern techniques allow us to measure group velocity with an error that is usually much less than 0.1 km s^{-1} , or about 3.2%. The measurement of group velocity is advantageous over that of phase because many phase measurement applications require the knowledge of the source process (see eqn [19]). Group velocity observations are largely unaffected by source processes, which makes this approach very attractive in regional studies where earthquakes are typically small. For events deeper than about 25 km, the source may affect group travel times at long periods beyond 100 s though the bias is usually not significant, that is, smaller than the measurement error (Levshin et al., 1999).

Group velocities picked from the Gabor matrix can be biased, as first discussed by Dziewonski et al. (1972). As seen in Figure 30, the spectral amplitude for the first wave train increases with frequency. In this case, group velocity estimates from periodograms are biased toward high-frequency values. Changes in the spectral amplitude may be particularly large when dispersion is strong, which is the case for frequencies below 4 mHz. A similar bias occurs when phase velocities are estimated from the phase of the complex analysis of the Gabor matrix. Dziewonski et al. (1972) suggested to deconvolve the time series with a synthetic seismogram before measuring the much less pronounced ‘residual dispersion.’ There have also been developments to improve the multiple filtering technique itself. Wielandt and Schenk (1983) provided a formalism to correct the bias in phase velocity estimates to within 0.1%. A more recent reference is that of Shapiro and Singh (1999) who suggested to use a centroid frequency of the filtered spectrum rather than the center frequency of the Gaussian filter to tabulate the Gabor matrix.

1.04.3.2.2 The study of ambient noise

The determination of group velocity using ambient noise has become tremendously popular in recent years. Although many ambient noise studies are limited to the microseism band between 20 and 3 s, these studies may provide valuable dispersion data where inadequate earthquake distribution does not allow an analysis otherwise. Microseisms are generated by linear and nonlinear interaction of wind-generated ocean swell with itself and with the seafloor and the coast (see also Chapter 1.12). The most dominant microseism signal, at a period typically near 5 s, is generated when waves approaching from opposing directions interact nonlinearly to form standing waves in the water column (Longuet-Higgins, 1950). The resulting Rayleigh waves, which are excited continuously but incoherently, can be observed even in continental interiors. With the aid of a network, the dispersion of microseisms can be extracted to constrain local crustal structure (e.g., Sabra et al., 2005a; Shapiro et al., 2005). In essence, a cross correlation technique is applied to station pairs in an array to extract empirical Green’s functions (e.g., Sabra et al., 2005b; Shapiro and Campillo, 2004). Without

doubt, this technique has become so attractive because ocean noise is observed everywhere on the planet, and two-station Green’s functions are more readily extractable using noise than waves from single earthquakes that have to align with the two-station great circle. It appears that time series collected over just 1 month are capable of providing high-resolution images of Earth structure (Shapiro et al., 2005).

The study of ambient noise to extract Earth structure has also been applied to seismic stations on the ocean floor (e.g., Harmon et al., 2007). Even observations of phase velocity that inherently require more sophisticated measurement techniques than group velocity have appeared in the literature (e.g., Bensen et al., 2007; Harmon et al., 2007). Phase velocity results based on cross correlation are reported to be in good agreement with those obtained with beamforming (Harmon et al., 2008). The recent advances in ambient noise include the analysis of overtones (e.g., Harmon et al., 2007) and Love waves (e.g., Lin et al., 2008). In some areas, such as Europe, ambient noise group velocity constraints appear to be quite compatible with or even superior to those from earthquake data as the former appear to be more internally consistent (Yang et al., 2007).

In principle, the analysis of ambient noise can be extended to longer periods though noise levels are considerably lower than in the microseism band. At periods longer than 100 s, the interaction of infragravity waves with the ocean floor and the continental slopes is thought to generate infragravity noise (e.g., Tanimoto, 2005; Webb, 1998). Shapiro and Campillo (2004) found that broadband dispersion information can be extracted from two-station ambient noise cross correlation records, to periods up to at least 100 s.

A precondition for ambient noise analyses to yield unbiased dispersion data is that the source distribution is isotropic, that is, the microseisms have to approach the array from all directions, which may not always be the case. For example, Schulte-Pelkum et al. (2004) found preferential directions of approach at the ANZA Seismic network in Southern California. Strong source directivity was also found in Europe (Essen et al., 2003). Such source directivity is most obviously coupled to the seasonal return of large winter storms (e.g., Hiller et al., 2012) that may even be responsible for Earth’s hum (e.g., Kurrle and Widmer-Schmidrig, 2010; Rhie and Romanowicz, 2004, 2006). Uneven source distribution can result in phase velocity estimates that are biased high by up to 1%, which can map into seismic 3-D structure in tomographic images on the order of a few percent (Yang et al., 2008; Yao et al., 2006). For Southern California, Harmon et al. (2010) estimated the bias on isotropic phase velocity as a result of uneven source distribution to be +0.2% at a period of 25 s, at the same time mimicking an apparent azimuthal anisotropy of up to 1%. These effects can potentially be accounted for by performing a source density analysis. It seems that a year’s amount of ambient noise data that spans a time frame long enough to include effects from seasonal variations, coupled with robust cross correlation techniques, should deliver reliable results (e.g., Bensen et al., 2007). For further details about noise correlations, see Chapter 1.12.

1.04.3.2.3 Phase velocity

Unlike group travel times, the phase explicitly includes a source term (see eqn [19]). Measuring phase between a source and receiver therefore requires accurate knowledge of the

seismic source. The measurement of phase velocities without spectral analysis requires the comparison of at least two waveforms, for example, from seismograms of neighboring stations that share a great circle with the source (two-station method, e.g., [Brune and Dorman, 1963](#)). Using a one-station approach, [Nafe and Brune \(1960\)](#) first measured complete great-circle phase velocity for the 15 August 1960 Assam earthquake at station PAS (Pasadena, California) with errors $< 1\%$. Ten years later, the observation of phase velocity on a global scale was still in its infancy when [Kanamori \(1970\)](#) reported surface wave great-circle phase velocity observations for surface wave packets separated by a complete great-circle orbit, while others preferred to derive phase velocities from mode observations ([Dziewonski, 1970](#); [Dziewonski and Landisman, 1970](#)).

The phase of a surface wave packet changes very rapidly with frequency, and its 2π -ambiguity almost never allows us to measure phase between source and receiver directly from a single waveform. Early works suggested that in the two-station approach, phase estimated from a cross correlogram of the two seismograms yields more stable estimates than from phase differences ([Landisman et al., 1969](#)). Before we elaborate on our own measurement technique on the global scale, we briefly review advances in regional studies. For dense arrays where the station spacing is on the order of the signal wavelength, individual peaks or troughs can be followed across the array and phase velocities can be measured as function of period. Some of the earliest such measurements of phase velocity, for periods < 1 s, can be found in the oil exploration literature (e.g., [Dobrin et al., 1951](#)). For crustal or mantle studies, seismic arrays are typically sparse. [Press \(1956, 1957\)](#) used the triangulation or tripartite method to determine crustal structure in California from average phase velocities. But the use of the method goes back further (e.g., [Evernden, 1953, 1954](#)) and was also used to retrace hurricane tracks with seismic data (e.g., [Donn and Blaik, 1953](#)). In fact, the tripartite method was first used by Milne, and the interested reader is referred to [Evernden \(1953\)](#) for a brief review of early applications. In the studies of the 1950s, only few earthquakes were used for a particular station triangle, and measurement errors were on the order of 0.1 km s^{-1} (3%) or less. The technique assumes that plane waves approach a station triangle, whose aperture could reach several 100 km (e.g., [Knopoff et al., 1966](#)). These authors found that even though the method allows for an arbitrary arrival angle of the approaching wave, it yields biased results unless the wave propagation direction is aligned with one of the network legs. [Knopoff et al. \(1967\)](#) later found the two-station method to be superior to the tripartite method to minimize errors in phase shifts in the presence of lateral heterogeneity. [Schwab and Kausel \(1976a\)](#) suggested to expand the recording array to at least four stations and allow the consideration of curved wavefronts. In essence, in an optimization process, waveforms are matched to be in phase to form a single beam (beamforming). This is an approach that can still be found in the literature to determine the average structure beneath a recording array (e.g., [Alsina and Snieder, 1993](#); [Stange and Friederich, 1993](#)). The preposition here is that incoming wavefronts are uniform and distortion of the wavefronts within the array due to heterogeneous structure is insignificant though this may not be the case ([Wielandt, 1993](#)).

Numerous studies followed, and the two-station method is still used today to retrieve regional and local structure, often

along only one particular two-station path. A recent example of using the multiple filtering technique on a cross correlogram in the two-station case (between two real seismograms) is that of [Meier et al. \(2004\)](#) who studied Rayleigh wave phase velocity in the Eastern Mediterranean. It can be argued that phase velocities estimated with the two-station technique are systematically biased high when waves do not approach a station along the great circle, which is to be expected particularly in the analysis of teleseismic events. In our global studies, we have found that lateral refraction caused by heterogeneity in the mantle can change the direction of approach at a station by as much as 20° . The deviation of an arriving wave packet away from the great-circle direction effectively shortens the travel path. For a regional study that uses teleseismic earthquakes, the bias in the estimated phase velocity for a single travel path can therefore be as large as 6.4%. The bias on local or regional phase velocity can be reduced when many crossing paths are considered, but the estimates will remain biased high, unless the phase estimates are corrected for off-great-circle approach.

Another problem arises from multipathing when wave packets get refracted away from the great circle and then travel along multiple paths and interfere at the recording station upon arrival. Multipathing was detected in the early study of [Evernden \(1953\)](#) for surface waves traveling along the west coast of North America. Wavefronts get bent in complex structures and the plane wave approach is no longer valid. For example, waves get bent around an enclosed low-velocity anomaly so that the sides of a plane wave advance. In the extreme case, wavefront healing occurs when the wave travels long enough and ‘forgets’ that it passed this structure ([Wielandt, 1987](#)). To illustrate the gravity of the problem, one of the most remarkable examples of the controversy over the two-station method is probably that of [Woods et al. \(1991\)](#) along the Hawaiian Islands chain. They could not find a low-velocity anomaly associated with the proposed reheating of the Pacific plate by the Hawaiian hot spot and therefore argued against the plate reheating concept. On the other hand, [Maupin \(1992\)](#) argued that complex wave propagation along a relatively narrow low-velocity anomaly inhibits the application of the two-station approach for a single two-station path. [Pedersen \(2006\)](#) estimated that bias from ignoring the non-plane geometry of the incoming wavefield can be reduced to 1% in the two-station method for 200 km profiles, if at least ten earthquakes with different hypocenters are analyzed. This may be achieved for permanent station installations but is often difficult to achieve for temporary deployments that typically last less than 2 years. The unbiased recovery of structure within an array in the case of nonplane waves approaching the array requires the analysis of both phase and amplitude ([Friederich et al., 1994](#); [Wielandt, 1993](#)). [Friederich et al. \(2000\)](#) demonstrated that even though seismic surface waves propagating in a laterally heterogeneous half-space do not obey the Helmholtz equation, using the latter still gives much improved tomographic images over the usually applied eikonal equation. Of course, such an approach is only possible when data from dense arrays are available. [Forsyth and Li \(2005\)](#) proposed a simplified technique that fits two approaching plane waves to the observed phase measurements of an array. More recently, Mike Ritzwoller’s group applied Helmholtz tomography ([Lin and Ritzwoller, 2011](#)) to the data from

the dense USArray and produced high-resolution dispersion maps of the Western United States with stunning details (e.g., Lin et al., 2011).

For our global studies, we measure phase relative to a synthetic seismogram. In the simplest case, this can be a synthetic computed for a spherical Earth (e.g., Lasker and Masters, 1996). We measure the transfer function between the observed and a synthetic fundamental mode waveform that is calculated for Earth model 1066A (Gilbert and Dziewonski, 1975). An early example of the transfer function technique measuring great-circle dispersion and attenuation can be found in Dziewonski and Steim (1982). A multitaper approach provides an optimal compromise between frequency resolution and resistance to bias from noise in the time series. The multitaper approach also allows us to assign measurement errors in a statistical sense. The analysis is done interactively on the computer screen where we choose the optimal time window to isolate the fundamental mode. An example is shown in Figure 38. Other workers choose automated approaches (e.g., Trampert and Woodhouse, 1995). These approaches take significantly less time but may either produce a noisy data set or quality control restrictions yield a significantly reduced data set, compared to our hand-picked one. Measured phase perturbations typically amount to a few percent, and measurement errors are 0.15% on average for R_1 , while measurement errors in R_2 and great-circle data are somewhat smaller. Even though we measure phase with respect to a synthetic, some of our short-period data are 2π -phase-ambiguous. At short periods, the phase ambiguity is enhanced by the fact that small perturbations to a model may cause many 2π -phase wraps. The phase ambiguity can be removed by the condition that the phase has to vary smoothly with frequency. Since we observe no phase ambiguity at 4 mHz, our phase data set is unique, for the frequency range chosen in our global study (4–17 mHz). We usually need only one iteration to determine the transfer function, but occasionally, the great difference between data and synthetic requires one or two additional iterations (see Figure 38). Nevertheless, our ‘one-step’ spectral approach does not allow us to go much beyond 20 mHz. An alternative approach to obtain unbiased estimates in a wider frequency range is that of Ekström et al. (1997) who determined phase perturbation in several passbands rather than just one. As in our approach, they use synthetic seismograms in a phase-matched filtering procedure. The process is iterated to minimize residual dispersion and to suppress interference from overtones. They succeeded to collect an impressive global data set between 150 and 35 s. With 50 000 high-quality dispersion curves, their data set was the largest at the time, and their data and phase velocity maps have been used subsequently by many other workers either in their own global studies or to calibrate regional crustal models (e.g., Yang et al., 2004). An update of Ekström’s data set, phase and group velocity maps, and programs to evaluate the maps are described and provided in Ekström (2011).

1.04.3.2.4 Time-variable filtering

Time-variable filtering (TVF) was proposed to stabilize fundamental mode surface wave dispersion estimation when waveforms appear contaminated. Interference effects from other mode branches, multipathing, or other concurrent signals are the most likely causes. Arguably, one should probably refrain

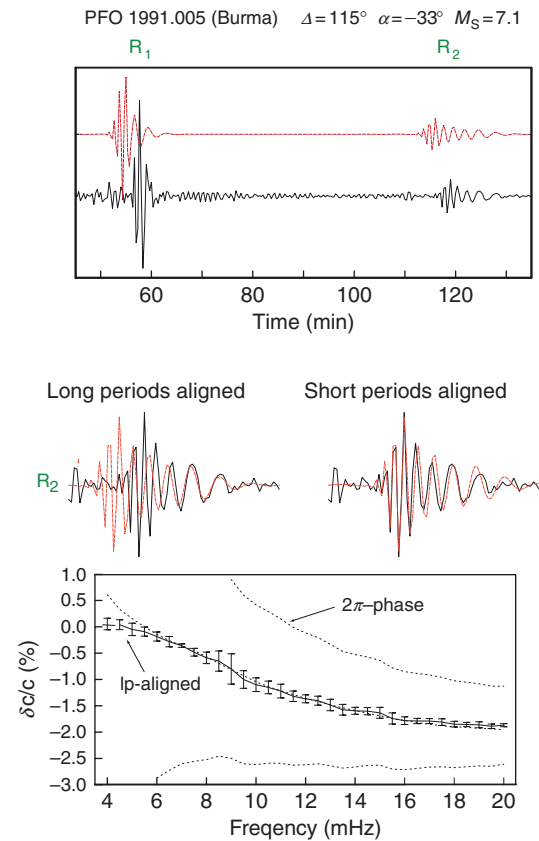


Figure 38 Example of our interactive phase measurement procedure in which the transfer function between an observed seismogram and a synthetic is retrieved. A seismogram at station PFO (Piñon Flat Observatory, California) is compared to a fundamental mode synthetic. The example is extreme in that the transfer function has to be determined iteratively, due to the large difference between observed and synthetic waveforms. The bottom panel shows the resulting path-averaged phase velocity perturbation. The dashed line in the middle marks the results when the waveforms are aligned on the short periods. Also shown are the results when 2π are subtracted or added to the phase (upper and lower dashed lines).

entirely from analyzing such contaminated waveforms. This may be feasible in global low-frequency seismology below 20 mHz, where large waveform collections are available. However, in regional studies using temporary networks, in monitoring efforts of the CTBT or to study the dispersion at shorter periods, this may not be possible. Aside from TVF, various techniques are available to extract a primary signal from a time series. Herrin and Goforth (1977) applied phase-matched filters (PMFs) to Rayleigh waves of an earthquake and a nuclear explosion. In this process, a time series is matched to a synthetic by iteratively windowing a narrow-band-filtered correlation function between the two to eliminate interfering signals. PMF makes no assumptions about the time–frequency structure of the interfering signals in a seismogram. TVF takes into account the dispersion. The idea behind TVF is that different signals may arrive at the recording station at the same time but the frequency content and group velocities are sufficiently different that the signal to be studied can be isolated by time–frequency filtering. For example, the Gabor matrix in

Figure 37 shows the fundamental mode as the largest signal, but at the same time as the very low-frequency fundamental mode reaches the station, the first overtone, with frequencies around 10 mHz, also comes in. A time–frequency filter that enhances the signal below 3 mHz at this time but then enhances 10-mHz signals at a later time significantly reduces the biasing effects of a single window covering the whole time series. [Pilant and Knopoff \(1964\)](#) first applied TVF to separate the seismic signal from two different earthquakes that arrived at a station nearly at the same time and therefore created a beating pattern in the waveform. Since then, the method has been applied to investigate structure of the crust and upper mantle (e.g., [Knopoff et al., 1966](#)). TVF is also included in the FTAN package of [Levshin et al. \(1989\)](#) in a second iteration to improve measurement precision. A technique that combines PMF with TVF is the frequency variable filtering of [Russell et al. \(1988\)](#) to reduce spectral amplitude biasing introduced by frequency domain filtering.

Technical details of the TVF approach are described in [Landisman et al. \(1969\)](#). The filtering can be done either in the time or the frequency domain. In the latter, the starting point is the spectrum of the original time series. Each harmonic coefficient is multiplied by a function that has a certain shape in the time domain. [Landisman et al. \(1969\)](#) suggested a cosine taper with

$$w(t) = \begin{cases} \cos\left(\frac{\pi(t-t_n(\omega))}{2L(\omega)}\right), & \text{for } t_n - L \leq t \leq t_n + L \\ 0 & \text{else} \end{cases}$$

where

$$L(\omega) = T(\alpha + \beta|du(T)/dT|)$$

$L(\omega)$ is the window length in the time domain, $T = 2\pi/\omega$, and $t_n(\omega)$ is the center group travel time. Other workers refined the filtering to optimize the trade-off between interference from unwanted signals and loss of energy for the signal analyzed (e.g., [Cara, 1973](#); [Roult, 1974](#)). At frequencies with strong dispersion, TVF should probably be applied with caution to avoid biased estimates, if $t_n(\omega)$ are the predictions of a model.

The technique has also found application in normal mode studies (e.g., [Jobert and Roult, 1976](#); [Roult and Romanowicz, 1984](#); [Roult et al., 1990](#)). Our own experience is that the technique works best for seismograms with epicentral distances far away from 90° ([Koptshalitsch, 1988](#)). For epicentral distances near 90° , the close temporal succession of overtones and fundamental modes does not allow an effective suppression of overtones without significantly affecting fundamental mode frequencies by several microhertz and Q by up to 20%. A topic of research still is why mean attenuation estimates for surface waves below 5 mHz often disagree significantly with those obtained from mode studies. [Durek and Ekström \(1996\)](#) suggested that noise contamination in the much longer normal mode seismograms can bias Q estimates high. [Roult and Clévéde \(2000\)](#) improved their time-lapse technique to obtain more accurate mode Q data that are in agreement with those of others though the discrepancy to surface wave Q remains. Our own unpublished experiments lead us to speculate that overtone interference may significantly bias mode Q estimate high, particularly for toroidal modes ([Masters and Laske, 1997](#)).

Some of this can be removed by TVF. On the other hand, some published surface wave-derived Q values may be biased low as our own surface wave results agree well with the mode Q values. Figures can be found on the REM web page. For a more detailed discussion, see also [Chapter 1.01](#).

1.04.3.3 Other Surface Wave Observables

Surface waves can be deflected significantly from the source–receiver great circle by lateral refraction in a heterogeneous medium. [Evernden \(1953, 1954\)](#) was among the first to observe this phenomenon at long periods. [Capon \(1970\)](#) observed off-great-circle propagation also at short periods (20–40 s) and found that refraction and reflection of wave packets at continental margins were responsible for this. Lateral refraction has also been observed by a large group of other workers and array techniques, such as the tripartite method of [Press \(1956\)](#) or comprehensive modifications thereof (e.g., [Stange and Friederich, 1993](#)), have been used to obtain unbiased dispersion estimates. In essence, incoming wavefronts are fitted simultaneously to the phase data of all stations in an array, where phase velocity and angle of approach are free parameters to search for. In regional studies that search for structure within an array, these arrival angles are discarded, but they can serve as additional constraint on structure along the travel path. [Woodhouse and Wong \(1986\)](#) developed the elegant linearized path integral approximation (PIA) to relate arrival angles to lateral heterogeneity. Similar to the integral in eqn [20], we can relate the tangent of the observed arrival angle, $v = \tan \theta$, to the phase velocity anomalies along the source–receiver great circle

$$v(\Delta) \simeq -\operatorname{cosec}(\Delta) \int_0^\Delta \sin \phi \frac{\partial}{\partial \theta} \left[\frac{\delta c(\pi/2, \phi)}{c_0} \right] d\phi \quad [23]$$

where the great circle has been rotated onto the equator, the source is at $\phi = 0$, the receiver is at distance Δ , and θ is the colatitude. A similar expression exists for the amplitude

$$\ln A \simeq \frac{1}{2} \operatorname{cosec}(\Delta) \int_0^\Delta \sin(\Delta - \phi) [\sin \phi \partial_\theta^2 - \cos \phi \partial_\phi] \times \left[\frac{\delta c(\pi/2, \phi)}{c_0} \right] d\phi \quad [24]$$

where ∂_θ and ∂_ϕ are derivatives with respect to θ and ϕ (e.g., [Romanowicz, 1987](#)). [Dahlen and Tromp \(1998\)](#) slightly modified this to include a term with sensitivity to phase velocity at the receiver. Both v and A depend on frequency because phase velocity does.

Both arrival angles and amplitudes depend on gradients of structure rather than structure itself, which gives them sensitivity to shorter wavelengths than the corresponding phase data (see also [Romanowicz, 1987](#)). [Wong \(1989\)](#) applied this theory to include amplitude data to obtain frequency-dependent phase velocity maps at very long periods (modes up to angular order $\ell = 59$ at about 6.5 mHz). We developed an interactive technique to measure arrival angles using the multitaper approach of [Park et al. \(1987a\)](#). In the most general case, this method models elliptical particle motion in 3-D space. In a singular value decomposition (SVD) of the three-component

seismogram, we seek the frequency-dependent complex eigenvector that spans the plane of particle motion. From the eigenvectors, we can derive polarization parameters, such as the eccentricity of the ellipse and three angles that define the orientation of the ellipse. The eigenvalues give us an idea of how well-defined the particle motion is, that is, how well it can be explained by a single ellipse. As in the case of phase data, the multitaper approach provides statistical error bars as well as resistance to bias from noise in the time series. Lerner-Lam and Park (1989) first used this technique to investigate lateral refraction and multipathing of long-period surface waves in the Western Pacific.

Other methods to analyze particle motion exist, for example, the method by Jurkevics (1988) that works in real space. In the interactive analysis of Plesinger et al. (1986), one seeks the local coordinate system for which certain component products are zero. These products, as functions of time, can be used to either discriminate between wave types or measure arrival angles. Paulssen et al. (1990) expanded the basic time-frequency analysis for the three-component seismograms and presented the time and frequency-dependent polarization of anomalous surface waves observed at stations on the Iberian Peninsula. They constructed a quality factor that depends on the largest eigenvalue of the SVD to assess the likeness of the signal to a Rayleigh or Love wave. Lilly and Park (1995) applied the time-frequency analysis using a wavelet algorithm and the multitaper technique to investigate the evolution of the frequency-dependent polarization in a time series. The methods described here all involve the analysis of single three-component seismograms. As discussed in the last section, assuming a simple incoming wavefield, arrival angles can also be determined from array analyses (e.g., beamforming). A recent example of this is the study of Cotte et al. (2000) who investigated off-great-circle propagation in southern France caused by lateral refraction of surface waves by the French Alps. Using the beamforming technique, Friedrich et al. (1998) and Essen et al. (2003) observed a strong directivity of ocean-generated microseism noise in Europe. Similar

observations exist for Southern California (e.g., Schulte-Pelkum et al., 2004).

Arrival angle data have been included successfully in inversions for global structure (e.g., Laske and Masters, 1996; Yoshizawa et al., 1999). It is interesting to compare the sensitivity of arrival angles and phase to lateral heterogeneity. Figure 39 shows the integral kernels of eqn [23] in a similar way as those for the phase integral in Figure 31. Sensitivity to short-wavelength structure increases with harmonic degree, which is the opposite of the behavior for the phase. This is due to the fact that arrival angles depend on the gradient of structure, not the structure itself as phase does (see eqn [20]). We also notice that sensitivity to high- l structure, relative to low- l structure, increases with travel distance and does not decrease as the sensitivity of phase does. Except for very short paths of $<20^\circ$, sensitivity to even harmonic degrees is always higher than to odd-harmonic degrees. Near the antipodes, sensitivity in the PIA becomes extremely large. At the same time, the antipode is a caustic with severe multipathing effects where asymptotic theories tend to break down (e.g., Romanowicz and Roullet, 1986). We therefore discard data for epicentral distances larger than 160° . Relatively speaking, arrival angle data also have larger measurement errors than phase data. In principle, sensitivity to short-wavelength structure can be enhanced by including large data sets of phase data for very short travel paths (i.e., $<30^\circ$) though the separation of the fundamental mode to obtain uncontaminated phase estimates at long periods becomes problematic. The collection of a global data set of arrival angle data, and its subsequent usage in the modeling of global structure, also has a useful by-product. Arrival angle data are sensitive to the misalignment of the horizontal seismometer components from east and north, and such information was not available when we first started our investigation. The joint inversion of arrival angles for structure and component misalignment can be linearized, but the inversion requires several iterations for misalignments of more than 5° . The Harvard group has also observed station misalignment though they use a different approach (Larson

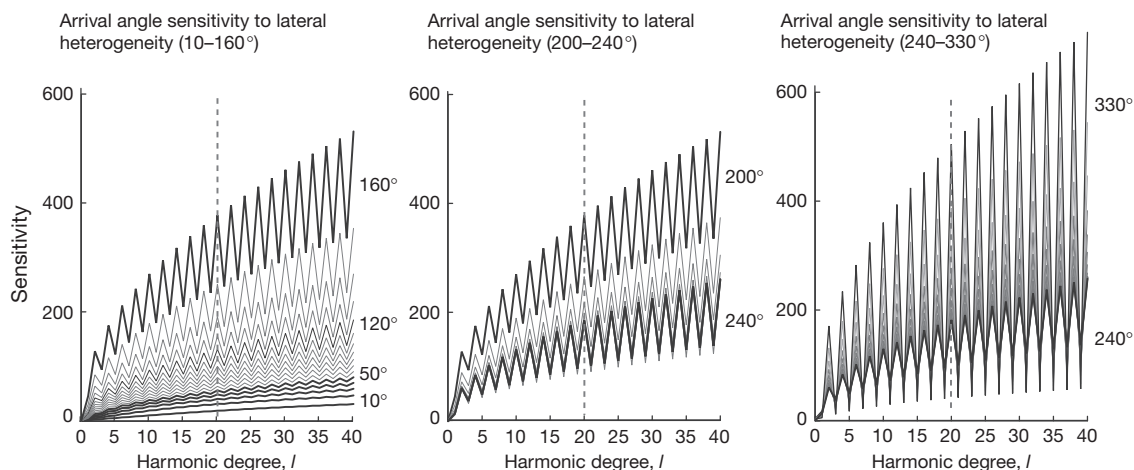


Figure 39 Arrival angle sensitivity to lateral heterogeneity, as function of harmonic degree in structure. Curves are shown for travel distances between 10° and 330° . Paths with distance $<180^\circ$ are for minor arc paths (R_1); larger distances are for major arc paths (R_2). We do not analyze data within 20° of the antipode so the kernels were omitted.

and Ekström, 2002): arrival angle information is extracted from smoothed amplitude estimates using a PMF technique and synthetic seismograms computed with the dispersion measured for each waveform. Their station misalignment data agree quite well with our own. Some of the misalignments that we published (Laske, 1995) have been confirmed by station operators, and this information is now routinely available at the DMCs, together with the instrument responses.

As mentioned in the preceding text, amplitude data are also very useful to constrain lateral heterogeneity. In fact, due to the second derivative in eqn [24], amplitudes are even more sensitive to short-wavelength structure than arrival angles are. Amplitude information has been used as additional constraints to investigate elastic structure. Some of the earliest work is that of Yomogida and Aki (1987) who used the Gaussian beam method to obtain 30–80 s Rayleigh wave phase velocity structure in the Pacific Ocean. Wong (1989) used their linear theory to include amplitudes in the retrieval of elastic structure at very long periods beyond 150 s. Dalton and Ekström (2006) showed that it is possible to retrieve elastic structure using surface wave amplitudes alone, but the primary purpose to study surface wave amplitudes has been to retrieve Earth's attenuation structure (e.g., Billien et al., 2000; Durek et al., 1993). The problem with analyzing surface wave amplitudes is that the effects of lateral elastic heterogeneity may be an order of magnitude larger than those of attenuation. Selby and Woodhouse (2000) found that amplitude variations are dominated by anelastic structure for long wavelengths and by elastic structure at short wavelengths. If the linear approximation of eqn [24] holds, then this would perhaps be expected because the amplitude great-circle integral over anelastic structure is linear and does not involve any gradient as that over elastic structure does. The first to successfully address this problem in the retrieval of anelastic structure was Romanowicz (1994) who took focusing–defocusing effects into account before constructing the first attenuation maps for long-period Rayleigh waves. More recent work to retrieve attenuation includes that of Gung and Romanowicz (2004) who provide a 3-D attenuation model for the upper mantle. Using the non-linear asymptotic coupling theory (NACT), they first derive an elastic model for V_{SH} and V_{SV} using long-period surface and body wave waveforms. The surface wave waveforms are then aligned using this model and inverted for 3-D attenuation. For further details about modeling attenuation from surface waves, see also Chapter 1.25.

Here, we have only discussed the horizontal arrival angles as observables to assess Earth structure, but the particle motion of surface waves is characterized by two additional angles: the sloping angle that describes the deviation of a Rayleigh wave orbit from the vertical and the tilting angle of the elliptical orbit with respect to the horizontal. Vig and Mitchell (1990) attempted to relate arrival angles (which they call inclination) and the sloping angles observed at station HON (Honolulu, Hawaii) of the DWSSN to the anisotropic mantle around Hawaii. The shape of the Rayleigh wave ellipse, that is, the ratio between major and minor axes of particle motion (HZ ratio), depends on the shallow structure. Tanimoto and Alvizuri (2006) had recently used the HZ ratio of microseisms to infer shallow crustal structure shallower than 5 km in Southern California.

1.04.3.4 Higher Modes

The analysis of overtones, or higher modes, is attractive because it yields independent constraints on structure at depth. Overtones are more sensitive to deep structure than fundamental modes of the same frequency (see Figure 43 in the next section). At long periods, overtones would significantly enhance resolution in the transition zone and uppermost lower mantle. At shorter periods, overtones carry better constraints on the low-velocity zone in the upper mantle than fundamental modes do. The analysis of overtones, however, faces several problems that are outlined in this section.

1.04.3.4.1 Higher-mode dispersion and waveform modeling

From Figures 34, 35, and 37, we have seen that the fundamental mode is fairly isolated in time and frequency because its group velocities are significantly lower than those of overtones. Overtone velocities, on the other hand, overlap significantly, except at low frequencies. Figure 37 suggests that we could analyze the first overtone, if we were able to isolate it, for example, using TVF or a phase-matched filtering operation (e.g., Jobert and Roullet, 1976). Note, however, that for this particular earthquake, the mode contains relatively little energy. For the other modes, extraction appears very uncertain. To illustrate the problem, Figure 40 shows the Gabor matrix for a synthetic calculated for isotropic PREM with a 39 km thick crust. For the seismogram in the top panel, all modes were included in the calculations, and we can discern the same body-wave phases, composed of interfering overtones, that we observe in the real seismogram. The other panels show the contribution from each mode, up to the fifth overtone. As just mentioned, the first overtone appears quite isolated in time–frequency space, but its energy is so little that it is not discernible in the composite Gabor matrix. The other overtones overlap significantly though extraction of the second higher mode may be possible at frequencies higher than 10 mHz, because group velocities are relatively low. At lower frequencies, there is significant overlap between the second and third overtones. At frequencies above 12 mHz, the third and fourth overtones overlap. TVF may provide only limited success in this case.

The first convincing observation of overtone dispersion was probably that of Oliver and Ewing (1957) for a path across eastern North America, but utilizing overtone dispersion to study Earth's interior obviously requires a different approach than fundamental modes do. The first breakthrough was achieved by Nolet (1975) and Cara (1978) who used an array stacking technique to separate different overtone branches using a ω – k transform, for studies of structure in Western Europe and across North America. This approach has also been used in other studies (e.g., Cara et al., 1981 for the Western United States). At fixed frequency, different overtone branches then appear separated in phase–group velocity space. This approach works well to obtain average structure within an array but does not allow us to assess variations within an array. The problem with this approach is also that it needs an array.

Using individual source–receiver data on a global scale, a successful separation of overtones up to order 8 was achieved by van Heijst and Woodhouse (1999). They used their mode branch stripping technique (van Heijst and Woodhouse, 1997)

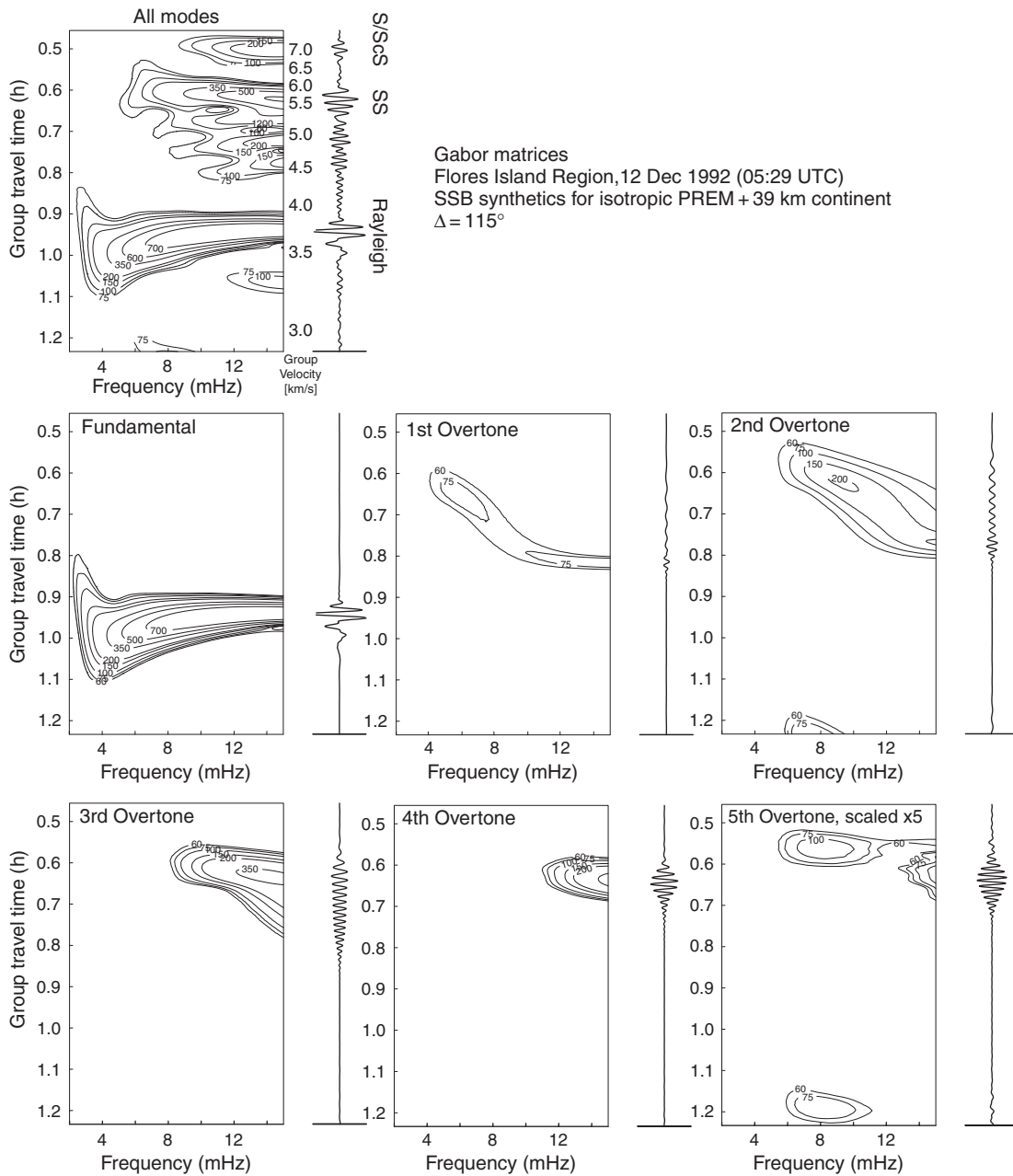


Figure 40 Visualization of a Gabor matrix for the synthetic seismogram in Figure 37. The top panel shows the complete synthetic, including all modes computed for isotropic PREM with a 39 km thick continental crust. The bottom panels show the Gabor matrices for the fundamental mode and first five overtones. While the fundamental mode is well isolated, the interference between overtones is rather complex. Note that the amplitudes for the fifth overtone are rather small. Also note that overtones beyond order 7 are required to compose the overlapping body-wave phases S and ScS (see also Figure 33).

to isolate the overtone branches and make global phase velocity maps (termed Oxford approach hereafter). This technique makes use of branch cross correlation functions (bccf's) that increase sensitivity to a certain overtone signal. The signal with the most energy is analyzed first and subtracted from the seismogram before successive branches are analyzed in a similar fashion. The technique works well for Rayleigh waves but appears to fail for Love waves due to strong interference effects.

This is one of few studies that extract dispersion. The vast majority of publications utilize waveform modeling to retrieve structure at depth directly, without involving the intermediate step of determining dispersion. One may argue about which approach is superior, but a useful by-product of the Oxford approach is the ability to check for consistencies in the data. For example, they were able to compare their fundamental mode Rayleigh wave maps at 40 s with that of the fourth

overtone at 62 s. Since their dependence on structure at depth is quite similar, the phase velocity maps should highly correlate.

The *bccf*'s have been used by others as well who choose the waveform modeling approach (e.g., [Cara and L  v  que, 1987](#); [Debayle and L  v  que, 1997](#)). Other advances to study overtone branches include the hybrid technique by [Stutzmann and Montagner \(1993\)](#). This waveform fitting technique retrieves path-averaged overtone phase velocities and path-averaged velocity structure in successive steps. An attempt to determine global structure was discussed by [Stutzmann and Montagner \(1994\)](#) though data coverage was quite sparse. Similar to Nolet's array technique, they utilized several earthquakes along similar paths to retrieve phase velocities. They recently developed the 'roller-coaster technique' ([Beucler et al., 2003](#)) that is named after the shape of the misfit function in their method. Their method can be applied to a cluster of events to retrieve structure along a single source-receiver great circle in a nonlinear scheme. Another development is that of [Yoshizawa and Kennett \(2002, 2004\)](#) who used [Sambridge's \(1999\)](#) neighborhood algorithm to efficiently search the model space for multimode dispersion in a nonlinear waveform inversion.

Most of the other techniques involve full waveform modeling and the retrieval of structure at depth directly, without determining dispersion first. The first study on a global scale was that of [Woodhouse and Dziewonski \(1984\)](#) whose global upper-mantle shear velocity models, M84A and M84C, were regarded as reference 3-D model upper-mantle models for the following decade. The technique is still used by the Harvard group and has led to a series of updated whole mantle models such as S12/WM13 ([Su et al., 1994](#)) and S362D1 ([Gu and Dziewonski, 1999](#)). Though Woodhouse and Dziewonski used normal mode summation to calculate synthetic seismograms, they used a clever trick to account for sensitivity to odd-degree structure by introducing a fictitious epicentral distance shift in the minor and major arc great-circle integrals. This was later justified theoretically by [Mochizuki \(1986a,b\)](#) and [Romanowicz \(1987\)](#). Woodhouse and Dziewonski argued that individual waveforms are probably too noisy for direct inversions for structure so they projected their measurements onto a set of global basis functions in a two-step procedure. Another global waveform modeling approach is that of the Berkeley group called NACT ([Li and Romanowicz, 1995](#)). This technique accounts for cross branch coupling that is ignored in conventional path average approximations. While this is less of an issue for fundamental modes surface waves, it becomes relevant for overtones that involve deep-turning body waves. The application of this technique led to the first 'Berkeley model,' SAW12D ([Li and Romanowicz, 1996](#)), as well as more recent models (e.g., SAW24B16 by [M  gnin and Romanowicz, 2000](#)). In contrast to other mantle models, the Berkeley models have traditionally been V_{SH} models. A recent discussion of asymptotic and nonasymptotic waveform modeling approaches can be found in [Cl  v  d   et al. \(2000\)](#).

With his nonlinear partitioned waveform inversion, [Nolet \(1990\)](#) provided a tool that is widely used in regional-scale studies. The technique is similar to step 1 in the Woodhouse and Dziewonski approach. Publications are too numerous to list here, but examples include work in Western Europe (e.g., [Zielhuis and Nolet, 1994](#)), in North America (e.g., [van der Lee](#)

and [Nolet, 1997](#)), and on the Skippy array in Australia (e.g., [Simons et al., 2002](#)). Nolet argued that full waveform inversions directly for 3-D structure are computationally expensive and do not allow for a proper assessment of resolution capabilities. Rather, one can 'partition' the process and search for multiparameter, path-averaged structure first, for each source-receiver path, before conducting a computationally efficient inversion of a sparse matrix to retrieve 3-D structure. An advancement of this technique is its automation by [Lebedev et al. \(2005\)](#), which allows the processing of large data sets such as massive global data sets or regional-scale data sets from a dense network such as the USArray.

A few concluding words of caution are in order. We have seen that overtones have the potential to constrain deep Earth structure much better than fundamental modes do, and numerous studies emphasize that resolution is 'significantly' enhanced over fundamental mode only studies. A reader has to bear in mind though that in the parametric approach, due to the massive interference with other overtone branches, errors in the fit to overtone data are probably much larger than to fundamental mode data. Another important point is the relative weight of overtone data in an inversion. We have seen in [Figure 37](#) that recorded amplitudes of overtones were much smaller than those of the fundamental mode. Overtone experts may argue that the choice of the seismogram to demonstrate this point is poor because this earthquake was shallow. Such earthquakes excite fundamental modes particularly well and usually leave overtones with much reduced amplitudes in the seismogram. A proper choice of earthquakes for overtone studies therefore focuses on deep events. Unfortunately, such events are relatively rare and even more unevenly distributed than shallow events. [Figure 41](#) shows that earthquakes with source depths >75 km account for only 21% of all earthquakes, while the rest are shallower. Even with source depths of about 150 km, the fundamental modes still dominate the seismogram. Only when source depths become significantly

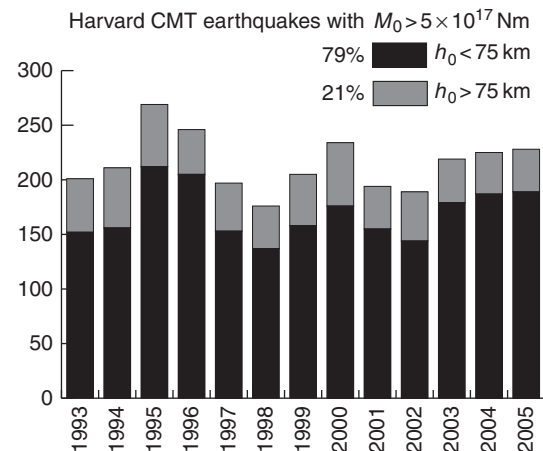


Figure 41 Events from the Harvard CMT catalog, for each year between 1993. Shown are all events with scalar seismic moment $M_0 \geq 5 \times 10^{17}$ Nm. For shallow events, this corresponds approximately to $M_S \geq 5.4$. Shown are 'shallow' events with source depths <75 km, which comprise 79% of all earthquakes. Events deeper than 75 km, which are potentially better earthquakes to study overtones, account for only 21% of all earthquakes.

greater than that, overtones above 4 mHz have larger spectral amplitudes than fundamental modes, which implies further reduction in the number of suitable earthquakes. A careful assessment of the resolution capabilities of a certain data set therefore entails more than just comparing the sensitivity kernels of fundamental modes and overtones. A 3-D surface wave tomographer essentially faces a trade-off problem. One can use all earthquakes to obtain best lateral resolution but bearing in mind that the vertical resolution is dominated by the limitations that fundamental modes dictate. Or one can choose mostly deep events to obtain optimal depth resolution, at the expense of decreased lateral resolution dictated by the sparser source distribution. The Berkeley and Oxford approaches appear to account for this by giving different weights to overtones, but the issue appears somewhat unresolved.

1.04.3.4.2 Love waves and overtones

With increasing amounts of data and the sophistication of measurement techniques, measurement errors have become ever smaller. Systematic biases introduced by unmodeled effects then become significant. We have already pointed out in [Figures 34 and 35](#) that Love wave overtone group velocity curves are quite close to that of the fundamental mode between 8 and 12 mHz (125–85 s). In a seismogram, short-period Love wave overtones therefore appear at the same times as long-period fundamental modes. Using sophisticated time-frequency analyses, such as the multiple filtering technique, one may be able to separate the different mode branches. However, it appears that even advanced techniques such as the branch stripping technique are not able to properly separate Love wave overtone branches, possibly because cross branch coupling is significant ([Méglin and Romanowicz, 1999](#)). The question now is whether even the fundamental modes can be analyzed without taking interference effects into account. For oceanic paths in particular, overtones and fundamental mode group velocities are nearly the same for similar frequencies and separation is no longer trivial. It was discovered early that Rayleigh and Love waves are often incompatible, that is, that no realistic isotropic model fits the dispersion of both wave types simultaneously (e.g., [McEvelly, 1964](#)). Often, such models exhibit low-velocity zones overlain by thin lids with nearly unrealistically high shear velocities.

Some argued that at least some of this discrepancy can be explained by Love wave overtone contamination (e.g., [Thatcher and Brune, 1969](#)). Others suggested that no uniform bias can be found in a large data set that includes several earthquakes, for a given path and model (e.g., [Boore, 1969](#)). Due to this unsatisfying problem, initial collections of regionalized models resulting from inversions of dispersion curves did not include Love waves ([Knopoff, 1972](#)). The vast majority of publications address this problem by allowing transverse isotropy in the model, also called polarization anisotropy or radial anisotropy. More recently, [Polet and Kanamori \(1997\)](#) revisited this problem by studying the biasing effects for an upper-mantle model in Southern California. They found that after correcting for the biasing effect on Love waves from overtone contamination, the models obtained from Love and from Rayleigh waves were much more compatible than before.

They also found that after the correction, the isotropic model that fit both wave types was much more realistic than before though the model had an unusually fast thin lid beneath the Moho and a low-velocity zone near 100 km depth, both not obtained when inverting for each wave type alone. On the other hand, [Ekström and Dziewonski \(1998\)](#) argued that anomalies found in V_{SV} , deduced from uncontaminated Rayleigh waves, and not in V_{SH} led to their discovery of anomalous azimuthal anisotropy in the Pacific ocean, while V_{SH} basically follows the lithospheric age progression.

With two-thirds of Earth covered by oceans, a possible contamination of Love wave data by overtones would pose a serious problem to find a proper REM. Our REM website compares the spherical averages of various published Love wave phase velocity maps with toroidal fundamental mode frequencies. Mode frequencies should not be biased by overtone contamination because an entirely different measurement technique is applied. A discrepancy between Love waves and toroidal modes is not apparent, which could indicate that, at least on average, overtone interference does not affect global estimates of Love wave phase velocity. A Rayleigh–Love incompatibility therefore can only be due to transverse isotropy. Nevertheless, a test with synthetic seismograms could help to illuminate how large a possible bias could be. We calculated 1200 mode synthetic seismograms for model 1066A that included the complete set of overtones. Using the same technique that we used in [Laske and Masters \(1996\)](#), we then measured phase relative to 1066A fundamental mode synthetics. [Figure 42](#) shows the median of our measured phase velocity anomalies. Rayleigh waves are essentially not affected by overtone contamination. Love wave data, on the other hand, show a bias that becomes significant at higher frequencies and can reach 0.06%, a result that could potentially raise concern. However, when comparing these discrepancies with the medians in the real data, we find that this bias is an order of magnitude smaller than what we observe. Potentially, Rayleigh wave overtone contamination could play a role if significant lateral refraction rotates some of the signal from the radial onto the transverse component. We have not tested how much this affects our data set, but we suspect that this effect is much smaller than Love wave overtone contamination. It appears therefore that a possible Rayleigh–Love incompatibility requires a transversely isotropic REM. Note that the medians shown here are averages in the data set and not true spherical averages, which are obtained only after an inversion for phase velocity maps. The small changes this would entail are irrelevant and do not at all affect the discussion here.

1.04.3.5 Surface Waves and Structure at Depth

The first inversion of surface wave dispersion to obtain mantle structure was carried out for the Canadian Shield by [Brune and Dorman \(1963\)](#) along a two-station pair. Forward modeling attempts go back at least 10 years (e.g., [Ewing and Press, 1954](#)). A vast amount of modeling attempts has followed since then, and the interested reader finds a detailed description of the quest for structure in the mantle in other contributions in this volume, for example, [Chapter 1.16](#), which also discusses azimuthal anisotropy, or that of [Chapter 1.21](#), which discusses

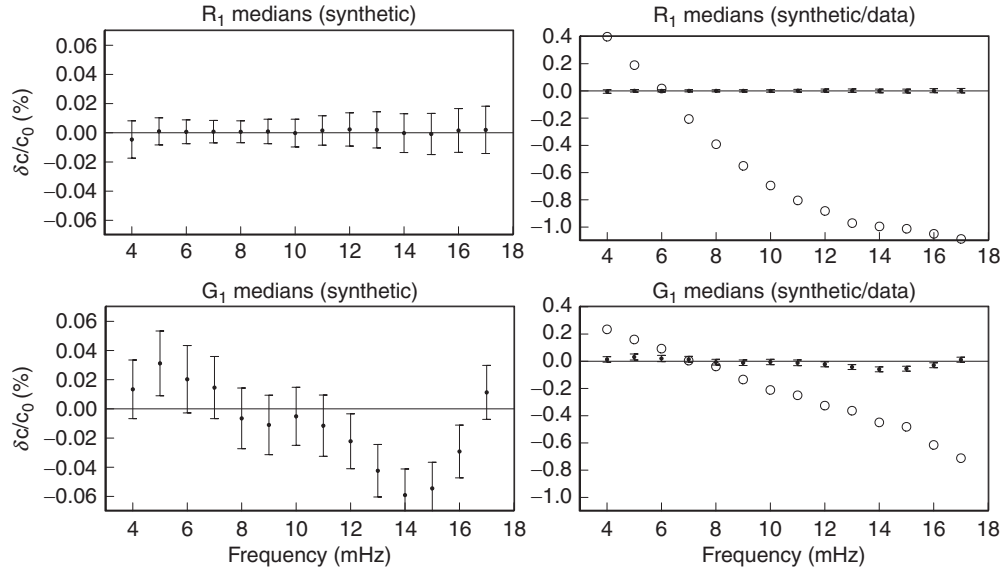


Figure 42 Estimation of the bias on fundamental mode phase velocity estimates introduced by overtone interference. Measurements are with respect to fundamental mode synthetics computed for model 1066A of Gilbert and Dziewonski (1975). The left panels show the bias on about 1200 synthetic waveforms that include the complete set of overtones, for Rayleigh (R_1) and Love (G_1) waves. The right panels show the same synthetic results but now together with the anomalies that we measured in our Laske and Masters (1996) data set (open circles). The synthetic test shows that the bias on Love waves is much greater than on Rayleigh waves, and the bias is significant. On the other hand, the anomalies that we measure on real data are an order of magnitude larger.

attenuation. A comprehensive review on the inversion of surface waves can be found in Romanowicz (2002). Here, we would like to close the discussion on surface wave data and their inversion for structure at depth with just a few remarks. Surface wave phase velocity is sensitive to all three elastic parameters, V_S (or β), V_P (or α), and density ρ :

$$\frac{\delta c}{c} = \int_0^a r^2 dr (\tilde{A} \cdot \delta\alpha + \tilde{B} \cdot \delta\beta + \tilde{R} \cdot \delta\rho) \quad [25]$$

where a is Earth's radius, r is the radius and all other parameters in the integral depend on r . In addition, phase velocity and the integral kernels depend on frequency. For uncoupled modes in transversely isotropic media, phase velocity sensitivity is expressed in terms of even more parameters where the two velocities are replaced by the five elastic parameters A , C , N , L , and F (e.g., Dziewonski and Anderson, 1981; Love, 1927; Takeuchi and Saito, 1972) where

$$\begin{aligned} V_{PH} &= \sqrt{A/\rho}, & V_{SH} &= \sqrt{N/\rho} \\ V_{PV} &= \sqrt{C/\rho}, & V_{SV} &= \sqrt{L/\rho} \\ \eta &= F/(A - 2L) \end{aligned}$$

where $A = C$, $N = L$, and $\eta = 1$ for isotropic media. Note that A here is not to be confused with the integral kernels \tilde{A} -tilde in eqn [25]. Montagner and Nataf (1986) devised an elegant technique to generalize this representation to model azimuthal anisotropy in the so-called vectorial tomography (Montagner and Nataf, 1988). In transversely isotropic media, Rayleigh waves are sensitive to all four velocities: V_{PV} , V_{PH} , V_{SV} , and V_{SH} where sensitivity to the latter is practically negligible. On the other hand, Love waves are sensitive to V_{SH} and V_{SV} where sensitivity to the latter is significantly smaller and usually ignored. We have no space to discuss the effects of anisotropy

in greater detail, but the interested reader is referred to Chapter 1.16.

As mentioned in the preceding text, investigators strive to include overtones in their modeling because overtones enhance sensitivity to structure at greater depth than fundamental modes do. Figures 43 and 44 show the sensitivity of Rayleigh and Love wave fundamental modes and their first two overtones to isotropic structure at depth. In the frequency range considered here (4–20 mHz), fundamental modes do not reach much beyond 300 km, though some sensitivity exists down to 500 km for 4 mHz Rayleigh waves. Overtones, on the other hand, reach well into the lower mantle. This fact has been utilized by numerous surface wave studies that concentrate on the transition zone and subducting slabs (e.g., Stutzmann and Montagner, 1994; Trampert and van Heijst, 2002; van der Lee and Nolet, 1997). In the isotropic case, Rayleigh waves are not very sensitive to V_P deeper than 50 km, but sensitivity is significant at shallower depths where sensitivity to V_S is very low. A comprehensive inversion for structure at depth would include the search for all three elastic parameters. In practice, this is usually not feasible, because the frequency range covered by the measurements does not provide enough independent information to make an inversion well constrained. To simplify an inversion, scaling relationships between the kernels for V_S , V_P , and ρ are drawn from mineral physics constraints and used to include the kernels for V_P and ρ in the kernels for V_S . We then invert only for V_S . For mantle structure, we commonly use, for all depths,

$$\begin{aligned} \tilde{A} \cdot \delta\alpha &= (1/1.7)\tilde{B} \cdot \delta\beta \\ \tilde{R} \cdot \delta\rho &= (1/2.5)\tilde{B} \cdot \delta\beta \end{aligned}$$

This assumption is basically valid if observed seismic anomalies are caused by thermal effects. In the crust, above 50 km

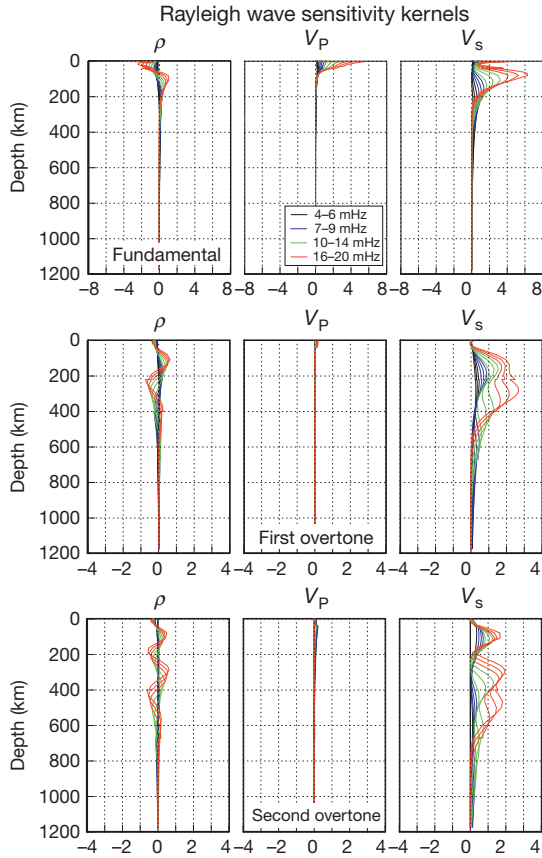


Figure 43 Sensitivity kernels for phase velocity to isotropic structure at depth, for Rayleigh wave fundamental modes and the first two overtones. Rayleigh waves depend on all three parameters, but sensitivity to V_S dominates. Overtone sensitivity to V_P is weak, and fundamental modes are affected only by V_P shallower than 50 km, when sensitivity to V_S decreases. Overtone sensitivity to structure below about 300 km is larger than that of fundamental modes though note that the scale is different by a factor 2. The model used to calculate the kernels is PREM.

depth, compositional variations may dominate and the scaling relationships no longer hold (e.g., in thick sedimentary basins). It is somewhat fortunate that sensitivity to shallow V_S is greatly diminished. Consequently, if we invert for a model, the shallow structure should probably be attributed to variations in V_P , not V_S as is commonly done. Note, however, that sensitivity to shallow density is also significant and a detailed discussion of tectonic implications should take this into account. A point that has not been treated here is that group velocities provide additional independent constraints, not in the physical sense but from a measurement technique point of view. A combination of the two is particularly useful to reduce ambiguities resulting from data uncertainties and to enhance the modeling of crustal structure (e.g., Shapiro and Ritzwoller, 2002).

We should mention that all examples shown in this chapter use a spherical Earth approach. On regional scale, when travel paths are limited to a few 100 km, investigators may choose to use a flat Earth approach. Surface wave applications overlap sufficiently that data or models may be compared that did not use the same approach. In this case, an Earth-flattening

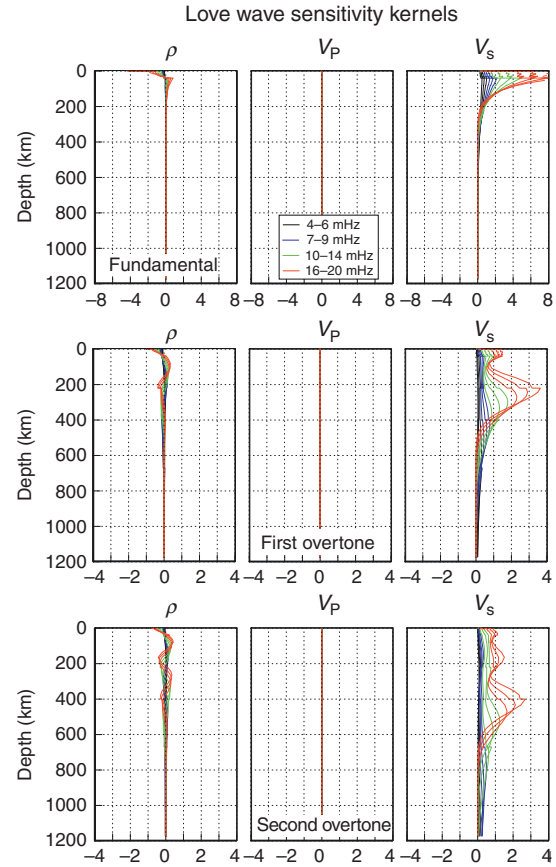


Figure 44 Sensitivity kernels for phase velocity to isotropic structure at depth, for Love wave fundamental modes and the first two overtones. Love wave fundamental modes are primarily sensitive to V_S only, but some sensitivity for density exists, especially for overtones. For details, see Figure 43. Second overtones are particularly useful to constrain structure in the transition zone.

transformation has to be applied to facilitate this comparison (e.g., Ben-Menahem and Singh, 1981; Biswas and Knopoff, 1970). In the case of a velocity model comparison, a conversion can be done through

$$v_f(z_f) = \left(\frac{a}{r}\right) v_s(r) \quad [26]$$

where the subscripts f and s denote ‘flat’ and ‘spherical,’ z is the depth, r is the radius, and a is Earth’s radius (Shearer, 1999). Near the surface, the differences between v_f and v_s are insignificant, but they become larger with depth. To use Shearer’s example, with $v_s = 8.6 \text{ km s}^{-1}$ at 150 km depth, the velocity in the flat Earth model would be 2.4% larger and the impact on velocity becomes relevant when discussing geodynamical implications.

A major issue not covered in this chapter is the model parameterization and the regularization during an inversion. Both influence the outcome of the modeling effort. The two basic classes of parameterizations include ‘global’ and ‘local’ ones. In a ‘global’ parameterization, each contributor to a set of basis functions covers the entire model space but represents different wavelengths (e.g., Chebyshev polynomials or spherical harmonics). In a ‘local’ parameterization, each contributor

covers only part of the model (e.g., layers or local B-splines). Comprehensive techniques also search for perturbations in boundaries, not only perturbations in elastic parameters. Regularizations or damping tries to account for the fact that some parts of the model space remain poorly constrained by the available data. For example, Rayleigh waves at periods shorter than 50 s have only marginal sensitivity to structure below 150 km. An undamped inversion could falsely place structure at these depths after a least-squares procedure dictated that this is the minimum norm solution. From a data perspective, this solution is not justifiable because there were no data to reliably constrain this. A careful analyst therefore conducts thorough a posteriori hypothesis testing (e.g., spike, checker board, or other tests with hypothetical input structures) on which structures of the model are reliably imaged and which are likely not. Other issues include how the inversion is done. Depending on the inversion algorithm, the modeling can end up in a local minimum of the misfit function in which case the model does not represent the best model consistent with our data. The Monte Carlo technique is used in forward modeling to explore larger areas in the model space (e.g., Shapiro and Ritzwoller, 2002). To make the search computationally more economical, Knopoff (1972) employed a hedgehog algorithm that he and Keilis-Borok developed (see also Keilis-Borok and Yanovskaja, 1967). The search starts out in a Monte Carlo fashion but then refines it once a minimum is found. Neighboring model parameters are tried out but discarded if the predictions move the value in the misfit function outside of a certain boundary around the minimum. Beghein and Trampert (2004) provided a novel approach using the neighborhood algorithm of Sambridge (1999). They define probability density functions to explore the range of possible models. Such forward approaches are attractive, but one should carefully evaluate the coverage of the null space. Last but not least, the Backus and Gilbert (1968) approach is still used today (Masters and Gubbins, 2003) when specific targets are investigated. In the B&G approach, specific linear combinations of data are selected that illuminate a certain model parameter (e.g., density near the core–mantle boundary). This method is attractive in that it provides an elegant way to assess the resolution capabilities of the data.

1.04.3.6 The Validity of the Great-Circle Approximation and Data Accuracy

Much of the discussion presented here is based on the use of Fermat's principle. Anomalies are assumed to accumulate along the great-circle arc between the source and receiver. Concerns about the validity of the great-circle approximation and suggestions to improve the interpretation of observables may go back as far as the great-circle approximation itself, and we need to be aware to which limit approximate theories are applicable. For example, Woodhouse and Ginius (1982) presented surface kernels for normal modes that show a rather broad corridor of sensitivity to structure along the source–receiver great circle. On the other hand, Jordan (1978) made a good argument that, asymptotically, modes are essentially sensitive to structure in the immediate vicinity of the source–receiver great circle. This is true if structure is smooth and the structural wavelength remains much larger than the signal

wavelength. This applies not only to normal modes but also to surface waves. Advances in parametric surface wave modeling have been made through Gaussian beam ray-tracing techniques (e.g., Yomogida, 1985), Born single and multiple scattering (e.g., Friederich et al., 1993; Snieder and Nolet, 1987), or diffraction tomography (e.g., Meier et al., 1997; Ritzwoller et al., 2002). More recently, finite-frequency theory (e.g., Yoshizawa and Kennett, 2005; Zhou et al., 2005) has been added to the tools in the quest to resolve ever smaller details in Earth structure using surface waves. While each of these techniques promises vast improvement over simple approximations, they almost always also have their own limitations. Equally if not more importantly, we must not forget that the resulting models can only be as good as the data that the modeling is based on (see, e.g., Trampert and Spetzler, 2006). Measurement uncertainties can be large due to noise in the time series that may often be accepted too readily as being Gaussian because the theory requires it. Often, noise is produced systematically, for example, through coupling or interference effects or by inappropriate measurement techniques or by not accounting for them properly. Noise may simply be introduced by unknown effects such as a failing instrument, a faulty installation, or unknown coupling of the instrument to the ground. It is probably not unheard of that a spurious resonance in an installation (e.g., a process turning on every few minutes) nearly coincides with a normal mode frequency of Earth and the data analyst was not aware of the problem. We hope that this chapter has contributed to raise awareness of how important it is to understand how data are collected and how one's favorite measurement technique works and to judge its strengths and pitfalls objectively. Only then is one able to discuss the validity of small details in a model.

1.04.4 Concluding Remarks

As mentioned in Section 1.04.1, the seismograms we analyze are typically collected within the FDSN that includes not only the GSN, GEOSCOPE, and the GEOFON global seismic networks but also regional networks of permanent seismometer installations such as the German GRSN, the Canadian Digital Seismic Network, the Italian MedNet, the Japanese F-net, and the Californian TERRAscope and BDSN. Some of these have been recording continuously for 25 years or longer or have replaced earlier networks, such as the DWSSN and SRO. The observation of normal modes, with periods up to 54 min, requires a very long-period sensor, and some of the best early digital observations were collected on LaCoste–Romberg gravimeters (e.g., IDA; Agnew et al., 1976) that have been used primarily to observe tides. The disadvantage of recording with gravimeters is that we collect only the vertical ground movement. Also, the first few wave trains in earlier recordings of large earthquakes were typically saturated. More modern equipment therefore includes a very broadband three-component seismometer, such as the Wieland–Streckeisen STS-1 vault seismometer or the Geotech–Teledyne KS-54000 borehole seismometer. Though some individual installations of the broadband STS-2s deliver spectacular low-frequency spectra, more often, the signals of the gravest modes are buried in the noise. STS-1 and KS-54000 are no longer produced. As

sensors age and start to fail, we are losing some of the best and quietest stations that collected records of memorable quality. For example, at the old IDA/UCLA station SPA at the South Pole, the gravimeter recorded the deep 09 June 1994 Bolivia earthquake, which is, to this day and after the 2011 Tohoku, Japan earthquake, the best digitally recorded deep earthquake to study many overtone modes, including IC-sensitive modes. The station was closed soon after 'Bolivia,' and the site was equipped with seismometers and operated under the GSN umbrella. Though the installation included an STS-1, the 1994 Bolivia spectrum was the last and one of very few noteworthy normal mode spectra collected at SPA. Spectra collected at Earth's poles are invaluable to us because they provide the unique opportunity to study in detail the $m=0$ singlet of a mode. To this day, some $m=0$ singlets, such as that of IC-sensitive mode ${}_3S_2$, have not yet been observed, and we have yet to understand whether this is caused by Earth structure, low excitation by the seismic source, or high noise levels at SPA. The low signal quality at SPA has been known for many years, but such a station is extremely difficult to operate, not lastly for environmental reasons. It is therefore not surprising that it took almost 10 years before new equipment was installed at the new site QSPA, not too far away. The 2004 Sumatra–Andaman earthquake did produce a nice spectrum at QSPA, but this earthquake was exceptionally large. For the more recent, slightly smaller 2011 Tohoku, Japan earthquake, the spectrum of the primary sensor at QSPA, a KS-54000, was so noisy that mode 1S4, that sits between fundamental modes 0S6 and 0S7, was not observable. Note though that the secondary sensor, a Güralp CMG-3T, produced a much cleaner spectrum, with 1S4 clearly visible above the noise, but not 3S2. It still remains to be seen, if the 1994 Bolivia SPA spectrum can be reproduced in the future. The GSN is now a decade past reaching its design goals (Butler et al., 2004). No new stations have come online and the networks are past the transition from a R&D (research and development) to an O&M (operation and maintenance) modus operandi. To guarantee the data flow that we enjoy today requires the continued commitment of network operators to maintain stations at observatory-quality level, preferably at remote, low-noise locations. Amazingly enough, some network operators have run these networks on budgets that have not increased or, at the least, kept up with inflation rates. In today's world of high-resolution tomography and squeezed in between large but temporary projects such as the US EarthScope initiative and other high-visibility endeavors, it is becoming increasingly difficult to make the case for running, and funding, a permanent very long-period global seismic network. There are many yet unresolved problems in the Earth sciences to which normal mode seismology may hold the crucial clues, if not the only ones. Our greatest commitment therefore must be to ensure that we have not yet passed the golden age of normal mode observational seismology. Recent advances in ocean technology now allow year-long temporary deployments of broadband seismometers on the ocean floor that are routinely installed as primary sensors at permanent seismic observatories. Some deep-ocean deployments have produced very promising vertical-component spectra that could fill in crucial gaps in the current global coverage of GSN spectra. During the Hawaiian PLUME ocean bottom seismometer (OBS) deployment (Laske

et al., 2009), we gathered several GSN-quality spectra for earthquakes much smaller than the 2011 Tohoku, Japan earthquake. For the $M_s=8.3$ 15 Nov 2006 Kuril Islands earthquake, we observed modes 0S6 and 3S2 – and even 0S5 – routinely on unburied Nanometrics Trillium 240 sensors, and on some Güralp CMG-3T sensors. Burial of the sensor is expected to significantly reduce tilt noise on all three components but particularly so on the horizontal components (Collins et al., 2001). Real-time access to OBS observatories can be provided through communication cables such as station H2O halfway between Hawaii and Oregon or through moored buoys. Innovative wave glider technology could provide real-time access to OBSs that are not serviced by cable or moorings (Laske et al., 2014). Advances in both battery and data acquisition technology nurture realistic hopes that an expansion of the GSN into the remote oceans is within our reach.

Acknowledgments

We wish to thank the network and station operators for their unselfish long-term commitment to continuously and consistently collect high-quality long-period seismic data. Foremost among these are GEOSCOPE (France), IRIS–IDA (UC San Diego, the United States), IRIS–USGS (ASL Albuquerque), GEOFON (GFZ, Potsdam, Germany), TERRAscope/TriNet (Caltech, the United States), BDSN (UC Berkeley, California), GRSN (SZGRF, Erlangen, Germany), BFO (Black Forest Observatory, Germany), and the operators of superconducting gravimeters. Thanks also go to IRIS, FDSN, the global geodynamics project (GGP; Crossley et al., 1999), and all data management centers for freely and readily making the data available to us. This research was funded by grants EAR03-36864 and EAR12-15636 of the US National Science Foundation.

References

- Agnew DC, Berger J, Buland R, Farrell WE, and Gilbert JF (1976) International deployment of accelerometers: A network for very long period seismology. *EOS. Transactions of the American Geophysical Union* 77: 180–188.
- Agnew DC, Berger J, Farrell WE, Gilbert JF, Masters G, and Miller D (1986) Project IDA: A decade in review. *EOS. Transactions of the American Geophysical Union* 67: 203–212.
- Aki K and Richards PG (1980) *Quantitative Seismology, Theory and Methods*. San Francisco, FL: W.H. Freeman.
- Aki K and Richards PG (2002) *Quantitative Seismology, Theory and Methods*. San Francisco, FL: University Science Books.
- Alsina D and Snieder R (1993) A test of the great circle approximation in the analysis of surface waves. *Geophysical Research Letters* 20: 915–928.
- Backus G (1962) The propagation of short elastic surface waves on a slowly rotating Earth. *Bulletin of the Seismological Society of America* 52: 823–846.
- Backus G (1964) Geographical interpretation of measurements of average phase velocities of surface waves over great circular and great semi-circular paths. *Bulletin of the Seismological Society of America* 54: 571–610.
- Backus G (1967) Converting vector and tensor equations to scalar equations in spherical coordinates. *Geophysical Journal of the Royal Astronomical Society* 13: 71–101.
- Backus G and Gilbert F (1968) The resolving power of gross Earth data. *Geophysical Journal of the Royal Astronomical Society* 16: 169–205.
- Beghein C and Trampert J (2004) Probability density functions for radial anisotropy from fundamental mode surface wave data and the neighbourhood algorithm. *Geophysical Journal International* 157: 1163–1174.

- Benioff H, Harrison JC, LaCoste L, Munk WH, and Slichter LB (1959) Searching for the Earth's free oscillations. *Journal of Geophysical Research* 64: 1334.
- Ben-Menahem A and Singh SJ (1981) *Seismic Waves and Sources*. New York: Springer.
- Bensen GD, Ritzwoller MH, Barmin MP, et al. (2007) Processing seismic ambient noise data to obtain reliable broad-band surface wave dispersion measurements. *Geophysical Journal International* 169: 1239–1260.
- Berckhemer H (1956) Rayleigh-wave dispersion and crustal structure in the East Atlantic Ocean basin. *Bulletin of the Seismological Society of America* 46: 83–86.
- Beuclet É, Stutzmann É, and Montagner J-P (2003) Surface wave higher-mode phase velocity measurements using a roller-coaster-type algorithm. *Geophysical Journal International* 155: 289–307.
- Billien M, Lévêque J-J, and Trampert J (2000) Global maps of Rayleigh wave attenuation for periods between 40 and 150 seconds. *Geophysical Research Letters* 27: 3619–3622.
- Biswas NN and Knopoff L (1970) Exact Earth-flattening calculation for Love waves. *Bulletin of the Seismological Society of America* 60: 1123–1137.
- Blackman RB and Tukey JW (1958) *The Measurement of Power Spectra*. New York: Dover.
- Boore DM (1969) Effect of higher mode contamination on measured Love wave phase velocities. *Journal of Geophysical Research* 74: 6612–6616.
- Bromirski PD and Duennebieber FK (2002) The near-coastal microseism spectrum: Spatial and temporal wave climate relationships. *Journal of Geophysical Research* 107: 2166–2185.
- Bromirski PD and Gerstoft P (2009) Dominant source regions of the Earth's hum are coastal. *Geophysical Research Letters* 36: L13303. <http://dx.doi.org/10.1029/2009GL038903>.
- Brune J and Dorman J (1963) Seismic waves and Earth structure in the Canadian shield. *Bulletin of the Seismological Society of America* 53: 167–209.
- Brune JN, Nafe JE, and Alsop LE (1961) The polar phase shift of surface waves on a sphere. *Bulletin of the Seismological Society of America* 51: 247–257.
- Buland R, Berger J, and Gilbert F (1979) Observations from the IDA network of attenuation and splitting during a recent earthquake. *Nature* 277: 358–362.
- Butler R, Lay T, Creager K, et al. (2004) The global seismographic network surpasses its design goal. *EOS, Transactions of the American Geophysical Union* 85: 225–229.
- Capdeville Y, Chaljub E, Vilotte JP, and Montagner JP (2003) Coupling the spectral element method with a modal solution for elastic wave propagation in global Earth models. *Geophysical Journal International* 152: 34–67.
- Capon J (1970) Analysis of Rayleigh-wave multipath propagation at LASA. *Bulletin of the Seismological Society of America* 60: 1701–1731.
- Cara M (1973) Filtering of dispersed wavetrains. *Geophysical Journal of the Royal Astronomical Society* 33: 65–80.
- Cara M (1978) Regional variations of higher Rayleigh-mode phase velocities: A spatial-filtering method. *Geophysical Journal of the Royal Astronomical Society* 54: 439–460.
- Cara M and Lévêque J-J (1987) Waveform inversion using secondary observables. *Geophysical Research Letters* 14: 1046–1049.
- Cara M, Minster J-B, and Le Bras R (1981) Multi-mode analysis of Rayleigh-type L_g . Part 2: Application to Southern California and the Northwestern Sierra Nevada. *Bulletin of the Seismological Society of America* 71: 985–1002.
- Carder DS (1934) Seismic surface waves and the crustal structure of the Pacific region. *Bulletin of the Seismological Society of America* 24: 231–302.
- Chaljub E and Valette B (2004) Spectral element modelling of three-dimensional wave propagation in a self-gravitating Earth with an arbitrarily stratified outer core. *Geophysical Journal International* 158: 131–141.
- Clévéde É, Mégnin C, Romanowicz B, and Lognonné P (2000) Seismic waveform modeling and surface wave tomography in a three-dimensional Earth: Asymptotic and non-asymptotic approaches. *Physics of the Earth and Planetary Interiors* 119: 37–56.
- Collins JA, Vernon FL, Orcutt JA, et al. (2001) Broadband Seismology in the Oceans: Lessons from the Ocean Seismic Network Pilot Experiment. *Geophysical Research Letters* 28: 49–52.
- Cooley JW and Tukey JW (1965) An algorithm for the machine computation of complex Fourier series. *Mathematics of Computation* 19: 297–301.
- Cotte N, Pedersen HA, Campillo M, Farra V, and Cansi Y (2000) Off-great-circle propagation of intermediate-period surface waves observed on a dense array in the French Alps. *Geophysical Journal International* 142: 825–840.
- Creager KC (1997) Inner core rotation rate from small-scale heterogeneity and time-varying travel times. *Science* 278: 1248–1288.
- Creager KC (2000) Inner core anisotropy and rotation. In: Karato S-i, Forte AM, Libermann RC, Masters G, and Stixrude L (eds.) *Earth's Deep Interior: Mineral Physics and Tomography*. AGU Monograph, 117, pp. 89–114. Washington, DC: American Geophysical Union.
- Crossley D, Hinderer J, Casula G, et al. (1999) Network of superconducting gravimeters benefit a number of disciplines. *EOS, Transactions of the American Geophysical Union* 80: 125–126.
- Dahlen FA (1968) The normal modes of a rotating, elliptical Earth. *Geophysical Journal of the Royal Astronomical Society* 16: 329–367.
- Dahlen FA (1982) The effect of data windows on the estimation of free oscillation parameters. *Geophysical Journal of the Royal Astronomical Society* 69: 537–549.
- Dahlen FA and Sailor RV (1979) Rotational and elliptical splitting of the free oscillations of the Earth. *Geophysical Journal of the Royal Astronomical Society* 58: 609–623.
- Dahlen FA and Tromp J (1998) *Theoretical Global Seismology*. Princeton, NJ: Princeton University Press, p. 1025.
- Dalton C and Ekström G (2006) Constraints on global maps of phase velocity from surface-wave amplitudes. *Geophysical Journal International* 161: 820–826.
- Debayle E and Lévêque J-J (1997) Upper mantle heterogeneities in the Indian ocean from waveform inversion. *Geophysical Research Letters* 24: 245–248.
- Deuss A, Ritsema R, and van Heijst H (2013) A new catalogue of normal-mode splitting function measurements up to 10 mHz. *Geophysical Journal International* 193: 920–937.
- Deuss A and Woodhouse J (2001) Theoretical free-oscillation spectra; the importance of wide band coupling. *Geophysical Journal International* 146: 833–842.
- Deuss A and Woodhouse J (2004) Iteration method to determine the eigenvalues and eigenvectors of a target multiplet including full mode coupling. *Geophysical Journal International* 159: 326–332.
- Dobrin MB, Simon RF, and Lawrence PL (1951) Rayleigh waves from small explosions. *Transactions of the American Geophysical Union* 32: 822–832.
- Donn WL and Blaik M (1953) A study and evaluation of the tripartite seismic method of locating hurricanes. *Bulletin of the Seismological Society of America* 43: 311–329.
- Dratler J, Farrell W, Block B, and Gilbert F (1971) High-Q overtone modes of the Earth. *Geophysical Journal of the Royal Astronomical Society* 23: 399–410.
- Durek JJ and Ekström G (1996) A model of radial anelasticity consistent with observed surface wave attenuation. *Bulletin of the Seismological Society of America* 66: 144–158.
- Durek JJ, Ritzwoller MH, and Woodhouse JH (1993) Constraining upper mantle anelasticity using surface wave amplitude anomalies. *Geophysical Journal International* 114: 249–272.
- Dziewonski AM (1970) On regional differences in dispersion of mantle Rayleigh waves. *Geophysical Journal of the Royal Astronomical Society* 22: 289–325.
- Dziewonski AM and Anderson DL (1981) Preliminary reference Earth model. *Physics of the Earth and Planetary Interiors* 25: 297–356.
- Dziewonski AM, Bloch S, and Landisman M (1969) A technique for the analysis of transient seismic signals. *Bulletin of the Seismological Society of America* 59: 427–444.
- Dziewonski AM, Chou TA, and Woodhouse JH (1981) Determination of earthquake source parameters from waveform data for studies of global and regional seismicity. *Journal of Geophysical Research* 86: 2825–2852.
- Dziewonski AM and Gilbert F (1971) Solidity of the inner core of the Earth inferred from normal mode observations. *Nature* 234: 465–466.
- Dziewonski AM and Gilbert F (1972) Observations of normal modes from 84 recordings of the Alaskan earthquake of 1964 March 28. *Geophysical Journal of the Royal Astronomical Society* 27: 393–446.
- Dziewonski AM, Hales A, and Lapwood E (1975) Parametrically simple earth models consistent with geophysical data. *Physics of the Earth and Planetary Interiors* 10: 12–48.
- Dziewonski AM and Landisman M (1970) Great circle Rayleigh and Love wave dispersion from 100 to 900 seconds. *Geophysical Journal of the Royal Astronomical Society* 19: 37–91.
- Dziewonski AM, Mills J, and Bloch S (1972) Residual dispersion measurement – A new method of surface-wave analysis. *Bulletin of the Seismological Society of America* 62: 129–139.
- Dziewonski AM and Steim J (1982) Dispersion and attenuation of mantle waves through wave-form inversion. *Geophysical Journal of the Royal Astronomical Society* 70: 503–527.
- Ekström G (2001) Time domain analysis of the Earth's long-period background seismic radiation. *Journal of Geophysical Research* 106: 26483–26494.
- Ekström G (2011) A global model of Love and Rayleigh surface wave dispersion and anisotropy, 25–250 s. *Geophysical Journal International* 187: 1668–1686.
- Ekström G and Dziewonski AM (1998) The unique anisotropy of the Pacific upper mantle. *Nature* 394: 168–172.
- Ekström G, Tromp J, and Larson EW (1997) Measurements and models of global surface wave propagation. *Journal of Geophysical Research* 102: 8137–8157.
- Ekström G, Nettles M, and Dziewonski AM (2012) The global CMT project 2004–2010. Centroid-moment tensors for 13,017 earthquakes. *Physics of the Earth Planetary Interiors* 200–201: 1–9. <http://dx.doi.org/10.1016/j.pepi.2012.04.002>.

- Essen H-H, Krüger F, Dahm T, and Grevermeyer I (2003) On the generation of secondary microseisms observed in northern and central Europe. *Journal of Geophysical Research* 108: 2506. <http://dx.doi.org/10.1029/2002JB002338>.
- Evernden JE (1953) Direction of approach of Rayleigh waves and related problems. Part I. *Bulletin of the Seismological Society of America* 43: 335–357.
- Evernden JE (1954) Direction of approach of Rayleigh waves and related problems. Part II. *Bulletin of the Seismological Society of America* 44: 159–184.
- Ewing M, Jardetzky WS, and Press F (1957) *Elastic Waves in Layered Media*, p. 380. New York: McGraw-Hill Book Company.
- Ewing M and Press F (1952) Crustal structure and surface wave dispersion, Part 2. *Bulletin of the Seismological Society of America* 42: 315–325.
- Ewing M and Press F (1954) An investigation of mantle Rayleigh waves. *Bulletin of the Seismological Society of America* 44: 127–147.
- Ewing M and Press F (1956) Rayleigh wave dispersion in the period range 10 to 500 seconds. *Transactions of the American Geophysical Union* 37: 213–215.
- Forsyth D and Li A (2005) Array-analysis of two-dimensional variations in surface wave phase velocity and azimuthal anisotropy in the presence of multi-pathing interference. In: Levander A and Nolet G (eds.) *Seismic Earth: Array Analysis of Broadband Seismograms*. *Geophysical Monograph*, 157, pp. 81–97. Washington, DC: American Geophysical Union.
- Friederich W, Hunzinger S, and Wielandt E (2000) A note on the interpretation of seismic surface waves over three-dimensional structures. *Geophysical Journal International* 143: 335–339.
- Friederich W, Wielandt E, and Stange S (1993) Multiple forward scattering of surface waves; comparison with an exact solution and Born single-scattering methods. *Geophysical Journal International* 112: 264–275.
- Friederich W, Wielandt E, and Stange S (1994) Non-plane geometries of seismic surface wavefields and their implications for regional surface-wave tomography. *Geophysical Journal International* 119: 931–948.
- Friedrich A, Krüger F, and Klinge K (1998) Ocean generated microseismic noise located with the Gräfenberg array. *Journal of Seismology* 2: 47–64.
- Fukao Y, Nishida K, and Kobayashi N (2010) Seafloor topography, ocean infragravity waves, and background Love and Rayleigh waves. *Journal of Geophysical Research* 115: B04302. <http://dx.doi.org/10.1029/2009JB006678>.
- Gabor D (1947) Acoustical quanta and the theory of hearing. *Nature* 159: 591–594.
- Galagher B (1971) Generation of surf beat by non-linear wave interactions. *Journal of Fluid Mechanics* 49: 1–20.
- Geller RJ and Takeuchi N (1995) A new method for computing highly accurate DSM synthetic seismograms. *Geophysical Journal International* 123: 449–470.
- Giardini D, Li X-D, and Woodhouse JH (1987) Three-dimensional structure of the Earth from splitting in free oscillation spectra. *Nature* 325: 405–411.
- Gilbert F (1971) The diagonal sum rule and averaged eigenfrequencies. *Geophysical Journal of the Royal Astronomical Society* 23: 119–123.
- Gilbert F (1980) An introduction to low-frequency seismology. In: *Proceedings of the Enrico Fermi Summer School of 1979* 41–81.
- Gilbert F (2001) Vandermonde matrix analysis of long-period seismograms. *Geophysical Journal International* 146: 843–849.
- Gilbert F and Dziewonski AM (1975) An application of normal mode theory to the retrieval of structural parameters and source mechanisms from seismic spectra. *Philosophical Transactions of the Royal Society A* 278: 187–269.
- Gu YJ and Dziewonski AM (1999) Mantle discontinuities and 3-D tomographic models. *EOS. Transactions of the American Geophysical Union* 80: F717.
- Gung Y and Romanowicz B (2004) Q tomography of the upper mantle using three-component long-period waveforms. *Geophysical Journal International* 157: 813–830.
- Gutenberg B and Richter CF (1936) On seismic waves, 3rd paper. *Gerlands Beitrage Zur Geophysik* 47: 73–131.
- Hanka W and Kind R (1994) The GEOFON program. *IRIS Newsletter* XIII: 1–4.
- Harmon N, Forsyth D, and Webb S (2007) Using ambient seismic noise to determine short-period phase velocities and shallow shear velocities in young oceanic lithosphere. *Bulletin of the Seismological Society of America* 97: 2009–2023.
- Harmon N, Gerstoft P, Rychert CA, Abers GA, Salas de la Cruz M, and Fischer KM (2008) Phase velocities from seismic noise using beamforming and cross correlation in Costa Rica and Nicaragua. *Geophysical Research Letters* 35: L19303. <http://dx.doi.org/10.1029/2008GL035387>.
- Harmon N, Rychert C, and Gerstoft P (2010) Distribution of noise sources for seismic interferometry. *Geophysical Journal International* 183: 1470–1484.
- Harris F (1978) On the use of windows for harmonic analysis with the discrete Fourier transform. *Proceedings of the IEEE* 66: 51–83.
- He X and Tromp J (1996) Normal-mode constraints on the structure of the Earth. *Journal of Geophysical Research* 87: 7772–7778.
- Henson IH (1989) Multiplet coupling of the normal modes of an elliptical, transversely isotropic Earth. *Geophysical Journal International* 98: 457–459.
- Herrin E and Goforth T (1977) Phase-matched filters: Application to the study of Rayleigh waves. *Bulletin of the Seismological Society of America* 67: 1259–1275.
- Hiller G, Graham N, Campillo M, Kedar S, Landès M, and Shapiro N (2012) Global oceanic microseism sources as seen by seismic arrays and predicted by wave action models. *Geochemistry, Geophysics, Geosystems* 13: Q01021. <http://dx.doi.org/10.1029/2011GC003875>.
- Hu X-G, Liu L-T, Hinderer J, Hsu HT, and Sun H-P (2006) Wavelet filter analysis of atmospheric pressure effects in the long-period seismic mode band. *Physics of the Earth and Planetary Interiors* 154: 70–84.
- Ishii M and Tromp J (1999) Normal-mode and free-air gravity constraints on lateral variations in velocity and density of Earth's mantle. *Science* 285: 1231–1236.
- Jeans JH (1923) The propagation of earthquake waves. *Gerlands Beitrage Zur Geophysik A* 102: 554–574.
- Jenkins GM (1961) General considerations in the analysis of spectra. *Technometrics* 3: 133–166.
- Jobert N and Roullet G (1976) Periods and damping of free oscillations observed in France after sixteen earthquakes. *Geophysical Journal of the Royal Astronomical Society* 45: 155–176.
- Jobert N and Roullet G (1978) Evidence of lateral variations from free oscillations and surface waves. *Geophysical Research Letters* 5: 569–572.
- Jordan T (1978) A procedure for estimating lateral variations from low-frequency eigenspectra data. *Geophysical Journal of the Royal Astronomical Society* 52: 441–455.
- Jurkevics A (1988) Polarization analysis of three-component array data. *Seismological Society of America* 78: 1725–1743.
- Kanamori H (1970) Velocity and Q of the mantle waves. *Physics of the Earth and Planetary Interiors* 2: 259–275.
- Kedar S, Longuet-Higgins M, Webb F, Graham N, Clayton R, and Jones C (2008) The origin of deep ocean microseisms in the Northern Atlantic Ocean. *Proceedings of the Royal Society A* 464: 777–793.
- Keilis-Borok VI and Yanovskaja TB (1967) Inverse problems of seismology (Structural Review). *Geophysical Journal of the Royal Astronomical Society* 13: 223–234.
- Kellogg LH, Hager BH, and van der Hilst RD (1999) Compositional stratification in the deep mantle. *Science* 283: 1881–1884.
- Knopoff L (1972) Observation and inversion of surface-wave dispersion. *Tectonophysics* 13: 497–519.
- Knopoff L, Berry MJ, and Schwab FA (1967) Tripartite phase velocity observations in laterally heterogeneous regions. *Journal of Geophysical Research* 72: 2595–2601.
- Knopoff L, Mueller S, and Pilant WL (1966) Structure of the crust and upper mantle in the Alps from the phase velocity of Rayleigh waves. *Bulletin of the Seismological Society of America* 56: 1009–1044.
- Komatitsch D, Ritsema J, and Tromp J (2002) The spectral-element method, Beowulf computing, and global seismology. *Science* 298: 1737–1742.
- Komatitsch D and Tromp J (2002) Spectral-element simulations of global seismic wave propagation. Part II: Three-dimensional models, oceans, rotation and self-gravitation. *Geophysical Journal International* 150: 303–318.
- Komatitsch D and Vilotte J-P (1998) The spectral element method: An efficient tool to simulate the seismic response of 2D and 3D geological structure. *Bulletin of the Seismological Society of America* 88: 368–392.
- Koptschalitsch G (1988) *Die Anwendung der zeitvariablen Filterung bei der Eigenschwingungs-analyse*. Masters Thesis. Germany: Universität Karlsruhe.
- Kurrie D and Widmer-Schnidrig R (2006) Spatiotemporal features of the Earth's background oscillations observed in central Europe. *Geophysical Research Letters* 33: L24304. <http://dx.doi.org/10.1029/2006GL028429>.
- Kurrie D and Widmer-Schnidrig R (2008) The horizontal hum of the Earth: A global background of spheroidal and toroidal modes. *Geophysical Research Letters* 35: L06304. <http://dx.doi.org/10.1029/2007GL033125>.
- Kurrie D and Widmer-Schnidrig R (2010) Excitation of long-period Rayleigh wave by large storms over the North Atlantic Ocean. *Geophysical Journal International* 183: 330–338.
- Landau LD and Lifshitz EM (1958) *Quantum Mechanics*, p. 515. Reading, MA: Addison Wesley.
- Landisman M, Dziewonski A, and Satô Y (1969) Recent improvements in the analysis of surface wave observations. *Geophysical Journal of the Royal Astronomical Society* 17: 369–403.
- Larson EWF and Ekström G (2002) Determining surface wave arrival angle anomalies. *Journal of Geophysical Research* 107. <http://dx.doi.org/10.1029/2000JB000048>.
- Laske G (1995) Global observation of off-great-circle propagation of long-period surface waves. *Geophysical Journal International* 123: 245–259.
- Laske G and Masters G (1996) Constraints on global phase velocity maps from long-period polarization data. *Journal of Geophysical Research* 101: 16059–16075.

- Laske G and Masters G (1999) Limits on the rotation of the inner core from a new analysis of free oscillations. *Nature* 402: 66–69.
- Laske G and Masters G (2003) The Earth's free oscillations and the differential rotation of the inner core. In: Dehant V, Creager K, Zatman S, and Karato S-I (eds.) *Earth's Core: Dynamics, Structure, Rotation. Geodynamics Series* 31, pp. 5–21. Washington, DC: AGU.
- Laske G, Masters G, and Dziewonski AM (2001) New measurements of radial mode eigenfrequencies. *EOS. Transactions of the American Geophysical Union* 82: F873.
- Laske G, Phipps Morgan J, and Orcutt J (1998) First results from the Hawaiian SWELL pilot experiment. *Geophysical Research Letters* 26: 3397–3400.
- Laske G, Collins JA, Wolfe CJ, et al. (2009) Probing the Hawaiian Hot Spot With New Broadband Ocean Bottom Instruments. *EOS. Transactions of the American Geophysical Union* 90: 362–363.
- Laske G, Berger J, Orcutt J, and Babcock J (2014) ADDOSS: Autonomously Deployed Deep-ocean Seismic System - Communications Gateway for Ocean Observatories. *Geophysical Research Abstracts* 16: EGU General Assembly 2014: EGU2014-4707.
- Lebedev S, Nolet G, Meier T, and van der Hilst RD (2005) Automated multimode inversion of surface and S waveforms. *Geophysical Journal International* 162: 951–964.
- Lerner-Lam AL and Park JJ (1989) Frequency-dependent refraction and multipathing of 10–100 second surface waves in the Western Pacific. *Geophysical Research Letters* 16: 527–530.
- Levin V and Park J (1998) Quasi-Love phases between Tonga and Hawaii: Observations, simulations, and explanations. *Journal of Geophysical Research* 103: 24321–24331.
- Levshin AL, Pisarenko VF, and Pogrebinsky GA (1972) On a frequency-time analysis of oscillations. *Annales Geophysicae* 28: 211–218.
- Levshin AL, Ritzwoller MH, and Resovsky J (1999) Source effects on surface wave group travel times and group velocity maps. *Physics of the Earth and Planetary Interiors* 115: 293–312.
- Levshin AL, Yanovskaya TB, Lander AV, et al. (1989) Recording identification and measurements of surface wave parameters. In: Keilis-Borok VI (ed.) *Seismic Surface Waves in a Laterally Inhomogeneous Earth*, pp. 131–182. Dordrecht: Kluwer.
- Li X-D, Giardini D, and Woodhouse JH (1991a) Large-scale three-dimensional even-degree structure of the Earth from splitting of long-period normal modes. *Journal of Geophysical Research* 96: 551–557.
- Li X-D, Giardini D, and Woodhouse JH (1991b) The relative amplitudes of mantle heterogeneity in P velocity, S velocity, and density from free oscillation data. *Geophysical Journal International* 105: 649–657.
- Li X-D and Romanowicz B (1995) Comparison of global waveform inversions with and without considering cross-branch modal coupling. *Geophysical Journal International* 121: 695–709.
- Li X-D and Romanowicz B (1996) Global mantle shear velocity model developed using non-linear asymptotic coupling theory. *Journal of Geophysical Research* 101: 22245–22272.
- Lilly JM and Park J (1995) Multiwavelet spectral and polarization analyses of seismic records. *Geophysical Journal International* 122: 1001–1021.
- Lin F-C, Moschetti MP, and Ritzwoller MH (2008) Surface wave tomography of the western United States from ambient seismic noise: Rayleigh and Love wave phase velocity maps. *Geophysical Journal International* 173: 281–298.
- Lin F-C and Ritzwoller MH (2011) Helmholtz surface wave tomography for isotropic and azimuthally anisotropic structure. *Geophysical Journal International* 186: 1104–1120.
- Lin F-C, Ritzwoller MH, Yang Y, Moschetti MP, and Fouch MJ (2011) Complex and variable crustal and uppermost mantle seismic anisotropy in the western United States. *Nature Geoscience* 4: 55–61. <http://dx.doi.org/10.1038/NNGEO1036>.
- Lindberg CR and Park J (1987) Multiple-taper spectral analysis of terrestrial free oscillations, Part II. *Geophysical Journal of the Royal Astronomical Society* 91: 795–836.
- Lognonné P (1991) Normal modes and seismograms in an anelastic rotating Earth. *Journal of Geophysical Research* 96: 20309–20319.
- Lognonné P and Romanowicz B (1990) Modelling of coupled normal modes of the Earth: The spectral method. *Geophysical Journal International* 102: 365–395.
- Longuet-Higgins M (1950) A theory of the origin of microseisms. *Philosophical Transactions of the Royal Society of London A* 243: 1–35.
- Love AEH (1927) *A Treatise on the Mathematical Theory of Elasticity*, 4th edn, pp. 1–35. Cambridge: Cambridge University Press.
- Masters TG (2011) Free oscillations for fun and profit (Beno Gutenberg Medal Lecture). *Geophysical Research Abstracts* 13: EGU2011–EGU14185.
- Masters G and Gilbert F (1981) Structure of the inner core inferred from observations of its spheroidal shear modes. *Geophysical Research Letters* 8: 569–571.
- Masters G and Gilbert F (1983) Attenuation in the Earth at low frequencies. *Philosophical Transactions of the Royal Society of London A* 308: 479–522.
- Masters TG and Gubbins D (2003) On the resolution of density within the Earth. *Physics of the Earth and Planetary Interiors* 140: 159–167.
- Masters G, Johnson S, Laske G, and Bolton H (1996) A shear velocity model of the mantle. *Philosophical Transactions of the Royal Society of London A* 354: 1385–1411.
- Masters G, Jordan TH, Silver PG, and Gilbert F (1982) Aspherical Earth structure from fundamental spheroidal-mode data. *Nature* 298: 609–613.
- Masters G and Laske G (1997) On bias in surface wave and free oscillation attenuation measurements. *EOS. Transactions of the American Geophysical Union* 78: F485.
- Masters G, Laske G, Bolton H, and Dziewonski A (2000) The relative behavior of shear velocity, bulk sound speed, and compressional velocity in the mantle: Implications for chemical and thermal structure. In: Karato S-I, Forte AM, Libermann RC, Masters G, and Stixrude L (eds.) *Earth's Deep Interior: Mineral Physics and Tomography. AGU Monograph* 117: pp. 63–87. Washington, DC: American Geophysical Union.
- Masters TG, Laske G, and Gilbert F (2000a) Autoregressive estimation of the splitting matrix of free-oscillation multiplets. *Geophysical Journal International* 141: 25–42.
- Masters TG, Laske G, and Gilbert F (2000b) Matrix autoregressive analysis of free-oscillation coupling and splitting. *Geophysical Journal International* 143: 478–489.
- Masters TG, Laske G, and Gilbert F (2000c) Large-scale Earth structure from analyses of free oscillation splitting and coupling. In: Boschi E, Ekström G, and Morelli A (eds.) *Problems in Geophysics for the New Millennium*, pp. 255–288. Bologna: Editrice Compositori.
- Masters G, Park J, and Gilbert F (1983) Observations of coupled spheroidal and toroidal modes. *Journal of Geophysical Research* 88: 10285–10298.
- Masters TG and Widmer R (1995) Free-oscillations: Frequencies and attenuations. In: Ahrens Th J (ed.) *Global Earth Physics: A Handbook of Physical Constants*, pp. 104–125. Washington, DC: American Geophysical Union.
- Maupin V (1992) Modelling of laterally trapped surface waves with application to Rayleigh waves in the Hawaiian swell. *Geophysical Journal International* 110: 533–570.
- McEvilly TV (1964) Central US crust-upper mantle structure from Love and Rayleigh wave phase velocity inversion. *Bulletin of the Seismological Society of America* 54: 1997–2015.
- Mégnin C and Romanowicz B (1999) The effects of the theoretical formalism and data selection on mantle models derived from waveform tomography. *Geophysical Journal International* 138: 366–380.
- Mégnin C and Romanowicz B (2000) The 3D shear velocity of the mantle from the inversion of body, surface, and higher mode waveforms. *Geophysical Journal International* 143: 709–728.
- Meier T, Dietrich K, Stöckhert B, and Harjes H-P (2004) One-dimensional models of shear wave velocity for the eastern Mediterranean obtained from the inversion of Rayleigh wave phase velocities and tectonic implications. *Geophysical Journal International* 156: 45–58.
- Meier T, Lebedev S, Nolet G, and Dahlen FA (1997) Diffraction tomography using multimode surface waves. *Journal of Geophysical Research* 102: 8255–8267.
- Mendiguren JA (1973) Identification of free oscillation spectral peaks for 1970 July 31, Colombian deep shock using the excitation criterion. *Geophysical Journal of the Royal Astronomical Society* 33: 281–321.
- Millot-Langet R, Clévédy E, and Lognonné P (2003) Normal modes and long period seismograms in a 3D anelastic elliptical rotating Earth. *Geophysical Research Letters* 30. <http://dx.doi.org/10.1029/2002GL016257>.
- Mochizuki E (1986a) Free oscillations and surface waves in an aspherical Earth. *Geophysical Research Letters* 13: 1478–1481.
- Mochizuki E (1986b) The free oscillations of an anisotropic and heterogeneous Earth. *Geophysical Journal of the Royal Astronomical Society* 86: 167–176.
- Montagner J-P and Nataf H-C (1986) A simple method for inverting the azimuthal anisotropy of surface waves. *Journal of Geophysical Research* 91: 511–520.
- Montagner J-P and Nataf H-C (1988) Vectorial tomography. Part I: Theory. *Journal of Geophysical Research* 94: 295–307.
- Nafe JE and Brune JN (1960) Observations of phase velocity for Rayleigh waves in the period range 100–400 s. *Bulletin of the Seismological Society of America* 50: 427–439.
- Nawa K, Suda N, Fukao Y, Sato T, Aoyama Y, and Shibuya K (1998) Incessant excitation of the Earth's free oscillations. *Earth, Planets and Space* 50: 3–8.
- Nishida K (2013) Earth's background free oscillations. *Annual Review of Earth and Planetary Sciences* 41: 719–740. <http://dx.doi.org/10.1146/annurev-earth-050212-124020>.

- Nishida K and Fukao Y (2007) Source distribution of Earth's background free oscillations. *Journal of Geophysical Research* 112: B06306. <http://dx.doi.org/10.1029/2006JB004720>.
- Nishida K, Kawakatsu H, Fukao Y, and Obara K (2008) Background Love and Rayleigh waves simultaneously generated at the Pacific Ocean floors. *Geophysical Research Letters* 35: L16307. <http://dx.doi.org/10.1029/2008GL034753>.
- Nishida K and Kobayashi N (1999) Statistical features of the Earth's continuous free oscillations. *Journal of Geophysical Research* 104: 28741–28750.
- Nishida K, Kobayashi N, and Fukao Y (2000) Resonant oscillations between the solid Earth and the atmosphere. *Science* 287: 2244–2246.
- Nishida K, Kobayashi N, and Fukao Y (2002) Origin of Earth's ground noise from 2 to 20 mHz. *Geophysical Research Letters* 29(52): 1–4.
- Nishida K, Montagner JP, and Kawakatsu H (2009) Global surface wave tomography using seismic hum. *Science* 326: 112.
- Nolet G (1975) Higher Rayleigh modes in Western Europe. *Geophysical Research Letters* 2: 60–62.
- Nolet G (1990) Partitioned waveform inversion and two-dimensional structure under the network of autonomously recording seismographs. *Journal of Geophysical Research* 95: 8499–8512.
- Oliver J (1962) A summary of observed seismic surface wave dispersion. *Bulletin of the Seismological Society of America* 52: 49–52.
- Oliver J and Ewing M (1957) Higher modes of continental Rayleigh waves. *Bulletin of the Seismological Society of America* 47: 187–204.
- Oliver J and Ewing M (1958) Short-period oceanic surface waves of the Rayleigh and first shear modes. *Transactions of the American Geophysical Union* 39: 483–485.
- Oliver J and Murphy L (1971) WWNSS: Seismology's global network of observing stations. *Science* 174: 254–261.
- Park J and Gilbert F (1986) Coupled free oscillations of an aspherical, dissipative, rotation Earth: Galerkin theory. *Journal of Geophysical Research* 91: 7241–7260.
- Park J, Lindberg CR, and Thomson DJ (1987) Multiple-taper spectral analysis of terrestrial free oscillations, Part I. *Geophysical Journal of the Royal Astronomical Society* 91: 755–794.
- Park J, Lindberg CR, and Vernon FL III (1987) Multitaper spectral analysis of high-frequency seismograms. *Journal of Geophysical Research* 92: 12675–12684.
- Paulssen H, Levshin AL, Lander AV, and Snieder R (1990) Time- and frequency-dependent polarization analysis: Anomalous surface wave observations in Iberia. *Geophysical Journal International* 103: 483–496.
- Pedersen HA (2006) Impacts of non-plane waves on two-station measurements of phase velocities. *Geophysical Journal International* 165: 279–287.
- Pekeris CL (1946) The theory of propagation of sound in a half space of variable sound velocity under conditions of formation of a shadow zone. *Journal of the Acoustical Society of America* 18: 295–315.
- Peterson J (1993) Observations and modeling of seismic background noise. *US Geological Survey, Open-file Report* 93-322, 1–45.
- Peterson J, Hutt CR, and Holcomb LG (1980) Test and calibration of the seismic research observatory. *US Geological Survey, Open-file Report* 80-187, 1–86.
- Peterson J and Tilgner EE (1985) Description and preliminary testing of the CDSN seismic sensor systems. *US Geological Survey, Open-file Report* 85-288, 1–60.
- Pilant WL and Knopoff L (1964) Observations of multiple seismic events. *Bulletin of the Seismological Society of America* 54: 19–39.
- Plesinger A, Hellweg M, and Seidl D (1986) Interactive high-resolution polarization analysis of broad-band seismograms. *Journal of Geophysics* 59: 129–139.
- Polet J and Kanamori H (1997) Upper-mantle shear velocities beneath Southern California determined from long-period surface waves. *Bulletin of the Seismological Society of America* 87: 200–209.
- Pollitz F (1994) Global tomography from Rayleigh and Love wave dispersion: Effect of raypath bending. *Geophysical Journal International* 118: 730–758.
- Press F (1956) Determination of crustal structure from phase velocity of Rayleigh waves. Part I: Southern California. *Bulletin of the Seismological Society of America* 67: 1647–1658.
- Press F (1957) Determination of crustal structure from phase velocity of Rayleigh waves. Part I: San Francisco Bay region. *Bulletin of the Seismological Society of America* 47: 87–88.
- Resovsky J and Ritzwoller M (1995) Constraining odd-degree mantle structure with normal modes. *Geophysical Research Letters* 22: 2301–2304.
- Resovsky J and Ritzwoller M (1998) New and refined constraints on the three-dimensional Earth structure from normal modes below 3 mHz. *Journal of Geophysical Research* 103: 783–810.
- Rhie J and Romanowicz B (2004) Excitation of Earth's continuous free oscillations by atmosphere-ocean-seafloor coupling. *Nature* 431: 552–556.
- Rhie J and Romanowicz B (2006) A study of the relation between ocean storms and the Earth's hum. *Geochemistry, Geophysics, Geosystems* 7. <http://dx.doi.org/10.1029/2006GC001274>.
- Riley KF, Hobson MP, and Bence SJ (2002) *Mathematical Methods for Physics and Engineering*, p. 1232. Cambridge: Cambridge University Press.
- Ritsema J and Van Heijst H (2000) Seismic imaging of structural heterogeneity in Earth's mantle: Evidence for large-scale mantle flow. *Science Progress* 83: 243–259.
- Ritzwoller M, Masters G, and Gilbert F (1986) Observations of anomalous splitting and their interpretation in terms of aspherical structure. *Journal of Geophysical Research* 91: 10203–10228.
- Ritzwoller M, Masters G, and Gilbert F (1988) Constraining aspherical structure with low frequency interaction coefficients: Application to uncoupled multiplets. *Journal of Geophysical Research* 93: 6369–6396.
- Ritzwoller MH, Shapiro NM, Barmin MP, and Levshin AL (2002) Global surface wave diffraction tomography. *Journal of Geophysical Research* 107. <http://dx.doi.org/10.1029/2002JB001777>.
- Röhrbach W (1932) Über die dispersion seismischer Oberflächenwellen. *Zeitschrift für Geophysik* 8: 113–129.
- Romanowicz B (1987) Multiplet–multiplet coupling due to lateral heterogeneity: Asymptotic effects on the amplitude and frequency of the Earth's normal modes. *Geophysical Journal of the Royal Astronomical Society* 90: 75–100.
- Romanowicz B (1994) On the measurement of anelastic attenuation using amplitudes of low-frequency surface waves. *Physics of the Earth and Planetary Interiors* 84: 179–191.
- Romanowicz B (2002) Inversion of surface waves: A review. In: Jennings PC, Kisslinger C, Kanamori H, and Lee WHK (eds.) *International Handbook of Earthquake and Engineering Seismology. International Geophysics*, vol. 81A, pp. 149–173. Amsterdam: Academic Press, International Association of Seismology and Physics of the Earth's Interior Committee on Education.
- Romanowicz B and Bréger L (2000) Anomalous splitting of free oscillations; a reevaluation of possible interpretations. *Journal of Geophysical Research* 105: 21559–21578.
- Romanowicz B, Cara M, Fels JF, and Roult G (1984) GEOSCOPE: A French initiative in long period three component global seismic networks. *Eos, Transactions of the American Geophysical Union* 65: 753–756.
- Romanowicz BA and Dziewonski AM (1986) Toward a federation of broadband seismic networks. *Eos, Transactions of the American Geophysical Union* 67: 541–542.
- Romanowicz B and Roult G (1986) First-order asymptotics for the eigenfrequencies of the Earth and application to the retrieval of large-scale lateral variations of structures. *Geophysical Journal of the Royal Astronomical Society* 87: 209–239.
- Romanowicz B, Roult G, and Kohl T (1987) The upper mantle degree two pattern: Constraints from GEOSCOPE fundamental spheroidal mode eigenfrequency and attenuation measurements. *Geophysical Research Letters* 14: 1219–1222.
- Rosat S, Sato T, Imanishi Y, et al. (2005) High resolution analysis of the gravest seismic normal modes after the 2004 Mw=9 Sumatra earthquake using superconducting gravimeter data. *Geophysical Research Letters* 32: L13304. <http://dx.doi.org/10.1029/2005GL023128>.
- Roult G (1974) Attenuation des ondes sismiques de tres basse frequence. *Annales Geophysicae* 30: 141–167.
- Roult G and Clévédy E (2000) New refinements in attenuation measurements from free-oscillation and surface-wave observations. *Physics of the Earth and Planetary Interiors* 121: 1–37.
- Roult G and Romanowicz B (1984) Very long-period data from the GEOSCOPE network: Preliminary results on great circle averages of fundamental and higher Rayleigh and Love modes. *Bulletin of the Seismological Society of America* 74: 2221–2243.
- Roult G, Romanowicz B, and Jobert N (1986) Observations of departures from classical approximations on very long period GEOSCOPE records. *Annales Geophysicae* 4: 241–249.
- Roult G, Romanowicz B, and Montagner JP (1990) 3-D upper mantle shear velocity and attenuation from fundamental mode free oscillation data. *Geophysical Journal International* 101: 61–80.
- Russell DR, Herrmann RB, and Hwang H-J (1988) Application of frequency variable filters to surface-wave amplitude analysis. *Bulletin of the Seismological Society of America* 78: 339–354.
- Sabra KG, Gerstoft P, Roux P, Kuperman WA, and Fehler MC (2005a) Surface wave tomography from microseisms in Southern California. *Geophysical Research Letters* 32: L14311. <http://dx.doi.org/10.1029/2005GL023155>.
- Sabra KG, Gerstoft P, Roux P, Kuperman WA, and Fehler MC (2005b) Extracting time-domain Greens function estimates from ambient seismic noise. *Geophysical Research Letters* 32: L03310. <http://dx.doi.org/10.1029/2004GL021862>.
- Sambridge M (1999) Geophysical inversion with a neighborhood algorithm. Part I: Searching a parameter space. *Geophysical Journal International* 138: 479–494.
- Savino J, Murphy A, Rynn JM, et al. (1972) Results from the high-gain long-period seismograph experiment. *Geophysical Journal of the Royal Astronomical Society* 31: 179–204.

- Schulte-Pelkum V, Earle PS, and Vernon FL (2004) Strong directivity of ocean-generated seismic noise. *Geochemistry, Geophysics, Geosystems* 5: Q03004. <http://dx.doi.org/10.1029/2003GC000520>.
- Schwab F and Kausel E (1976a) Quadripartite surface wave method: Development. *Geophysical Journal of the Royal Astronomical Society* 45: 231–244.
- Schwab F and Kausel E (1976b) Long-period surface wave seismology: Love wave phase velocity and polar phase shift. *Geophysical Journal of the Royal Astronomical Society* 45: 407–435.
- Selby ND and Woodhouse JH (2000) Controls on Rayleigh wave amplitudes: Attenuation and focusing. *Geophysical Journal International* 142: 933–940.
- Shapiro NM and Campillo M (2004) Emergence of broadband Rayleigh waves from correlations of the ambient seismic noise. *Geophysical Research Letters* 31. <http://dx.doi.org/10.1029/2004GL019491>.
- Shapiro NM, Campillo M, Paul A, Singh SK, Jongmans D, and Sanchez-Sesma J (1997) Surface-wave propagation across the Mexican volcanic belt and origin of the long-period seismic-wave amplification in the Valley of Mexico. *Geophysical Journal International* 128: 151–166.
- Shapiro NM, Campillo M, Stehly L, and Ritzwoller MH (2005) High-resolution surface-wave tomography from ambient seismic noise. *Science* 29: 1615–1617.
- Shapiro NM and Ritzwoller MH (2002) Monte-Carlo inversion for a global shear-velocity model of the crust and upper mantle. *Geophysical Journal International* 151: 88–105.
- Shapiro NM and Singh SK (1999) A systematic error in estimating surface-wave group-velocity dispersion curves and a procedure for its correction. *Bulletin of the Seismological Society of America* 89: 1138–1142.
- Sharrock DS and Woodhouse JH (1998) Investigation of time dependent inner core structure by the analysis of free oscillation spectra. *Earth, Planets and Space* 50: 1013–1018.
- Shearer P (1999) *Introduction to Seismology*, p. 260. New York: Cambridge University Press.
- Simons FJ, van der Hilst RD, Montagner J-P, and Zielhuis A (2002) Multimode Rayleigh wave inversion for heterogeneity and azimuthal anisotropy of the Australian upper mantle. *Geophysical Journal International* 151: 738–754.
- Smith SW (1972) The anelasticity of the mantle. *Tectonophysics* 13: 601–622.
- Smith MF and Masters G (1989a) The effect of Coriolis coupling of free oscillation multiplets on the determination of aspherical Earth structure. *Geophysical Research Letters* 16: 263–266.
- Smith MF and Masters G (1989b) Aspherical structure constraints from free oscillation frequency and attenuation measurements. *Journal of Geophysical Research* 94: 1953–1976.
- Sniieder R and Nolet G (1987) Linearized scattering of surface waves on a spherical Earth. *Journal of Geophysics* 61: 55–63.
- Song X (2000) Joint inversion for inner core rotation, inner core anisotropy, and mantle heterogeneity. *Journal of Geophysical Research* 105: 7931–7943.
- Song X and Richards PG (1996) Seismological evidence for differential rotation of the Earth's inner core. *Nature* 382: 221–224.
- Souriau A (1998) Earth's inner core – Is the rotation real? *Science* 281: 55–56.
- Souriau A and Souriau M (1983) Test of tectonic models by great circle Rayleigh waves. *Geophysical Journal of the Royal Astronomical Society* 73: 533–551.
- Stange S and Friederich W (1993) Surface wave dispersion and upper mantle structure beneath southern Germany from joint inversion of network recorded teleseismic events. *Geophysical Research Letters* 20: 2375–2378.
- Stutzmann É and Montagner JP (1993) An inverse technique for retrieving higher mode phase velocity and mantle structure. *Geophysical Journal International* 113: 663–683.
- Stutzmann É and Montagner JP (1994) Tomography of the transition zone from the inversion of higher-mode surface waves. *Physics of the Earth and Planetary Interiors* 86: 99–115.
- Su W-J, Dziewonski AM, and Jeanloz R (1996) Planet within a planet: Rotation of the inner core of Earth. *Science* 274: 1883–1887.
- Su W-J, Woodward RL, and Dziewonski AM (1994) Degree 12 model of shear velocity heterogeneity in the mantle. *Journal of Geophysical Research* 99: 6945–6980.
- Suda N, Nawa K, and Fukao Y (1998) Earth's background free oscillations. *Science* 279: 2089–2091.
- Takeuchi N, Geller RJ, and Cummins PR (2000) Complete synthetic seismograms for 3D heterogeneous Earth models computed using modified DMS operators and their applicability to inversion for Earth structure. *Physics of the Earth and Planetary Interiors* 119: 25–36.
- Takeuchi H and Saito M (1972) Seismic surface waves. In: Bolt BA (ed.) *Methods in Computational Physics*, vol. 11, pp. 217–295. New York: Academic Press.
- Tanaka S and Hamaguchi H (1997) Degree one heterogeneity and hemispherical variation of anisotropy in the inner core from PKPBC–PKPDF times. *Journal of Geophysical Research* 102: 2925–2938.
- Tanimoto T (2005) The ocean excitation hypothesis for the continuous oscillations of the Earth. *Geophysical Journal International* 160: 276–288.
- Tanimoto T and Alivizuri C (2006) Inversion of the HZ ratio of microseisms for S-wave velocity in the crust. *Geophysical Journal International* 165: 323–335.
- Tanimoto T, Um J, Nishida K, and Kobayashi N (1998) Earth's continuous oscillations observed on seismically quiet days. *Geophysical Research Letters* 25: 1553–1556.
- Thatcher W and Brune J (1969) Higher mode interference and observed anomalous apparent Love wave phase velocities. *Journal of Geophysical Research* 74: 6603–6611.
- Thomson DJ (1982) Spectrum estimation and harmonic analysis. *Proceedings of the IEEE* 70: 1055–1096.
- Toksöz MN and Anderson DL (1966) Phase velocity of long-period surface waves and structure of the upper mantle. *Journal of Geophysical Research* 71: 1649–1658.
- Trampert J and Spetzler J (2006) Surface wave tomography: Finite-frequency effects lost in the null space. *Geophysical Journal International* 164: 394–400.
- Trampert J and van Heijst H-J (2002) Global azimuthal anisotropy in the transition zone. *Science* 296: 1297–1299.
- Trampert J and Woodhouse JH (1995) Global phase velocity maps of Love and Rayleigh waves between 40 and 150 seconds. *Geophysical Journal International* 122: 675–690.
- Tromp J (1993) Support for anisotropy of the Earth's inner core from free oscillations. *Nature* 366: 678–681.
- Valette B and Lesage P (1992) Retrieving Mean Earth models. In: *Conference on Mathematical Geophysics, Taxco, Mexico*.
- van der Lee S and Nolet G (1997) Upper mantle S velocity structure of North America. *Journal of Geophysical Research* 102: 22815–22838.
- van Heijst H and Woodhouse JH (1997) Measuring surface-wave overtone phase velocities using a mode branch stripping technique. *Geophysical Journal International* 131: 209–230.
- van Heijst H and Woodhouse JH (1999) Global high-resolution phase velocity distribution of overtone and fundamental-mode surface waves determined by mode-branch stripping. *Geophysical Journal International* 137: 601–620.
- Vig PK and Mitchell BJ (1990) Anisotropy beneath Hawaii from surface wave particle motion observations. *Pure and Applied Geophysics* 133: 1–22.
- Webb SC (1998) Broadband seismology and noise under the ocean. *Reviews of Geophysics* 36: 105–142.
- Webb SC (2007) The Earth's 'hum' is driven by ocean waves over the continental shelves. *Nature* 445: 754–756. <http://dx.doi.org/10.1038/nature05536>.
- Widmer R (1991) *The Large-Scale Structure of the Deep Earth as Constrained by Free Oscillation Observations*. PhD Thesis, La Jolla, CA: University of California San Diego.
- Widmer R, Zürn W, and Masters G (1992a) Observation of low order toroidal modes from the 1989 Macquarie rise event. *Geophysical Journal International* 111: 226–236.
- Widmer R, Masters G, and Gilbert F (1992b) Observably split multiplets – Data analysis and interpretation in terms of large-scale aspherical structure. *Geophysical Journal International* 111: 559–576.
- Widmer R and Zürn W (1992) Bichromatic excitation of long-period Rayleigh and air waves by the Mount Pinatubo and El Chichon volcanic eruptions. *Geophysical Research Letters* 19: 765–768.
- Widmer-Schmid R (2002) Application of regionalized multiplet stripping to retrieval of aspherical structure constraints. *Geophysical Journal International* 148: 201–213.
- Wielandt E (1980) First-order asymptotic theory of the polar phase shift of Rayleigh waves. *Pure and Applied Geophysics* 118: 1214–1227.
- Wielandt E (1987) On the validity of the ray approximation for interpreting delay times. In: Nolet G (ed.) *Seismic Tomography*, pp. 85–98. Dordrecht: D. Reidel Publishing Company.
- Wielandt E (1993) Propagation and structural interpretation of non-plane waves. *Geophysical Journal International* 113: 45–53.
- Wielandt E and Schenk H (1983) On systematic errors in phase-velocity analysis. *Journal of Geophysics* 52: 1–6.
- Wilson T (1940) The Love waves of the South Atlantic earthquake of August 28, 1933. *Bulletin of the Seismological Society of America* 30: 273–301.
- Wong YK (1989) *Upper Mantle Heterogeneity from Phase and Amplitude Data of Mantle Waves*. PhD Thesis, Cambridge, MA: Harvard University.
- Woodhouse JH (1980) The coupling and attenuation of nearly resonant multiplets in the Earth's free oscillation spectrum. *Geophysical Journal of the Royal Astronomical Society* 61: 261–283.
- Woodhouse JH (1983) The joint inversion of seismic wave forms for lateral variations in Earth structure and earthquake source parameters. In: Kanamori H and Boschi E (eds.) *Proceedings of the Enrico Fermi International School of Physics LXXXV*, pp. 336–397. Amsterdam: North Holland.

- Woodhouse JH (1988) The calculation of eigenfrequencies and eigenfunctions of the free oscillations of the Earth and the Sun. In: Doornbos DJ (ed.) *Seismological Algorithms, Computational Methods and Computer Programs*, pp. 321–370. London: Academic Press.
- Woodhouse JH and Dahlen FA (1978) The effect of a general aspherical perturbation on the free oscillations of the Earth. *Geophysical Journal of the Royal Astronomical Society* 53: 335–354.
- Woodhouse JH and Dziewonski AM (1984) Mapping the upper mantle-3-dimensional modeling of Earth structure by inversion of seismic waveforms. *Journal of Geophysical Research* 89: 5953–5986.
- Woodhouse JH and Giardini D (1985) Inversion for the splitting function of isolated low order normal mode multiplets. *Eos, Transactions of the American Geophysical Union* 66: 300.
- Woodhouse JH, Giardini D, and Li X-D (1986) Evidence for inner core anisotropy from splitting in free oscillations data. *Geophysical Research Letters* 13: 1549–1552.
- Woodhouse JH and Gernius TP (1982) Surface waves and free oscillations in a regionalized earth model. *Geophysical Journal of the Royal Astronomical Society* 68: 653–673.
- Woodhouse JH and Wong YK (1986) Amplitude, phase and path anomalies of mantle waves. *Geophysical Journal of the Royal Astronomical Society* 87: 753–773.
- Woods MT, Lévêque J-J, Okal EA, and Cara M (1991) Two-station measurements of Rayleigh wave group velocity along the Hawaiian Swell. *Geophysical Research Letters* 18: 105–108.
- Yang X, Bondar I, Bhattacharyya J, et al. (2004) Validation of regional and teleseismic travel-time models by relocating ground-truth events. *Bulletin of the Seismological Society of America* 94: 897–919.
- Yang Y, Ritzwoller MH, Levshin AL, and Shapiro NM (2007) Ambient noise Rayleigh wave tomography across Europe. *Geophysical Journal International* 168: 259–274.
- Yang Y, Ritzwoller MH, Lin F-C, Moschetti MP, and Shapiro NM (2008) The structure of the crust and uppermost mantle beneath the western US revealed by ambient noise and earthquake tomography. *Journal of Geophysical Research* 113: B12310. <http://dx.doi.org/10.11029/12008JB005833>.
- Yao H, van der Hilst RD, and de Hoop MV (2006) Surface-wave array tomography in SE Tibet from ambient seismic noise and two-station analysis: I—Phase velocity maps. *Geophysical Journal International* 166: 732–744.
- Yomogida K (1985) Gaussian beams for surface waves in laterally slowly varying media. *Geophysical Journal of the Royal Astronomical Society* 82: 511–533.
- Yomogida K and Aki K (1987) Amplitude and phase data inversions for phase velocity anomalies in the Pacific ocean basin. *Geophysical Journal of the Royal Astronomical Society* 88: 161–204.
- Yoshizawa K and Kennett BLN (2002) Non-linear waveform inversion for surface waves with a neighbourhood algorithm; application to multimode dispersion measurements. *Geophysical Journal International* 149: 118–133.
- Yoshizawa K and Kennett BLN (2004) Multimode surface wave tomography for the Australian region using a three-stage approach incorporating finite frequency effects. *Journal of Geophysical Research* 109. <http://dx.doi.org/10.1029/2002JB002254>.
- Yoshizawa K and Kennett BLN (2005) Sensitivity kernels for finite-frequency surface waves. *Geophysical Journal International* 162: 910–926.
- Yoshizawa K, Yomogida K, and Tsuboi S (1999) Resolving power of surface wave polarization data for higher order heterogeneities. *Geophysical Journal International* 138: 205–220.
- Zhang J, Song X, Li Y, Richards PG, Sun X, and Waldhauser F (2005) Inner core differential motion confirmed by earthquake waveform doublets. *Science* 309: 1357–1361.
- Zhou Y, Dahlen FA, Nolet G, and Laske G (2005) Finite-frequency effects in global surface-wave tomography. *Geophysical Journal International* 163: 1087–1111.
- Zielhuis A and Nolet G (1994) Shear wave velocity variations in the upper mantle. *Geophysical Journal International* 117: 695–715.
- Zürn W, Laske G, Widmer-Schmid R, and Gilbert F (2000) Observation of Coriolis coupled modes below 1 mHz. *Geophysical Journal International* 143: 113–118.
- Zürn W and Widmer R (1995) On noise reduction in vertical seismic records below 2 mHz using local barometric pressure. *Geophysical Research Letters* 22: 3537–3540.

Relevant Website

<http://igppweb.ucsd.edu/~gabi/rem.html> – The Reference Earth Model Website (accessed June 2014).